BARIUM ION CAVITY QED
AND
TRIPLY IONIZED THORIUM ION TRAPPING

A Thesis
Presented to
The Academic Faculty

by

Adam V Steele

In Partial Fulfillment
of the Requirements for the Degree
Doctor of Philosophy in the
Department of Physics

Georgia Institute of Technology
December 2008

BARIUM ION CAVITY QED
AND
TRIPLY IONIZED THORIUM ION TRAPPING

Approved by:

Michael Chapman, Advisor
Department of Physics
Georgia Institute of Technology

Alex Kuzmich
Department of Physics
Georgia Institute of Technology

T.A. Brian Kennedy
Department of Physics
Georgia Institute of Technology

Chandra Raman
Department of Physics
Georgia Institute of Technology

Ken Brown
Department of Chemistry
Georgia Institute of Technology

Date Approved: 14 November 2008

To the wonderful future

ACKNOWLEDGEMENTS

Though this thesis has but a single author listed on the title page, it could never have been written without the large group of people supporting its completion. So, first I would like to thank my research advisor Mike Chapman. I walked past his door on one of my first weeks here and saw a small sign that read *Quantum Computing Lab,* so I knew immediately for whom I wanted to work. He took me into his lab despite already having had quite a few students knock at his door. He has a very level headed and practical approach to the experiments, especially handy when the students start to freak out crying, "nothing is working, and it never will!" He also allows his students work on the fun of the experiments without worrying overmuch about un-fun things like money or bureaucracy. I have also enjoyed our political discussions, despite the ocean of difference between his positions and mine.

The person I worked most closely with for the past years was Layne Churchill. Layne and I worked for long periods in the early days without much success in building our first ion trap but managed to keep our chins up and just keep spitballing ideas until one stuck and we got that first trap working. Layne has become a great friend of mine through our years of working together. We have had many interesting political and religious discussions. Layne always answered religious questions I asked him with honesty and thoughtfulness without taking offense; coming as the questions did from an atheist worldview. I think he embodies some of the finest ideals of the Christian faith.

I would also like to thank our collaborators in the lab of Alex Kuzmich. Alex, Michael DePalatis, David Naylor and Corey Campbell all worked alongside us on the thorium project. Having such a gifted group on the thorium project is what enabled

us to think of new approaches and test them out quickly. Troubleshooting problems as a group allowed us to find problems and make corrections orders faster than would have been possible otherwise.

Lots of thanks go to my other friends in the lab, even if they were in the other room. Kevin Fortier somehow became good friends with me, despite the fact that I would make him walk down the hall to help me at least twice a day for months on end when I first joined the lab. I thank Soo Kim for her laughter which somehow has the ability to pierce the concrete walls of Georgia Tech. I thank Michael Gibbons for letting me call him Mikey G, even though I suspect he hated it.

A few more folks outside the lab also deserve special mention for the impact they have had on the evolution of my work and personality. First is Joanna Hass. Joanna is one of the finest people I've ever met. She has a generous spirit, and is always there for her friends. We have drank to each others successes and drank to commiserate. I am proud to call her my friend. I would also like to thank Lisa McManus. Lisa's support in the last months of this work gave me all I needed to successfully finish. Who else would bring me lunch and dinner at the lab when I am sure I looked bad and smelled worse? I found in her someone worth working to impress and someone who I knew would fight for me. Finally I would like to thank my parents. My mother's unending encouragement and my father's stimulation of my interest in science was critical to all of my achievements.

TABLE OF CONTENTS

LIST OF TABLES

LIST OF FIGURES

SUMMARY

Trapped cold ions are tools which we used to approach two very disparate areas of physics, strong coupling between Ba^+ ions and optical resonators, and investigations of a low-energy nuclear isomer of ^{229}Th. The first part of this thesis describes our progress towards the integration of a miniature Paul (rf) ion trap with a high finesse ($\mathcal{F} \approx 30000$) optical cavity. Ba^+ ions were trapped and cooled for long periods and a new scheme for isotope selective photoionization was developed. The second part of this thesis describes our progress towards controlled excitation of the low energy nuclear isomer of ^{229}Th, which may provide a bridge between the techniques of cold atomic and nuclear physics. As a step towards this goal, $^{232}Th^{3+}$ ions were confined in rf ions traps and cooled via collisions with a buffer gas of helium. A sophisticated scanning program was developed for controlling ion trap loading, tuning lasers, and running a CCD camera to look for fluorescence. The low-lying electronic transitions of Th^{3+} at 984 nm, 690 nm and 1087 nm were observed via laser fluorescence.

CHAPTER I

INTRODUCTION

The study of interactions between one or a few atoms with a tunable laser has stood at the forefront of atomic physics for several decades now. Applications have included laser cooling of ions [1] and neutral atoms [2], and confinement of neutral atoms [3]. Cooling and confinement in turn revolutionized the world of precision spectroscopy [4], allowed for the creation of a Bose-Einstein condensates [5]. More recently, trapped cold atoms allowed for the first steps to be taken towards a scalable atom-based quantum computer [6] and for the construction of the building blocks of a robust quantum information network [7, 8].

Cold trapped ions have a number of exciting roles to play in the future of both precision measurements and quantum computation. In the first part of this Chapter, we will elaborate on a sample of the roles cold atoms have played. This elaboration will be followed by a description of the long term goals of our experiments in barium ion cavity quantum electro-dynamics (QED) and investigations of a low energy nuclear isomer of ^{229}Th. The Chapter concludes with our experimental contributions to the goals of these experiments.

The most precise measurements of atomic transition energies and lifetimes are limited by the perturbations of the measured atomic system. These perturbations may include the existence of, or fluctuations in, background electric or magnetic fields, or atomic motion induced doppler shifts. To reduce the effects of doppler-related perturbations, cooling of atoms is necessary. Lasers are able to cool atoms by exerting a radiation pressure force which is both directional and velocity dependent. Through the use of the radiation pressure force, atoms may readily be brought to

speeds of less than 1 m/s and temperatures of less than 1 mK [9].

Even at these cold temperatures, the precision of certain measurements is limited by the interaction times of the atom and laser, therefore confining the atom(s) to be interrogated is advantageous. Performing measurements on a large number of atoms and averaging the result is an option is some experiments, but in some cases this limits precision due to interaction between the atoms and variations on the fields experienced by the atomic ensemble.

With time, a variety of traps for both neutral atoms and ions were developed. The most popular neutral atom traps are magneto-optical traps (MOTs), magnetic traps and optical dipole force traps. For ions the two most popular types of traps are Penning traps and Paul, or radio-frequency (rf), traps. In this thesis, we worked with singly ionized barium (Ba^+), and triply ionized thorium (Th^{3+}) ions, and confine them using rf traps.

The linear rf trap has found use in some of the most precise atom measurements to date ([10]) and also is the tool of choice for mass-spectroscopic measurements done in many fields of science and industry. Indeed, one of our apparatus was made from a modified off-the-shelf ion filter, allowing us to capitalize on the 50 years spent perfecting these devices and instead focus our attention on the true challenges of the experiment. Rf traps are excellent storage devices owing to their large trap depth (up to 10^5 K). This depth is advantageous as it allows ions initially moving at high velocities to be confined and then cooled. Additionally, in the linear rf ion trap we used, a number of ions may all be confined at a point where the electric and magnetic fields are at a minimum, substantially reducing perturbations present in many other types of neutral atom and ion traps.

A frequency standard based on an atomic resonance offers a much higher standard of accuracy than the quartz-based standards which preceded them. The first implementation of an atomic standard measured the hyperfine energy level splitting

at ∼9.2 GHz in the ground state of the cesium atom in 1955 [11]. The initial clock had a fractional accuracy of 10^{-9}. Over the years the clock was improved by cooling the cesium atoms until recently when an uncertainty of about 10^{-15} was achieved [12].

The use of cold trapped ions has pushed the accuracy of atomic clocks ever higher. A standard based on a laser cooled trapped mercury ion in an rf ion trap has achieved a fractional uncertainty of $7 \cdot 10^{-17}$ [4] on the measurement of an electric quadrupole transition at 282 nm, with a projected ultimate limit of 10^{-18} [13].

1.1 Barium Ion Cavity QED

In our Ba^+ cavity QED experiment, we aim for a condition where single atoms and *single* photons interact for long periods. By this interaction we may combine the long term quantum memory of an atomic qubit with the long-distance transmission stability of a photonic qubit.

Several immediate applications of the strongly coupled ion/cavity system motivates this research. First, it may find use as a quantum repeater. In many classical information networks transmission is performed by means of light through an optical fiber, which is converted back into an electrical signal at the fiber's ends. Since any optical signal input to a fiber will decay exponentially with the fiber's length, communication over arbitrarily large distances would not be possible (without exponential overhead) if the optical signal could not be boosted at intermediate distances. For transmission of classical information, this boost is provided by an optical communications repeater.

In a quantum communication network, transmission of information over long distances is more complex. The no-cloning theorem forbids the copying of quantum states, so a quantum information repeater will be a distinctly different device. The requirements for a quantum repeater are described in [14]. As described in [15], an

atom strongly coupled to an optical cavity would meet these requirements and be able to act as a node in a quantum information network.

The system also has potential use as a quantum computer [16]. Ion trap based computers which no not utilize cavities confine several ions to the same trapping potential, and the shared motional phonons allows conditional logic between ions to be performed. Scaling this system up to more than a handful of qubits may be problematic however, due to difficulties arising from the more complicated phonon mode structure of larger numbers of ions, or from the challenge of physically moving ions between traps. An alternative scheme, described by [17], calls for a small number of ions in several individual traps. Each set of ions will also possess its own high finesse cavity which will be used for transporting quantum information between traps.

A third application the single atom-cavity arrangement offers is a single photon server, where individual light quanta can be delivered on demand. This is a system which may have applications for quantum cryptography [18] and quantum information processing [19]. However, for this scheme to be useful strong coupling is not required. These systems have been implemented with both ions [20] and neutral atoms [21].

One of the most challenging aspects of neutral atom-based cavity QED experiments has been to localize the atom's position to much less than one optical wavelength. This is called the Lamb-Dicke limit. We aim to achieve this level of precision because the strength of the atom-cavity interaction, and the fidelity with which the atom's internal state may be mapped onto the cavity's photon state, both depend on knowledge of the amplitude of the field to which the atom will be exposed.

Strong confinement of neutral atoms requires intense laser fields which generate an AC stark shift in the atoms. By contrast, rf ion traps give a high degree of confinement automatically for doppler cooled atoms and localize the ions in a field-free region. In [22], the ion's wavepacket was shown to be localized to a length of less than 40 nm.

Ion traps also offer exceedingly long trap lifetimes. While the state of the art

efforts in [23] have offered confinement of neutral atoms for up to 300 s, ion traps can provide confinement of the same ion for days.

Strong coupling of atoms and cavities requires very high quality mirrors. The technology to make these *supermirrors* is most advanced in the near-IR, slightly less advanced in the visible regime, and non-existent in the ultraviolet. Therefore, many of the ions used in modern day quantum computing experiments, such as Cd^+, Be^+ are not suitable for cavity QED because their strong transitions fall in the UV. Both Ba^+ and Ca^+ are exceptions, these ions both have atomic lines for which good mirrors can be obtained.

Another requirement is that the atom selected have a pair of long lived states which can serve as qubits. The atomic system to be used in this experiment is the ground state hyperfine manifold of $^{137}Ba^+$. The odd mass number isotopes of barium possess nuclear spin of 3/2, which splits the 2 $S_{1/2}$ ground states by 8 GHz. This hyperfine manifold makes an ideal quantum qubit memory, owing to the long lifetimes of these states.

1.2 Thorium Ion Trapping

About 15 months ago the Kuzmich and Chapman labs began a combined effort aimed at trapping Th^{3+} ions. We were able to make rapid progress towards our eventual goal of applying decades of developed atom-laser technologies to the world of nuclear interactions. Until now, atom-laser interactions were limited in that they could only probe the electronic structure of the atom, since these are the transitions which lie in the frequency range of the available lasers, from the near UV to the far IR. A low-energy excited state of the nucleus of ^{229}Th is an exception which may prove amenable to excitation by a coherent source of ultraviolet radiation.

Coherent control over the excitation of the ^{229}Th isomer may enable the next leap in the accuracy of atomic clocks. The lifetimes of excited states of the nucleus, like

their electronic counterparts, may be either very short (ps lifetime) or in the case of metastable isomeric levels, quite long (several hours). The predicted narrowness of a long-lived metastable level in the ^{229}Th isotope (~ 10 μHz) and its reduced susceptibility to environmental perturbations suggest it may become an excellent candidate for a frequency standard. While the exact limits of the uncertainty on such a measurement are not known, it is believed that an improvement of at least an order of magnitude over the projected limits of present atomic clocks may be achieved [24].

The long confinement lifetimes and low perturbations due to the confining potential which make ions traps so attractive for atomic clocks, also make these traps ideal for precision measurements of fundamental constants. Precision measurements of both the electronic *g-factor*, which is related to a measurement of the fine structure constant α via QED, and also the electron mass, have both been performed in ion traps to a remarkable precision [25]. While these serve as precision tests of well-established theories, precision studies of fundamental constants can also be useful for testing of new theories. Unification theories suggest that α and $m_{q,e}/\Lambda_{QCD}$ may be varying with time. Here Λ_{QCD} is a quantum chromodynamics energy scale and m_q and m_e are the quark and electron masses. The isomer transition in ^{229}Th has a particular feature which is believed to enhance any measured variation of these constants by a factor of 5-6 orders of magnitude [26]. The feature is due to the cancelation of two terms in the expression for the strong potential in the nucleus. The cancellation gives rise to an observed enhancement of variations of the light (up and down) quark masses. This is in addition to the enhancement offered by the narrowness of the isomeric transition. However, the existence of the enhancement is still a point of contention [27, 28, 29, 30].

This experiment is an essential step towards the coherent control over the metastable isomer transition in ^{229}Th. Such control has the potential to impact many areas of atomic and nuclear physics.

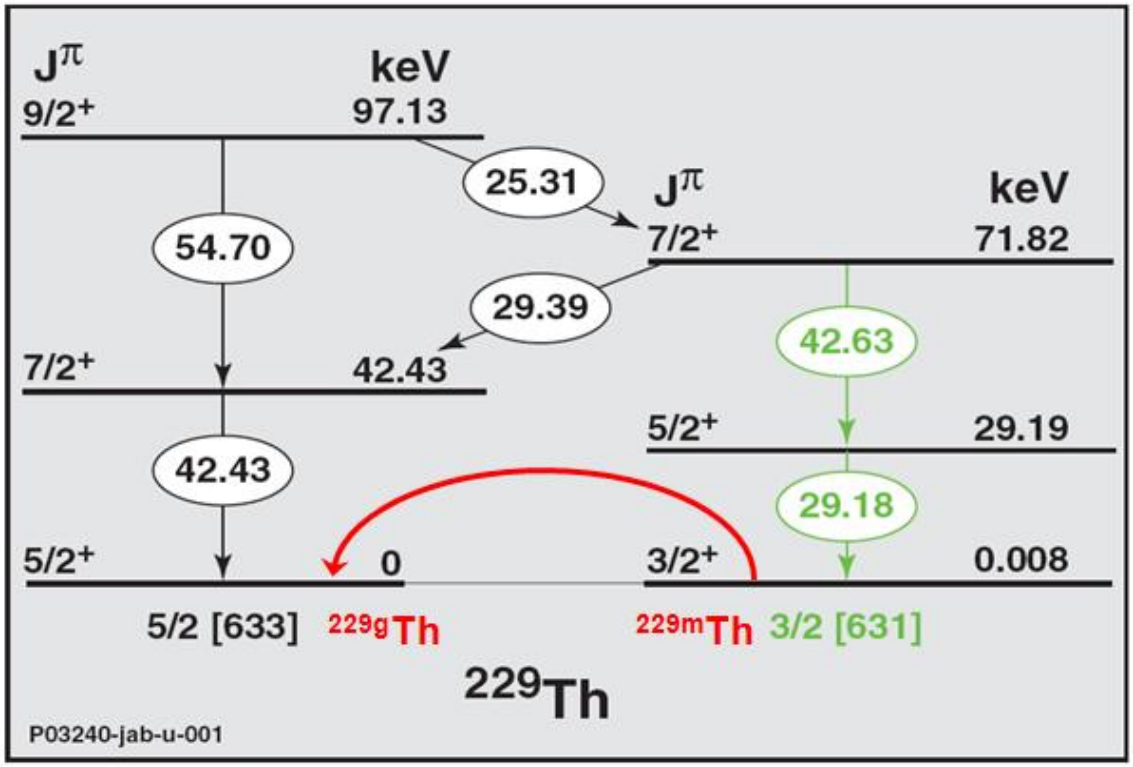

Figure 1: The low energy isomer states of ^{229}Th. The 7.6 eV transition is indicated by the red arrow. The levels are placed into two different columns (indicating different nuclear rotational bands) for clarity. Improvements in detector technology has recently the resolution of the 29.39 keV and 29.18 keV decays. Figure taken from [31]

1.2.1 Background

Nuclear isomers are typically populated via decay from another nuclide. In Fig. 1, some of the low-lying isomeric states of ^{229}Th are cataloged. A alpha decay from ^{233}U can populate the 5/2[633] $9/2^+$ Nilsson rotation band of thorium which will decay by emission of gamma rays, following one of several decay channels to the ground state, which has a nuclear spin $I = 5/2$. The vast majority of nuclear isomers are short lived, having a lifetime of order 10^{-12} s. A few are long lived metastable states. One path along the nuclear decay of ^{229}Th to its ground state passes through a metastable state with $I = 3/2$. The decay from this metastable level to the ground state is the focus of our experiment. It is unique among known isomers in its low energy, 7.6 ± 0.5 eV [31].

The existence of the low-energy (<0.1 keV) isomer state in the ^{229}Th nucleus was first proposed by Kroger and Reich [32]. Thirteen years later in [33], ^{229m}Th [1] was determined to be -1 ± 4 eV above the ground state. Subsequent measurements four years later by the same authors yielded a value of 3.5 ± 1.0 eV [34]. In none of these energy measurements was the $^{229m}\text{Th} \rightarrow \text{Th}^{229}$ photon observed directly, instead a variety of 'differencing' schemes were used. X-ray photons emitted following the decay of the ^{233}U were measured, their energies compared, and each associated with different paths in the decay channel. In this way the energy of the unobserved transition was inferred.

Many attempts at direct measurement of the decay photon at 3.5 eV were attempted without success. Two efforts in the 1990's reported the observation of low energy photons in the energy range of 2.5-4 eV from a sample of ^{233}U [35, 36]. These were initially believed to be due to the ^{229m}Th state. However, it was subsequently shown by [37, 38] that these photons were being emitted by N_2 discharge arising from the radiation emitted by the ^{233}U sample. More recent measurements by [39, 40] attempted to minimize these effects by isolating the ^{229}Th from the ^{233}U chemically. But these efforts were not able to identify any photons which could be associated with the decay of ^{229m}Th. Despite the difficult in observing the decay of this state directly, the possibility of observing such a low-energy long-lifetime isomer stimulated the proposals for using this transition discussed above.

The 3.5 eV measurement stood until very recently in 2007 when a new measurement yielded a value of 7.6 ± 0.5 eV [31]. This would explain why attempts at direct measurement of 3.5 eV photons in [39, 40] did not succeed, since the detectors used in those searches had no sensitivity at 7.6 eV wavelengths, and in any case 7.6 eV photons would have been absorbed by the quartz cells containing the samples.

[1] Metastable isomer states are usually denoted with an m superscript following the atomic mass, and that notation will be used here

Precision work with nuclear isomers is complicated by their high energies. The vast majority of these transitions are in the X-ray spectrum spanning from about 120 eV to 120 keV. A variety of detectors such as multi-channel plates, CCDs and microcalorimeters allow for the detection and energy measurement of x-rays emitted from excited nuclei. These devices all allow for the measurement of isomeric energies. The revised energy measurement of the ^{229m}Th decay in [31] was enabled by the use of a new x-ray calorimeter which examined the different decay channels shown in Fig. 1.

This revised measurement motivated our interest in this experiment. Building upon our previous experience in trapping barium ions, we chose to pursue an approach towards observation of the isomeric state using laser cooled Th^{3+} ions as suggested by Peik and Tamm [24]. The strengths and difficulties inherent to this approach are summarized in the next section.

1.2.2 Concept

The experiment's final goal is to observe the excitation of the 7.6 eV isomer transition in ^{229}Th. While the aims of the experiment are simply stated, a number of technical hurdles will have to be overcome before its goals may be accomplished. We will drive this transition in trapped $^{229}Th^{3+}$ ions. Observation of the isomeric excitation will be accomplished by a 'shelving' technique. This will be elaborated on below. Triply ionized thorium will be used because it has a simple level structure and because it will inhibit the internal conversion nuclear decay processes which are energetically allowed in neutral thorium. These decay processes are detailed below.

For a bare nucleus of ^{229}Th, the only manner of decay from the ^{229m}Th state to the ground level is by the emission of a photon (Fig. 2a). The presence of any electrons bound to the nucleus adds a number of other decay channels. In one process called internal conversion the nuclear decay leads to the ionization of the atom, with the electron carrying off any energy surplus as kinetic energy (Fig. 2b). This is

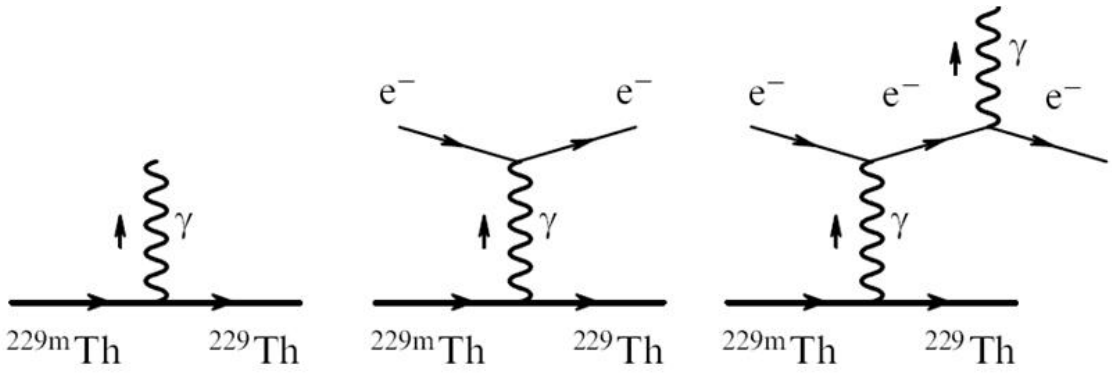

Figure 2: Feynman diagrams of three ^{229m}Th decay channels. On the left is direct photon decay. In the middle is internal conversion where the isomer energy ionizes the atom. On the right is the electron bridge, where the isomer decay excites a bound electron and emits the isomer-orbital energy difference as a photon. Figure taken from [42]

particularly undesirable decay channel, since in addition to making the isomer lifetime shorter, it will change the charge state and energy level structure of the atom. Another decay channel called electron bridging is also possible [41]. Here a bound electron is excited to another bound state and the atom emits a lower energy photon with the energy difference between the bound-bound transition and the isomer energy (Fig. 2c). Each of these channels will reduce the lifetime of the isomer state. The Feynman diagrams for these decay channels can be seen in Fig. 2. Relative decay rates for the different decay channels in neutral thorium were compared theoretically in [41] and calculated to be approximately equal, but this was for the outdated value of 3.5 eV. In [43], the spectrum of delayed photons arising from the relaxation of the isomeric state through the electron bridge was examined for the new 7.6 eV value and found to have a potentially very strong effect on the isomer lifetime, reducing it by many orders of magnitude. The authors also concluded a very small 10^{-5} s lifetime for decay by internal conversion for a neutral Th atom.

The ionization energy of Th^{3+}, 29 eV, is substantially higher than the 7.6 eV energy difference of the isomer state. The 22.5 eV energy gap between the ionization

energy and the isomer energy prevents the internal conversion isomer decay from occurring. This is one motivating reason for attempting to observe the isomeric transition in a positive thorium ion, as opposed to neutral thorium, which has an ionization energy of only 6.1 eV and would thus be susceptible to internal conversion decay of the 7.6 eV isomer state.

The second reason for using Th^{3+} rather than another thorium ion is its simplified level structure. Th^{3+} provides a close two-level transition at 1087 nm. It also has a closed Λ-system (see section 2.2.4) with transitions at 690 nm and 984 nm. To achieve continuous observation of fluorescence in either Th^{+} or Th^{2+} would require more lasers. Fluorescence imaging of trapped $^{232}Th^{+}$ was accomplished by [44], but there the ions were excited by a single laser and quenched back to the ground state from a low-energy metastable level through collisions with an gas of helium or hydrogen introduced to the chamber. The most precisly quoted energies of the transitions in Th^{3+} at 1087 nm, 984 nm and 690 nm (compiled from several previous studies) were reported in [45]; but no error bars were given for these measurements.

The ground state of ^{229}Th has a nuclear spin of 5/2, resulting in a rich hyperfine structure, so modulation of the lasers or introduction of microwave fields will also be required for observation of fluorescence. Measurement of of the hyperfine splitting factors of $^{229}Th^{+}$ for three particular energy levels was reported in [46]. Similar measurements will have to be made to find the hyperfine splitting in $^{229}Th^{3+}$.

Another thorium isotope, ^{232}Th, does not possess the isomer state. However, since it lacks any nuclear spin it can more easily be used to find the laser wavelengths to observe fluorescence. It is also much less expensive, so it is more practical to use this isotope to perfect the ion creation and trap loading stages of the experiment. After ion creation and fluorescence observation with $^{232}Th^{3+}$ has been accomplished, we can switch to using ^{229}Th and find its hyperfine structure.

Two similar experimental systems were used in this work. One chamber built by

Corey Campbell, Michael DePalatis and David Naylor was a linear quadrupole trap with a design similar to a commercial mass-spectrometer made by the Finnigan company. Confined ions may be counted electronically by exciting them with radiation at the trap frequency until they are ejected through a slit cut into a trap electrode and into a channel-electron multiplier. This technique and its structure are described in greater detail in 2.1.

The second system used was a commercial linear 4 rod mass-spectrometer (Stanford Research Systems RGA 100), with two pairs of electrodes added for confinement in the axial direction. Confinement in the radial direction is provided by alternating high voltage fields. Ions may be read out electronically here by turning off the trapping voltage along one of the trap's axes. The confined ions may be detected by observing their induced fluorescence on a CCD camera. The trap may be operated in a mode that only permits long term confinement of Th^{3+} so that other charge states of thorium or vacuum contaminants are not confined. The apparatus is described in greater detail in section 4.1.2.

Creation of the ions was accomplished by laser ablation. By using a lens to focus the third harmonic of a pulsed YAG laser at a pulse energy of a few mJ onto the surface of metallic thorium a plume of neutral thorium, electrons and thorium charge states from 1+ to 3+ and higher were created. These ions are initially outside of the trapping region. By modulating the trapping fields as the ions approach they can be captured. This process is detailed in sections 4.7.2 and 4.2.

Ions loaded in this way will have an energy which is near the trap depth (10^5 K), so they are cooled initially by a 'buffer gas' of helium introduced into the vacuum chamber. The light gas molecules damp out the motion of the ions and reduce their temperature from a large fraction of the trap depth down closer to room temperature. Subsequent direct Doppler cooling or sympathetic cooling of the ions may be used to reduce their temperature down to mK or less. Sympathetic cooling would require

the loading of another ion species, such as Ba^+ into the trap, laser cooling it to low temperatures, and allowing the inter-ion collisions to bring the Th^{3+} temperature down.

Once the ion is trapped and cooled, isomer excitation and de-excitation will be accomplished. Simply exciting the transition and then waiting for decay is not feasible given the exceedingly long calculated ∼5 hour [31] lifetime of the excited state. Instead a 'shelving' process will be used. The shelving detection works as follows. Suppose an ion is being observed via fluorescence imaging by illuminating it with light at 1087 nm and additional microwave frequencies. Suppose then that the isomer state is excited by illuminating the ion with light at 163 nm (7.6 eV). After the transition, the nuclear spin becomes 3/2. This will shift the hyperfine levels on the 1087 nm transition, so no more fluorescence will be observed. If we then de-excite the ion by stimulated emission the fluorescence will return. The relevant levels and how they shift during the isomer transition is shown in Fig. 3. Shelving allows us to observe the ion making the isomer transition without waiting for the decay of the excited state or need to collect the 7.6 eV photons. This technique has been used to make a number of very precise measurement of atomic line strengths and lifetimes, for instance in Ba^+ ions [47].

Alternatively, if the electron bridging process results in a substantially shortened lifetime over the bare nucleus estimate of 5 hours, then another path to excitation may be available. By exciting an intermediate state, such as the $^2D_{5/2}$ state above the ground level with a laser at 690 nm, and then illuminating with light at ∼213 nm, the isomeric state may be excited through the electron bridge. The 213 nm (5.6 eV) wavelength is determined by the difference between the energy of the upper level in the 650 nm transition (1.9 eV) and the 7.6 eV (163 nm) isomer energy. The bridging process was examined for the 3.5 eV excitation energy, leading to widely varied estimates of its width [48, 49, 50]. No refined calculations have yet been done

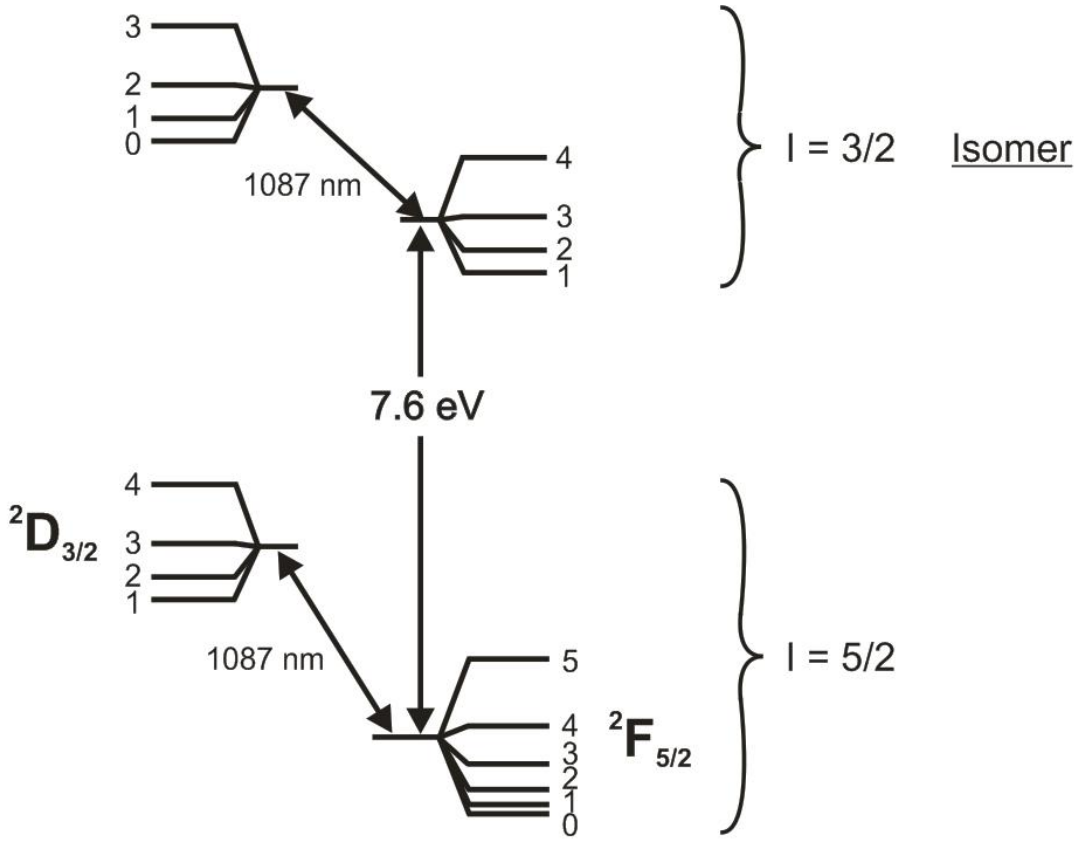

Figure 3: Relevant energy levels for shelving detection based technique of $^{229}Th^{3+}$ and the 1087 nm cycling transition in this ion. When the isomer state is excited hyperfine and chemical shifts will extinguish ion fluorescence. Splittings are not to scale. (Figure by C. Campbell)

for the new 7.6 eV value, but renewed interest in this isomer will likely stimulate enough excitement for these studies to be conducted. If the strength of the electron bridge winds up being substantial, then the task of excitation of ^{229m}Th may be substantially easier, since light at ∼213 nm will be much easier to generate than light at 163 nm. The shelving detection method would remain the same if the isomer were excited via the electron bridge.

1.2.3 Feasibility

Some aspects of the thorium ion trapping experiment pose as-yet unresolved problems for implementation. Foremost among these is the uncertainty in the present measurement of the isomer excitation energy. Assuming that the most recent measurement is accurate, other issues include generation of the 163 nm light, the effects this light might have on trapped ions and the detection of the isomer excitation. However, even before the isomer excitation may be driven, continuous excitation of the ^{229}Th isotope must be achieved, and this is complicated by its hyperfine structure.

The ground state ^{229}Th nucleus has I=5/2, and its ground state is $^2F_{5/2}$, yielding six levels in the ground state manifold, F=0..5. With six states in the manifold, five microwave fields will need to be applied to the atom, or five modulation frequencies applied to the laser to prevent the atoms from falling into states which are *dark* to the laser. So far, there are no known calculations for the splitting of this system. That said, a few remarks are worth making regarding the hyperfine structure, following the derivation of Joachain and Brandsen [51]. The two dominant terms in determining the hyperfine splittings will arise from the magnetic dipole and electric quadrupole moments of the nucleus: the former arising from the spin angular momentum of the nucleus, were it treated as a point source, the latter from the nucleus's non-uniform charge arrangement. There are no magnetic quadrupole or electric dipole nuclear moments. The splitting due to the magnetic dipole from some F to some

F+1 (F=I+J) may be written

$$\Delta E = \frac{C}{2}K \tag{1}$$

$$C = \frac{\mu_0}{4\pi}4g_I\mu_B\mu_N\frac{1}{J(J+1)(2L+1)}\frac{Z^3}{a_\mu^3 n^3} \tag{2}$$

$$\mu_N = \frac{m_e}{m_p}\mu_B \tag{3}$$

$$a_\mu = a_0(m/\mu) \tag{4}$$

$$K = F(F+1) - I(I+1) - J(J+1) \tag{5}$$

were μ_B is the bohr magneton, $g_I \approx 1$ the Landé factor, m_e and m_p the electron and proton masses, μ the reduced electron mass (with respect to the nucleus) and Z the nuclear charge. The electric quadrupole moment is given by

$$\Delta E = \frac{B}{4}\frac{\frac{3}{2}K(K+1) - 2I(I+1)J(J+1)}{I(2I-1)J(2J-1)} \tag{6}$$

where B is called the quadrupole coupling constant and given by

$$B = -Q\left\langle j, m_j = j \left| \frac{3z^2 - r^2}{r^5} \right| j, m_j = j \right\rangle \tag{7}$$

Q is the electric quadrupole moment of the nucleus and the other term is the gradient of the electron's E-field at the nucleus. Thus the total level shift is given by

$$\Delta E = \frac{C}{2}K + \frac{B}{4}\frac{\frac{3}{2}K(K+1) - 2I(I+1)J(J+1)}{I(2I-1)J(2J-1)} \tag{8}$$

The electric and quadrupole moments of the ground state nucleus of ^{229}Th are not known. They will have to be found experimentally. In the longer term, nuclear models may be employed to calculate the excited state multipole moments from those of the ground state. This would allow for direct observation of fluorescence from the excited isomeric state.

As discussed earlier, there have been a number of previous measurements of the isomer energy splitting. The most recent of these establishing the energy as 7.6 ± 0.5 eV [31] is different by more than three standard deviations from the previous

measurement of 3.5 ± 1 eV [34]. The techniques for both of these measurements rely on being able to calculate differences between x-ray energies of ∼100 keV. Therefore, a 1 eV uncertainty requires a precision of 10^{-5} in these measurements. In the 3.5 ± 1 eV measurement, a number of broad (∼300 eV or ∼900 eV depending on the center energy) line centers had to be measured very accurately. This required extensive use of reference lines and long periods of data collection.

Until the metastable isomer decay photon is measured directly it remains possible that these measurements are in some way flawed. Of course, direct measurement of the decay photon may be exceedingly difficult, depending on the relative branching ratio between the different decay channels described above in Fig. 2. If internal conversion processes dominate the decay, then few photons but many electrons may be emitted from the ^{229m}Th source. If the electron bridge decay is dominant, then photons at a variety of wavelengths may be emitted, each of which would correspond to a particular electronic transition in the atom.

A long isomer lifetime will be important if it is to used as a clock transition, or for examination of time variation in fundamental constants. As mentioned above, in [31] a 5 hour lifetime was estimated based on a comparison made with a particular level in ^{233}U. Two attempts have been made to measure the lifetime of the excited state. In [52] an attempt was made to observe growth of ^{229g}Th from ^{229m}Th through the ground state's α decay (observed indirectly by measuring subsequently emitted γ rays). While no time dependence was observed, this allowed the authors to place lifetime bounds of < 6 hours or > 20 days on the metastable state. In [53] a similar measurement was made, but the method of ^{229}Th creation was different and the alpha emission was observed directly. In this study a lifetime of 14 ± 3 hours was concluded. Though these calculations and measurements are not definitive, they suggest the ^{229m}Th state is long lived.

Driving the isomer transition will be a substantial challenge. The 7.6 eV (163 nm)

transition energy is in the vacuum ultraviolet; therefore air will strongly attenuate it. Additionally, light at this frequency is a challenge to even generate. A high harmonic of a frequency comb may have some spectral power in this band, but the power will be minuscule (<10 μW) [54]. But given the narrowness of the transition the power needed may depend more on the temperature of the trapped ions. Other tuneable light options include the use of frequency differencing crystals. In [55] a scheme was demonstrated which should cover the entire range of 108 to 193 nm with the use of a β-barium borate crystal (BBO) being fed with light at 193 nm(the edge of the VUV range and a dye laser) from an ArF eximer laser and a tuneable dye laser. A more straightforward frequency doubling to 163 nm is not possible with BBO, whose limit is 205 nm. A more realistic option at present would be an incoherent light source like a flash lamp. A deuterium flash lamp has a spectral output from 115 nm to 400 nm. If a lamp drove the transition, then the transition wavelength might be more precisely identified by collimating the lamp's output and using a diffraction grating to split up the spectrum.

1.3 Contribution of Present Work

1.3.1 Progress Towards Ion Trap+Cavity Integration

This thesis presents contributions towards the goal of the barium cavity QED experiment as described in Sec. 1.1. We constructed a linear rf ion trap and succeeded in loading it with Ba^+ ions. Doppler cooling of these ions was accomplished by exposing the trapped ions to light below the atomic resonances at 493 and 650 nm. Dark states arising from the Zeeman structure of the two states in the 650 nm transition where eliminated by using a magnetic field. Temperatures of less than 1 K where achieved, and ions where cooled into an ordered coulomb crystal. A new method for isotope selective photoionization of barium was developed and a new type of vapor cell for saturated absorption spectroscopy was developed. Finally, high finesse cavities were

constructed in preparation for the next stage of this experiment in which we will confine a single Ba^+ ion in the cavity's field mode.

1.3.2 $^{232}Th^{3+}$ Ion Trapping

We successfully employed laser ablation to create $^{232}Th^{3+}$ ions. Using dynamic adjustment of trapping potentials we were able to load the ions produced by several laser pulses together into the same trap. Yields of many thousands of Th^{3+} can obtained in this fashion. These ions can be identified as Th^{3+} using the mass/charge selectivity of the trap and can be counted electronically by emptying the trap into a channel-electron multiplier and counting the pulses on its output. Ions were cooled with a helium buffer gas. Additionally, we observed laser fluorescence of the trapped Th^{3+} ions and have determined the transition wavelength with a precision of ± 100 MHz. This work constitutes an essential step towards the direct observation of the ^{229}Th isomer transition using trapped ions.

1.4 Organization of Thesis

In Chapter 2, the theoretical background of the experiment will be explained. Topics covered will include the theory of the linear ion trap and mass filter and a section detailing the heating and cooling mechanisms at play in this work. The heating effects arise from ion-neutral atom collisions and ion-ion collisions. Cooling, specifically Doppler cooling, will be covered. First the simple case of a two level ion oscillating in the trap is reviewed, for which simulations of cooling are given. Then the more complex case of a 3-level lambda system is covered, and the inherent complication of coherent population trapping. Additionally, the techniques required for elimination of dark states in the lambda systems of both Ba^+ and Th^{3+} are discussed. Also in Chapter 2, the phase change from chaotic ion cloud to ordered coulomb crystal will be covered, as will several mechanisms by which ions may be lost from traps. The chapter concludes with some background on classical cavities, and the important

figures of merit characterizing the strong coupling regime in cavity QED.

Chapter 3 presents our progress towards the integration of a miniature Ba^+ ion trap and a high-finesse optical cavity. First, our initial efforts at trapping of Ba^+ with a simple linear trap are reviewed. This is followed by a discussion of our atomic source and the three methods used to create and trap barium ions, including: electron impact ionization, photoelectric impact ionization, and, most significantly, isotope selective photoionization. The chapter ends with notes on the construction of high-finesse cavities and our progress towards the integration of the same with a miniature ion trap.

Chapter 4 describes in detail the apparatus with which the Th^{3+} ion trapping experiment was conducted and the results we obtained. Three generations of ion traps are discussed, along with the technology required for their functionality. Techniques used for the generation of thorium ions by laser ablation are covered. Discussion of the lasers used in the observation of thorium ions is followed by a description of the effectiveness of cooling by collisions with helium atoms. Next the technology used for detection of ions, and observation of trap losses is covered. The Chapter concludes with an in depth look at some of the special methods used in the systematic search for, and eventual observation of, the Th^{3+} fluorescence frequencies of the 984 nm, 690 nm and 1087 nm lasers.

Chapter 5 will summarize the results and methods of the two experiments. This thesis will conclude with a look at the next few steps to be taken on both fronts. Attention is paid to the difficulties related to cost and observation in working with $^{229}Th^{3+}$ instead of $^{232}Th^{3+}$.

CHAPTER II

THEORY

This chapter reviews the theoretical framework of the experiment. First, an overview of the theory behind the radio-frequency (or Paul) style ion filter/trap will be given. This will be followed with an explanation of the operation of the various cooling mechanisms employed: buffer gas, laser cooling and sympathetic. The section on laser cooling will elaborate on the particulars of cooling three level atoms like those in Ba^+ and Th^{3+}, and techniques for eliminating the dark states arising from their Zeeman substructure. The Chapter concludes with a review of various sources of trapped ion loss and the dynamics of ion cloud to crystal phase transitions.

2.1 Radio-Frequency Ion Traps and Filters

Charged particles cannot be held in a stable equilibrium by electrostatic forces alone (see Earnshaw's theorem in [56]). Two of the most broadly used ion traps, the Penning and Paul style traps, each provide different methods of getting around this limitation. The Penning trap uses a confining electric potential along one axis then adds a magnetic field along that same axis. Ions trying to escape along either of the other two dimensions are forced into cyclotron-like motion in the plane and are thus confined.

The other widely used trap is the Paul trap. This uses oscillating high voltage fields applied to an array of electrodes. The typical oscillation frequencies are in the 0.5-50 MHz range. By oscillating the potentials applied to the electrodes a dynamic confinement may be obtained. The advantage of the Paul (or rf) trap is that it can be configured to admit a restricted range of charge-mass ratio ions. A three dimensional rf trap is also unique in its ability to confine both positive and negatively charged

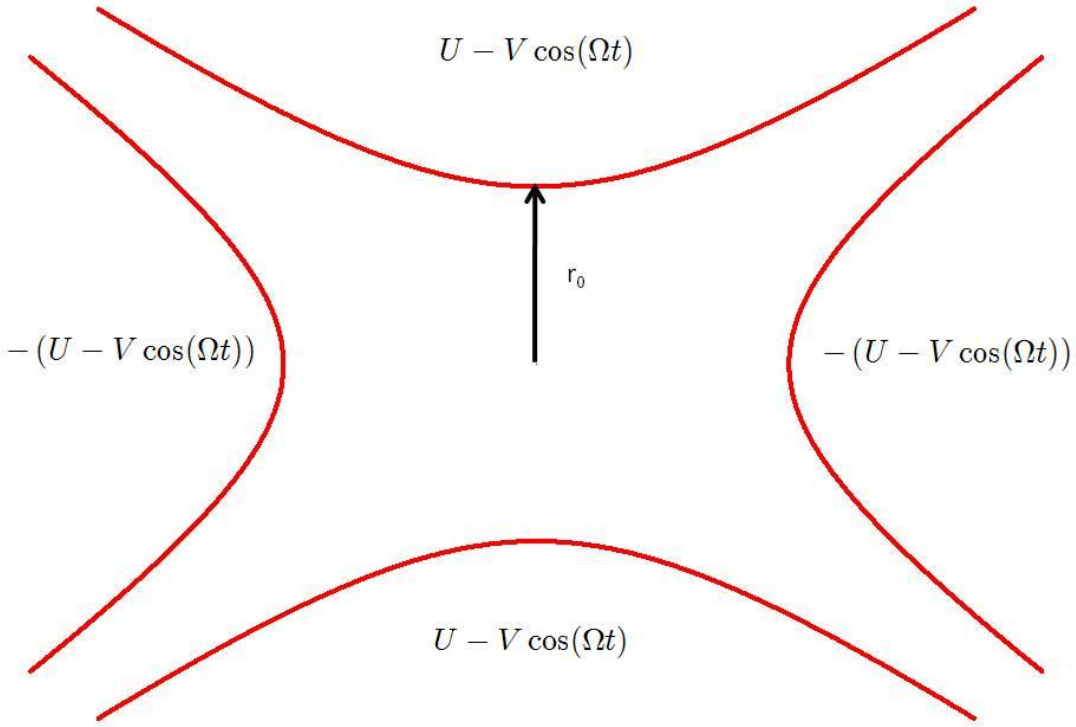

Figure 4: Cross section of an infinitely long 2-D mass filter. Hyperbolic electrodes have rf voltage of magnitude V at frequency Ω applied to them. The distance between the center of the trap and the nearest electrode surface is r_0.

particles without reconfiguration of its potentials.

Experiments in this thesis utilized three different 2-dimensional rf traps. These traps use both rf and dc trapping potentials and have a number advantages which make them attractive for use in atomic physics experiment. Some of these advantages include their their high trap depth and their ability to restrict the trapped ions to an easily reconfigurable charge/mass range.

The ideal 2-dimensional quadrupole mass filter is a configuration of four infinitely long electrodes arranged on the corners of a square with hyperbolic surfaces facing a common center. A cross section of the structure with the applied voltages can be seen in Fig. 4. The distance from the center to the nearest electrode surface will be called r_0. If a positive potential $V_0/2$ is placed on one pair of diagonally opposite

electrodes (along the x-axis) and $-V_0/2$ on the other set of rods along the y-axis then a potential of the form

$$\phi(x,y) = V_0 \frac{x^2 - y^2}{2r_0^2} \tag{9}$$

will fill the space between them. This is a saddle potential. It provides confinement for a positive charge along the x dimension but not y. If the potentials applied to each set of electrodes oscillate (at radial frequency Ω), then the confining dimension will oscillate between x and y. Of course, the time-averaged potential at any point will remain 0, but a charged particle with a given charge/mass (e/m) ratio will be trapped in a pseudopotential and follow a stable (ie, $x \nrightarrow \infty$ as $t \rightarrow \infty$) trajectory for a range of driving frequencies. This range is given by

$$\frac{e}{m} \gtrsim \frac{r_0^2 \Omega^2}{2.2V}. \tag{10}$$

A mechanical analog can be helpful for imagining how this works [57]. If a small spherical mass is place on a saddle shaped surface it will roll off. But if this surface is placed on a turntable and rotated, then for a range of angular frequencies the mass will be stable and exhibit small oscillations about the center of the surface.

By similarly adding a constant voltage $\pm U_{dc}/2$ to opposite electrodes we place a further restriction on which masses will be stable in the trap, this time limiting the upper bound on e/m, though this limit will depend on the the value of the rf voltage applied. With both V_{rf} and U_{dc} applied, the equations of motion become

$$\ddot{x} + \frac{e}{mr_0^2}\left(U - V cos\Omega t\right) x = 0 \tag{11}$$

$$\ddot{y} - \frac{e}{mr_0^2}\left(U - V cos\Omega t\right) y = 0. \tag{12}$$

Defining the following variables

$$a \equiv \frac{4eU}{mr_0^2\Omega^2} \tag{13}$$

$$q \equiv \frac{2eV}{mr_0^2\Omega^2} \tag{14}$$

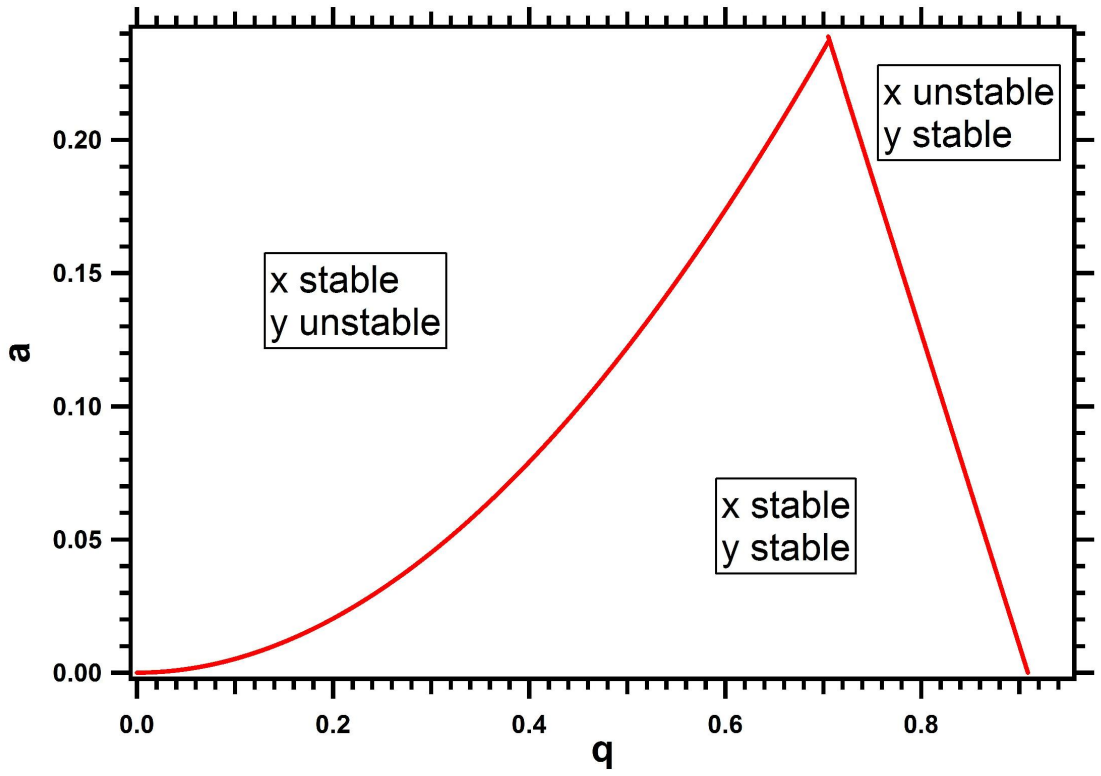

Figure 5: The 1^{st} stability zone of a 2-dimensional linear ion trap or mass filter. The ion will exhibit stable orbits when its a and q parameters lie in the area underneath the triangular shaped curve. Outside of this region, their orbital amplitudes increase exponentially until the ions crash into the trap electrodes.

we may cast equations (11) and (12) as the Mathieu equations

$$\frac{d^2x}{dx^2} + (a - 2q\cos 2\xi)\, x = 0 \tag{15}$$

$$\frac{d^2y}{dy^2} + (a - 2q\cos 2\xi)\, y = 0 \tag{16}$$

a and q are often referred to as the trap's *stability parameters*. Each of Eqns. 15 and 16 divide the a,q plane into regions of stability for the ions motion in the x and y directions. The regions of this plane which are stable for both coordinates are where these filters are operated. The stability zone closest to U_{dc},V_{rf}=0 is the most often used. In Fig. 5 the boundaries of this stability zone are shown.

Through careful selection of the trap parameters defined above this electrode structure may be used to pass some ions through and filter others. To get an idea

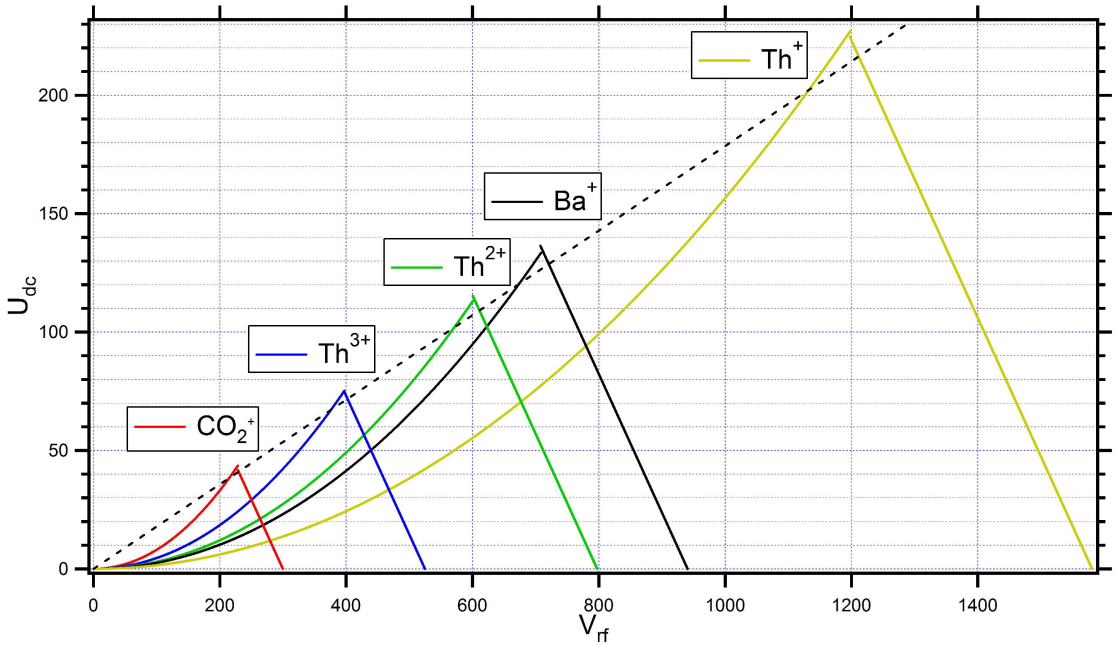

Figure 6: The 1^{st} stability zone for several ions as a function of the V_{rf} and U_{dc} voltages applied to the trap electrodes. The dashed line indicates the linear ramp along which a high degree of ion selection would be achieved. Other trap parameters were set to values typical for the traps in this experiment: $\Omega = 2\pi \cdot 2.2$ MHz and $r_0 = 2.77$ mm.

of how this works it is helpful to graph the stability boundaries in terms of the parameters U_{dc}, V_{rf} which can be modified most easily. Fig. 6 shows stability for various ions as a function of U_{dc} and V_{rf} with the trap size and driving frequency held fixed. The method used by most commercial mass filters or residual gas analyzers is to hold the ratio of U_{dc}/V_{rf} fixed and ramp both. As can be seen in Fig. 5, the voltage ramp passes through a region for each ion where it alone is stable in the trap. As this ramp is performed, an ion current is measured at the far end of the filter, generating a charge/mass spectrum for the injected ions.

To make the filter into a trap, two electrodes held at a positive voltage for positive ion confinement are placed along the length of the filter. A trap of this type was first described in [58]. A trap in this style which utilizes rf trapping along only two dimensions and uses a dc potential for confinement along the other is advantageous because a large number of ions may all may be at rest at a zero of the potential. This

is essential for sensitive spectroscopic applications where the rf field an ion experiences away from the trap center may have undesirable effects on the measurement being performed.

In this trap style, two strategies for ion ejection can be implemented; Fig. 6 will be helpful for visualizing these. Suppose an ion trap contained two species of ions with different charge/mass ratios e_1/m_1 and e_2/m_2, and it is desirable to keep Ion 1 and eject Ion 2. If $e_1/m_1 < e_2/m_2$ then we could increase U_{dc} until Ion 2 left the trap. For example if the ions were Th^{2+} and Th^{3+} and $V_{rf} = 400$ V; then, looking at the the graph of Fig 6, at $U_{dc} = 50$ V the Th^{2+} would leave the trap but the Th^{3+} would remain. If we wished to do the opposite, keep the Th^{2+} but eject the Th^{3+}, we could increase V_{rf} to about 550 V while holding U_{dc}=0.

Ions traversing a mass filter will undergo oscillations in the radial direction. The fundamental frequency of oscillation is called the secular frequency and is given for small values of a by

$$w_r = \frac{1}{\sqrt{2}} \frac{eV_0}{mr_0^2\Omega} \tag{17}$$

Higher frequency oscillations induced by the driving field are called *micromotion* [59]. Another mass-spectroscopic technique can be implemented by taking advantage of the mass dependence of the secular frequency. If trapped ions are exposed to a driving field along one trap axis which corresponds to the correct secular frequency, then the ion's displacement amplitude will increase until its kinetic energy exceeds that of the trap. If a small aperture is cut in the electrode along that axis then the ion may pass out of the trap and into a detection device. Use of this technique can create mass scans of great precision [60]. An equivalent scheme where the secular drive is held fixed and the rf voltage is ramped was used by our collaborators in this work and by [61].

Almost all real ion traps will suffer from some distortion from the ideal theory of the quadrupolar trap. The following are some of the most common distortions

observed. Because hyperbolic electrodes are expensive to machine, most often cylindrical rods are used instead. The ratio of the rod radius to the trap radius r_0 will determine the deviation from the ideal trap [62]. Also, in the theory of the trap presented above *ground* is located very far away, but in many traps a ground shield is placed just outside of the rods to minimize any background electric field in the trapping region. This can cause a shift in the boundary of the stability diagram [62]. Additional mixing of higher order multipole fields can occur when the positioning of the rods does not precisely place their centers on a the vertices of a square. By rotating one rod along the circumference of a circle passing through the rod centers a hexapole field can be added [63]. By shifting r_0 along one axis to be different from that of the other, octopole fields can be added [64]. These nonlinearities can be a boon for precision applications by, for example, forcing unstable ions out of the trap more quickly [65].

Though we do not need a high level of mass selection in this experiment, it is easy to see how it could be very beneficial for ion trapping experiments generally. For instance, if mass selection down to 1 amu could be achieved in our traps, then it would be possible to trap only the desirable isotopes of a particular ion. This may in fact become a requirement in the future, depending upon the purity of ^{229}Th samples which would be obtained.

Ion traps like the ones we used are extremely deep. With the secular frequency described in Eqn. 17, the depth of the harmonic pseudo-potential may be written

$$E = \frac{1}{2} m w_r^2 r_0^2 = k_B T \tag{18}$$

for the trap we utilized for trapping Th^{3+},

$$w_r = 2\pi \cdot 200\,\text{kHz},\ r_0 = 2.77\,\text{mm} \rightarrow T = 176,000\,\text{K} \tag{19}$$

This is quite deep compared with neutral atom traps, which have typical depths of a few mK. Along the axial direction, where the ions are confined by a DC potential,

typical trap frequencies for one of our traps were $\sim$ 20 kHz, but the length of the trap in that dimension was $\sim 20r_0$ so the depth is similar. It is also easy to increase this depth by adding more voltage to the endcaps, whereas the q stability parameter limits the maximum depth in the radial direction to

$$k_b T = \frac{1}{2} m \left(\frac{\Omega \, 0.92}{2\sqrt{2}} \right)^2 r_0^2 \tag{20}$$

since by Eqns. 14 and 17

$$w_r^2 = \frac{\Omega q}{2\sqrt{2}} \tag{21}$$

and the maximum value of q is $\sim$0.92.

The pseudo-potential picture begins to break down as large numbers of ions are loaded into the trap and inter-ion energies rise. In mass spectroscopic applications where a number of ions may occupy the trap at once, these effects can have noticeable effects on the mass-selection. Compensation for these effects by calculating corrections to the stability diagram (or secular frequency) are discussed in reference to a particular trap in [66] or more generally in [67]. Space-charge effects also set limits on the maximum number of ions any trap will be able to confine [68].

2.2 Ion Cooling and Heating

This section will review the motivations for cooling the trapped ions and the methods by which that cooling was accomplished. The first topic covered is a review of how ions may be heated or cooled via collisions with neutral particles or other ions. This will be followed by a review of laser cooling of trapped ions, both for two-level systems, and then for the more complicated case of lambda three-level systems.

Ions initially loaded into the trap may be very hot. If the ions are created in the trapping region via electron impact or photoionization, then their initial temperature will depend on where in the trap they were created. Given the depth of some ion traps stated above, the temperatures may be $>10^5$ K. Such temperatures generally

make observation of laser induced fluorescence difficult, due to large Doppler widths. The Doppler width is given by [69]

$$2\delta = \omega_0 \left(2 \ln (2) k_B T / mc^2\right)^{1/2} \tag{22}$$

where 2δ is the FWHM of the Doppler-broadened linewidth, ω_0 the natural linewidth and m the atomic mass. For example, the Doppler width of the one of relevant transitions at 690 nm in Th^{3+} (see 4.3) at 10^4 K is 2.0 GHz, which is exceedingly broad when compared with the natural linewidth of ~ 20 kHz.

2.2.1 Collisions with trapped ions

Collision based techniques for cooling, heating, interrogation or state changing of trapped ions have been used since the days of the first rf traps. The first theoretical treatment of the technique appeared in [70]. While the idea of introducing a buffer gas to cool might seem like a straightforward problem of thermal equilibrium, the model described in [70] suggests that this is not correct. The fact that the ions are in a trap rather dramatically changes the problem depending on the relationship between the mass of the ion m_I and the mass of the buffer gas m_B.

In the case where $m_I/m_B \ll 1$, after every collision the ion's velocity is totally randomized after each elastic collision with a fixed in position buffer gas atom. Averaging over a period of the rf cycle yields an exponentially increasing energy for the trapped ions. This heating is referred to as *rf heating*. In the opposite limit $m_I/m_b \gg 1$, the buffer gas atoms are assumed to be cold, and the ion's velocity is never totally randomized, but instead collisions will give rise to a velocity dependent force as in a viscous drag [70]. The secular motion is damped out exponentially, and the micromotion is unaffected. However, this model does not account for ion-ion collisions, which may be an important factor given the large number of confined ions in our Th^{3+} traps. The question of how to model ion-ion interaction along with the effects of ion-neutral collisions remained open for some time.

The trajectory of a single ion in a trap was next treated by [71]. In this work, the ion was found to undergo Brownian motion. Collisions with buffer gas atoms or random electric field noise, such as would be generated by the presence of other ions, are modeled as random forces on the ion. The long time stability of trapped ions was calculated as a function of the trap parameters a, q and the magnitude of the random forced impinging on the ion. The question of what heating rates we can expect for given cloud densities or buffer gases are not explicitly addressed, but the model does illustrate that rf heating by ion-ion collisions is driven by the existence of micromotion.

One of the first measurements of the equilibrium temperature of a cloud of ions as a function of helium buffer gas pressure was done in [72]. Temperatures were determined by observing the spacial extent of the trapped ion cloud by fluorescence imaging. The results show an inverse exponential relationship, with the energy asymptoting to a final value of 2 eV ($\approx 2.4 \cdot 10^4$ K) for buffer gas pressures of $>5 \cdot 10^{-6}$ torr.

In [73] and [74] Moriwaki *et al.* present new models, differing from those presented in [71] and [70]. These models were derived to describe the heating and cooling effects of light versus low mass buffer gases. The predictive power of these models was then tested against an experiment. In [74], the asymptotic temperature of a cloud of ions in a quadrupolar ions trap as a function of buffer gas was observed for several gases (H_2, He, CH_4). An equation for the 'critical pressure' at which this asymptote will occur was calculated.

The model in [73] was designed to simulate the effects of ion-ion collisions, ion-He cooling buffer gas collisions and ion-Kr heating buffer gas collisions. Both helium and krypton gas were added to a chamber containing an ion trap with Mg^+ ions. For a fixed pressure of Kr gas, the storage lifetime of the ion was measured as a function of He gas pressure. Loss of Mg ions due to non-heating mechanisms such as charge exchange (see Sec. 2.4) should not be prevalent since the ionization energy of Mg is

about half that of krypton. The hypothesis presented is that while the Kr gas will cause heating, this is partially counter-balanced by an evaporative cooling process. The Kr gas heats up the trapped ions at some constant rate, but the hottest ions are most likely to leave the trap leading to an equilibrium temperature condition. This model agrees with the storage lifetime data measured. Doppler temperatures were measured again for fixed Kr gas pressure as a function of He gas pressure, but no results were obtained which could justify the model's temperature predictions at low helium buffer gas pressures. However, this work suggests that the maximum real temperature observed for ions subjected to rf heating will be about 10% of the trap depth, and thereafter the temperature will remain constant as evaporative cooling balances heating effects. This result was confirmed in the paper [72] mentioned earlier. The easiest way to visualize this is that at 10% of the trap depth the tail of the Boltzmann temperature distribution with the hottest ions start to contain a non-negligible number of ions which are lost through collisions with the trap structure.

In [75], single barium ions were cooled using a helium buffer gas at a pressure of $4.8 \cdot 10^{-4}$ torr. At a pressure of $4.8 \cdot 10^{-4}$ the ions' measured Doppler temperature was 256 ± 10 K, although no measurable difference in ion temperature was observed between $5 \cdot 10^{-5}$ and $4 \cdot 10^{-3}$ torr. Ion loss rates were also investigated by including various partial pressures of argon and xenon. As expected, loss rates were higher when the heavier gases were included because a single collision between a barium ion and a xenon atom has a probability of ejecting the ion from the trap. It is still an open question, however, how much of the loss they observed for helium buffer gas is due to impurities causing charge exchange collisions versus unfavorable heating collisions. It is clear, from the varied temperatures observed in the papers cited above, that the final temperature of an ion being cooled by a buffer gas will depend on several factors. These will include the amplitude of the micromotion (determined by the particular trap's field structure) and the number of ions in the trap (with more ions leading

to greater fluctuations in the background electric field and thus greater heating as described in the previous paragraph).

2.2.2 Two-Level Laser Cooling

The minimum temperature achievable by buffer gas collisional cooling methods is limited roughly to the ambient chamber temperature. However, by employing laser cooling, temperatures in the mK regime can be readily obtained. In this section methods for using radiation pressure to cool atoms will be detailed.

The basic idea of radiation pressure cooling is simple. Suppose an atom interacts with a near resonant light beam with wave vector $\vec{k}$. Each photon absorbed from the laser gives the atom a momentum kick of $\hbar\vec{k}$ in the direction of the laser beam. If the subsequent excited state decay is via spontaneous emission, then the photon emission will be isotropic. Therefore, averaged over many absorption-emission cycles, the force exerted on the atom will be only in the direction of the laser beam. This co-called radiation force is given by momentum change per photon scattered, $\hbar k$, times the scattering rate, $\sigma\Gamma$,

$$\vec{F} = \hbar\,\vec{k}\,\sigma\Gamma. \tag{23}$$

Where $\tau = \Gamma^{-1}$ is the lifetime of the excited state and σ the average population of the excited state, given by [76]

$$\sigma = \frac{s/2}{1 + s + (2\delta/\Gamma)^2} \tag{24}$$

where δ is the detuning of the laser from the atomic resonance and s is the saturation parameter defined as

$$s = I/I_0 \tag{25}$$

$$I_0 = \frac{\pi hc}{3\lambda^3\tau}. \tag{26}$$

I_0 is the saturation intensity. The Rabi rate may be stated in terms of the saturation intensity as

$$\Omega = \Gamma\sqrt{\frac{I}{2I_s}}, \tag{27}$$

It is convenient to write the population in terms of the saturation parameter because the laser intensity is the most readily changed parameter when interacting with the atoms.

If the atom's velocity is opposite the laser's propagation direction then this force will slow the atom down. However, as the ion's velocity changes so will σ through the detuning parameter δ. The atomic transition is Doppler shifted by the atoms velocity, and the magnitude of the shift is given by

$$\delta_{Doppler} = \vec{k} \cdot \vec{v}. \tag{28}$$

Laser cooling was first achieved achieved in a Penning ion trap [1] shortly after a scheme for cooling of gases with atoms was proposed [77, 78]. Some more detailed theoretical formulations of the process followed shortly after [79, 80, 81]. In a trap the situation is a bit different from the free atom case. As bound ions oscillate in the trap, their velocity varies sinusoidally. If the laser is directed at trapped ions they will experience a force in the direction of the laser, so they will be heated for half of a trap cycle and cooled for the other half. The goal is to ensure that the cooling done as the ions move in the $-\vec{k}$ direction is greater than the heating done as the ions move in the $+\vec{k}$ direction. In order to remove heat from the system on average and cool the ions, the laser is tuned so below the atomic resonance for an atom at rest. The detuning which determines the excited state population σ is

$$\delta = \delta_0 + \delta_{Doppler} = \delta_0 + \vec{k} \cdot \vec{v}. \tag{29}$$

where δ_0 is the laser detuning with respect to the atomic resonance for an atom at rest. As the ions oscillate in the trap their detuning, and therefore σ, will also oscillate.

By setting $\delta_0 < 0$ it is ensured that δ is closer to 0 as the ions move opposite to $\vec{k}$. During this half of the cycle a small δ will imply a larger σ. In this way more photons are scattered as the ion moves opposite $\vec{k}$ than when it moves in the direction of $\vec{k}$. Note that this is valid only when the trap frequency is much smaller than the both the laser and the atomic linewidths, but for most ion traps, including ours, this is true.

A numerical simulation of ion cooling was performed using the theory outlined above. A particle with a mass and excited state lifetime equal to the 493 nm transition in a Ba^+ ion was set with an initial velocity in a harmonic oscillation with frequency 20 kHz. The goal is to observe how the oscillation damps out with time. Noteworthy though is that this model does not include any rf heating effects due to ion-ion or ion-neutral collisions. It also does not include micromotion, but as we typically cool along an axis where the confinement is not done by rf, the lack of micromotion should not subtract from the model's usefulness in describing our cooling. The model should be accurate for a single or a few ions in a trap with a vacuum pressure low enough that collisions with background gases are rare.

Fig. 7 shows the simulation's results. The ion is losing and gaining energy as it oscillates in the trap. As described above, the ion will be heated as it moves in the same direction as the laser and cooled when it moves in the opposite direction. Fig. 8 shows cooling with a fixed initial temperature as the laser detuning is varied. The initial temperature selected is quite high, but it is consistent with the trap depths we have (see Sec. 2.1). Given that an ion's initial temperature in a real trap will depend on where it was created in relation to the trap's extent, these temperatures are quite reasonable. As can be seen in the figure, the temperature after a few milliseconds cooling depends strongly on the laser detuning. Cooling is maximal for a fixed detuning of $\sim 100\,\Gamma$. It becomes substantially less rapid for detunings $< -100\Gamma$ as can be seen by the $\delta = -125\,\Gamma$ curve. If, instead of using a fixed detuning, we

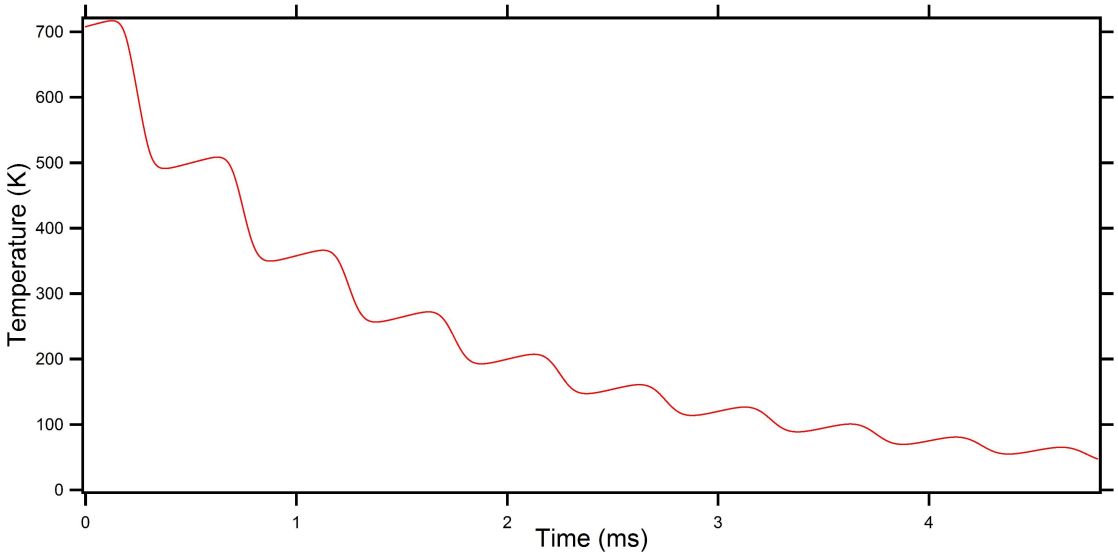

Figure 7: Laser cooling and heating during an ion's secular oscillation. In those parts where the ion is being heated it is moving in the same direction as the laser, during cooling it is moving in the opposite direction. In this trial the secular frequency was purposely set lower than the 20 kHz typical value in our traps to $\omega = 2\pi \cdot 2$ kHz so that the oscillations may be more readily observed.

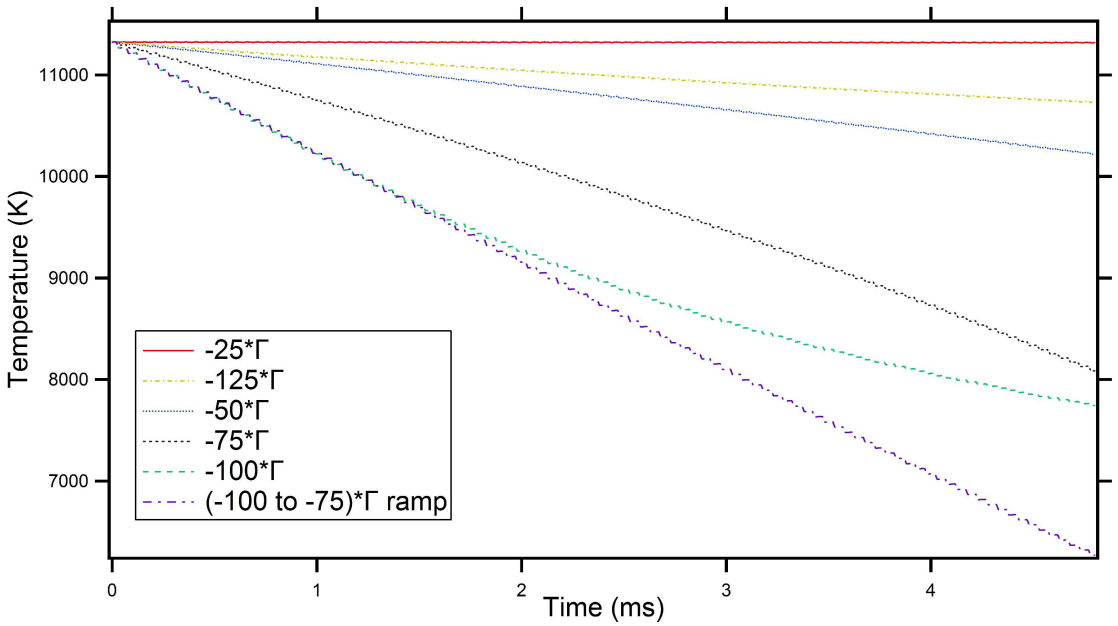

Figure 8: Laser cooling a trapped ion for variable laser detunings from the atomic line center. The initial energy of the ion was the same for each trial. Cooling proceeds more rapidly for larger detunings up to -100 Γ above which the effectiveness drops. The best cooling shown is the trial were the detuning was swept linearly from -100 Γ to -75 Γ. For all trials s=500 $\omega_0 = 2\pi \cdot 20$ kHz

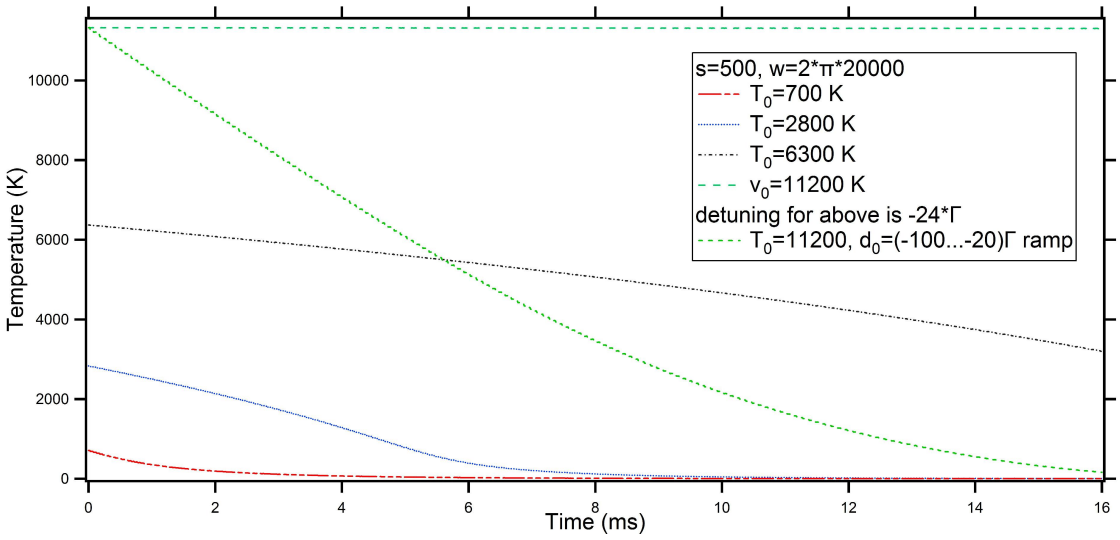

Figure 9: Laser cooling simulation varying initial temperature of the ion, holding $\delta = -25 * \Gamma$ s=500 $\omega_0 = 2\pi \cdot 20$ kHz constant, excepting for one trial were the detuning was again swept from -100 to -20 Γ

ramp the laser frequency linearly from from $\delta = -100\,\Gamma$ to $\delta = -75\,\Gamma$, we can get an even lower final temperature. The cooling for swept versus constant detuning are equal for early times, but the ramp adjustment keeps the cooling strong even as the ion gets colder.

In Fig. 9 the detuning is fixed at a value of $\delta = -25\,\Gamma$, and several plots are made of energy as a function of time for different initial temperatures. At higher initial temperatures the cooling is markedly less rapid in the 16 ms time window shown. For comparison, a plot is included where the detuning is ramped from $\delta = -100\,\Gamma ... -20\,\Gamma$. The lower final temperature when the detuning is ramped is apparent.

Some of the early theoretical formulations of cooling gave the following picture of cooling in traps: as the ion oscillates in the trap it receives a sharp kick as the Doppler shifted detuning crosses through 0 [81]. But this behavior is only observed for small laser detunings, and ions already at temperatures much smaller than the trap depth. The figures above are more representative of cooling in the hot ion temperature regimes where this experiment operates.

These Doppler-cooling based techniques have limits on the lowest temperature

they may achieve. The highest of these is called the *Doppler limit,* and it is given by

$$T_D = \frac{\hbar\Gamma}{2k_B}. \tag{30}$$

This limit is defined by the linewidth Γ. Its uncertainty inhibits further cooling near the Doppler limit. In Ba^+ there is a line at at $\lambda = 493$ nm connecting the ground $S_{1/2}$ and excited $P_{1/2}$ states for which $\Gamma = 2\pi\, 15$ MHz. This line will be used as an example to demonstrate the Doppler limit of laser-cooled trapped ions.

Suppose a Ba^+ ion is cooled to near the Doppler limit, for which $T_D = 380\ \mu$K. At this temperature the maximum velocity of the ion as it undergoes oscillations in the trap will be ~ 0.2 m/s. This corresponds to a maximum Doppler shift of $\vec{k}\cdot\vec{v} = 2\pi \cdot 0.42$ MHz. Looking at Eqn. 24, the $(2\delta/\Gamma)^2$ term in the denominator will therefore vary by less than 0.1% during the opposite phases of the ion's motion in the trap. Unlike in Fig. 7, where the ion was on average cooled over one oscillation, now the ion will experience as much heating as it moves opposite $\vec{k}$ as it does cooling when it moves in the direction of $\vec{k}$.

One additional limitation to reaching the Doppler limit temperature is that the atomic line must not be artificially broadened, for example, by power broadening. Power broadening of the atomic resonances natural linewidth occurs when intense monochromatic light on resonance is incident on the atom. The power broadened linewidth Γ' is given by [76]

$$\Gamma' = \Gamma\sqrt{1+s_0} \tag{31}$$

where s_0 is given by Eqn. 25. If broadening is present then the proper lower limit will be given by the Eqn. 30 but with the broadened linewidth Γ' replacing the natural width of the atomic resonance.

Utilizing more elaborate cooling schemes, temperatures lower than T_D may be achieved. The *recoil limit* is given by

$$T_r = \frac{\hbar^2 k^2}{k_B m}. \tag{32}$$

Where m is the mass of the atom or ion, and k is the wavenumber of the light with which the atom is being illuminated. The recoil limit is set by the minimum momentum kick an atom receives every time the atom absorbs or emits a photon. Because the atom absorbs or emits light in quanta of $p = \hbar k$, this is the minimum change in momentum. This minimum momentum change implies a minimum average kinetic energy of $\sim p^2/M$ associated with the absorption or decay of a single photon. For barium, using the transition at 493 nm, the recoil limited temperature is 0.6 μK.

2.2.3 Sympathetic Cooling

While ion-ion interactions have been shown to be a source of heating by Sec. 2.2.1, sympathetic cooling of trapped ions allows the inter-ion Coulomb force to be used for cooling. Suppose two ion species are present in the trap, and one is being laser cooled. The thermalization of the two ions, mediated by their Coulomb interaction, allows the ion species being laser cooled to damp out the motion of the other species which is not interacting with the laser. In this way, ions not amenable to laser cooling can be brought to the Doppler or recoil limit of another ion for which laser cooling is convenient. Implementation of this technique was first described by [82].

Sympathetic cooling was used to create an atomic clock based on a cold Al^+ ion. In [83], a single ion of aluminum and a single beryllium ion were loaded into the same trap. As the clock transition in the aluminum ion was driven, it was cooled sympathetically by its Coulomb interactions with the beryllium ion.

The radiation pressure force can also be used to shift the center of the harmonic trap for one ion species relative to another. In this way, different ion species can be segregated into different areas of the trap. In our experiment we used the radiation pressure force to (see Sec. 3.3) separate rare isotopes of barium using the more common ^{138}Ba isotope. The technique may find some use in the future for the cooling of Th^{3+} sympathetically by laser-cooled Ba^+, as discussed in Sec. 1.2.3.

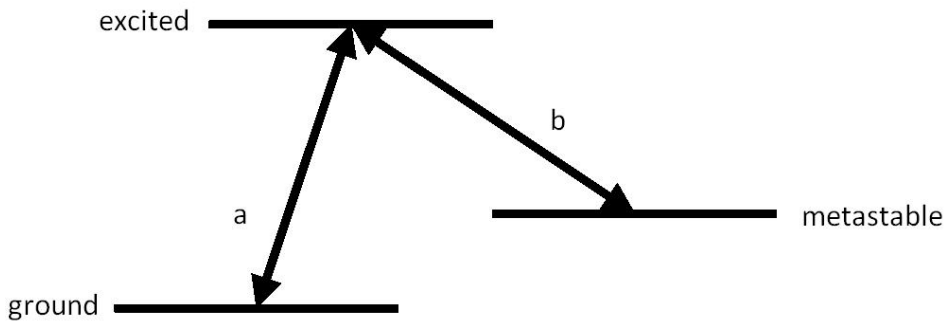

Figure 10: An atomic three level *lambda* system. It is characterized by the long-lived metastable intermediate level, necessitating two lasers for continuous observation. In this system coherent population trapping becomes an important consideration.

2.2.4 Three Level Cooling

Not all ions contain convenient closed two level systems on which they may be cooled. In both Ba^+ and Th^{3+} a three level atomic system was primarily used for cooling and observation. In both of these ions, an excited state is linked to a the ground state of the ion and also a metastable level of intermediate energy. A three level system of this type is called a lambda-system (Λ-system) (see Fig. 10). Both Ba^+ and Th^{3+} contain a lambda system. In Ba^+, the branching ratio, which determines the likelyhood of decay from the excited state to each of the lower levels, is 3:1. The first number in the ratio divided by the sum of both numbers yields the probability of a decay to the ground state. In Th^{3+}, the ratio was measured to be $\sim$1:10(1)(see Sec. 4.8). The probability of decay to the ground state is given by the first number divided by the sum of both numbers.

One complication encountered in cooling Λ-systems is coherent population trapping. A full treatment of this effect is given in [84]. When two laser fields coherent couple two different lower levels to a common upper state, certain combinations of

laser detunings will cause the population of the shared upper state to vanish. Because the radiation pressure force exerted on the ions, and the rate of cooling, depends on the excited state population (see Eqn. 23), coherent trapping of population must be avoided.

If the two applied lasers are denoted a and b with corresponding detunings δ_a and δ_b, Rabi frequencies (as in Eqn. 27) Ω_a and Ω_b and linewidths Γ_a and Γ_b then the excited state population σ_{22} as a function of these parameters is[84]

$$\sigma_{22} = N_{22}/D \tag{33}$$

$$N_{22} = 4\Omega_a^2\Omega_b^2\left(\Gamma_a+\Gamma_b\right)\left(\delta_a-\delta_b\right)^2 \tag{34}$$

$$\begin{aligned} D = \quad & \left(\delta_a-\delta_b\right)^2\left\{8\Omega_a^2\Omega_b^2\left(\Gamma_a+\Gamma_b\right)+16\Omega_a\Gamma_b\left[\left(\Gamma_a+\Gamma_b\right)^2+\delta_b^2\right]+\right. \\ & \left.16\Omega_b^2\Gamma_a\left[\left(\Gamma_a+\Gamma_b\right)^2+\delta_a^2\right]\right\}+8\left(\delta_a-\delta_b\right)\left(\Omega_a^4\delta_b\Gamma_b-\Omega_b^4\delta_a\Gamma_a\right)+ \\ & \left(\Omega_a^2\Gamma_b+\Omega_b^2\Gamma_a\right)\left(\Omega_a^2+\Omega_b^2\right)^2. \end{aligned} \tag{35}$$

The numerator N_{22} contains a factor which is the difference between the two laser detunings. As $\delta_a \rightarrow \delta_b$ then $N \rightarrow 0$, but $D \nrightarrow 0$. Therefore the excited state population $\sigma_{22} \rightarrow 0$. Fig. 11 shows the excited state population as a function of laser detunings, for Ba^+. The excited state population goes to zero where $\delta_a = \delta_b$. In this figure, the saturation parameters (see Eqn. 25) were both set to 100, which is typical in our experiment. It is noteworthy that even for a fairly high saturation parameter, where in the two-level case the excited state population would be very close to 0.5, here the maximum is 0.33. This amounts to about 33% less fluorescence and is about the best that can be achieved with this system. The particular detunings for which the maximal fluorescence is achieved will also depend very strongly on the branching ratio of the upper state and the powers used. If we increase the saturation parameter on Laser a to s=1000, then Fig. 12 shows the movement of the point with maximal excited state population.

Each of the three levels which make up the Λ-system may have Zeeman sublevels,

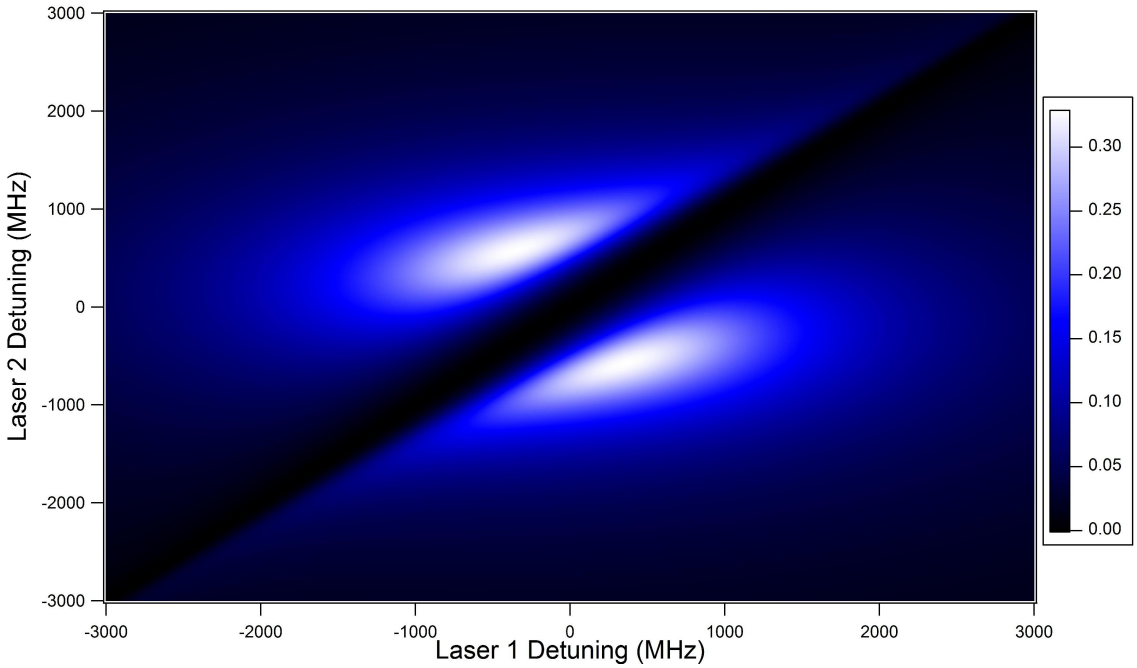

Figure 11: Excited state population for Λ-system with linewidth's set to the Ba^+ values and $s_a = 100$, $s_b = 100$. The x-axis is the a laser detuning and on the y axis is the b laser detuning. Coherent population trapping is evident for equal detunings in both lasers

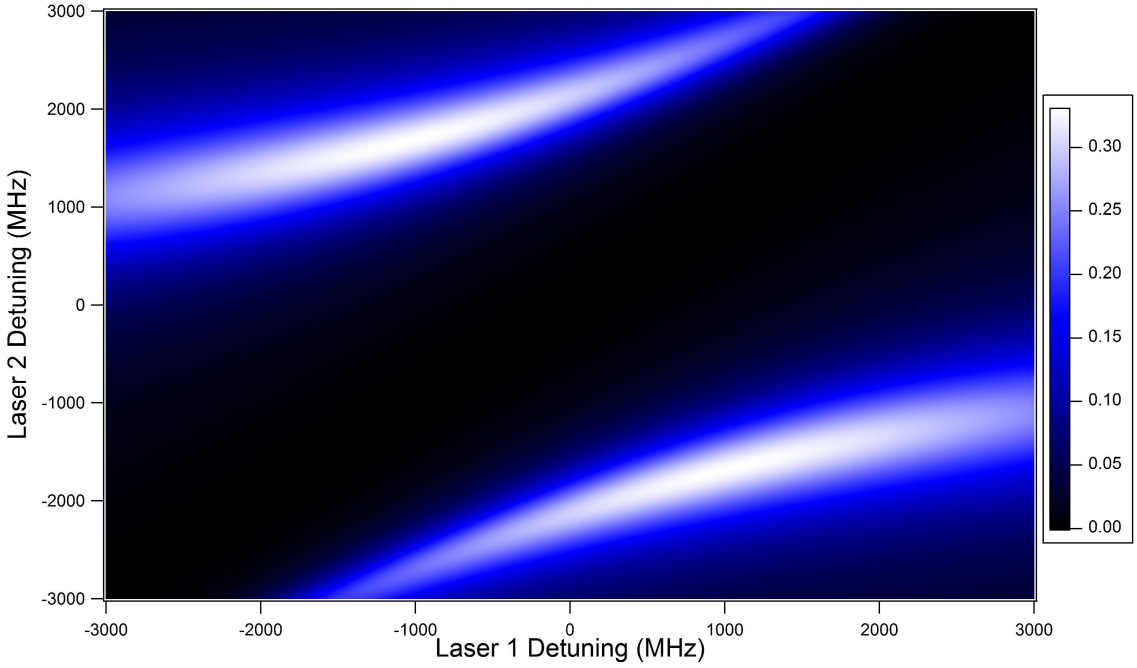

Figure 12: Similar to Fig. 11, except with $s_a = 1000$ and $s_b = 100$.

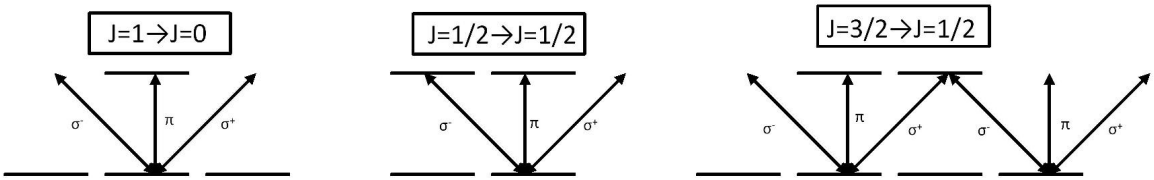

Figure 13: Dark states shown for ground→excited states with J= $1 \rightarrow 0$, $1/2 \rightarrow 1/2$ and $3/2 \rightarrow 1/2$. Arrows not attached to a available upper state will be *dark* to light of that particular polarization

which will split in energy if a magnetic field is present. Thereafter, instead of the single black band pictured in Figs. 11 and 12, there will be several different coherent population trapping resonances. For each combination of laser a and b frequencies which connect a ground state and metastable Zeeman sublevel, there will be a so-called dark resonance where the excited state population will go to 0. In [85] a scan of laser frequency at 493 nm in Ba^+ is shown where each of these dark resonances can resolved.

2.2.5 Dark States

Avoiding coherent population trapping is not sufficient for continuous observation of fluorescence from Ba^+ or Th^{3+}, dark states resulting from optical pumping must be avoided as well. Dark states [86] are superpositions of the atom's internal energy levels which are transparent to the laser impinging on the atom. They will exist on a given transition being driven for certain fixed laser polarizations if the number of Zeeman sub-levels present in the lower state is equal to or greater than the number of Zeeman sub-levels in the upper level. In the Λ-systems of both Ba^+ and Th^{3+}, the metastable state has more Zeeman sub-levels than the excited state. Fig. 13 shows some examples of atomic systems for which dark states will occur. The $D_{3/2} \rightarrow P_{1/2}$ transition in Ba^+ will have two dark states, which may be superpositions of the various Zeeman sub-levels, for any fixed polarization. For example, if using π-polarized light the dark states will be $|J = 3/2, m_J = \pm 3/2\rangle$.

Two methods are available for elimination of dark states. One way of eliminating the dark states is modulation of the polarization. Because the system's dark state depends on the polarization of the incident radiation, as seen in Fig. 13, polarization modulation is a straightforward way of making the dark states time dependent. However, care must be taken with the rate at which this is done. If the modulation is too slow (ie $\ll \Omega$, the Rabi frequency), then the excited state population will be greatly reduced because of the long time the system takes to evolve out of a dark state. Conversely, if the modulation frequency is $\gg \Omega$ then excited state population will remain low and the atom's emitted fluorescence will be diminished. Polarization modulation was not used in this experiment; instead, we used the alternative technique of applying a constant magnetic field to the ions.

In applying a magnetic field to the atoms, the dark states are made time-dependent. Suppose linearly polarized light is driving an atomic system with some dark states in its lower level. If the laser polarization makes an angle θ with the quantization axis of the atom and $\theta \neq 0, 90°$, then the dark state will be a superposition of the m_J quantum number sub-levels. If a magnetic field is applied along the atom's quantization axis, then each sub-level's energy will shift non-uniformly. The phase of each component of the dark-state superposition will oscillate at a different rate. In this way, the particular state which is dark becomes a function of time.

As an example, in [86], it was shown that in a two-level system with $J = 0$ in the lower level and $J = 1$ in the upper level, that for low light intensities (eg: $\Omega = \left(\sqrt{3}/5\right)\Gamma$, where Γ is the natural linewidth) that $\delta_B/\Gamma \approx 0.1$ was ideal, where δ_B is the Zeeman shift for a particular element of a dark state superposition. For Ba^+, a field of just a few gauss was ideal for typical light intensities applied to the atom. For Th^{3+}, the earth's magnetic field will be sufficient so long as the angle it makes with the laser polarization isn't very close to 0°.

2.3 Cold Ion Clouds and Crystals

In Sec. 2.2.1 the ion heating driven by its interaction with other ions in the same potential was discussed by viewing those other ions as contributing to a fluctuating background electric field, where the electric fields due to each individual ion mostly average each other out. In energy regimes where the kinetic energy is much greater than the Coulomb repulsion, and the number of ions per unit volume is large, this is a good approximation.

It was pointed out by Wigner in [87] that electrons bound by a common potential will form a crystal lattice if their density is below some critical value. In this lattice, the centers of charge would be fixed by the lattice potential and the spacing would be determined by the common harmonic well in which the electrons sit. Similarly, cold trapped ions can form a Wigner, or Coulomb, crystal where the positions of the charges remain in fixed positions with respect to each other. For arbitrary charged particles separated by an average distance r, an important figure of merit is the ratio (ε) of the particles' Coulomb (E_C) and kinetic energies (E_{kin}) [80]

$$\varepsilon = \frac{E_C}{E_{kin}} \tag{36}$$

$$E_C = \frac{1}{4\pi\epsilon_0}\frac{e^2}{r} \tag{37}$$

$$E_{kin} \simeq k_B T \tag{38}$$

thus

$$\varepsilon = \frac{1}{4\pi\epsilon_0}\frac{e^2}{r k_B T} \tag{39}$$

where we may also define a particle density $n = 4/3\pi r^3$. In [88] crystal structures were predicted for values of $\varepsilon \gtrsim 168$. However, even before a formal theory of trapped charged particle crystallization was developed, ordered structures in rf traps had been observed. In [89], crystallization of trapped 20 μm diameter aluminum particles was shown. These particles each had $\sim$ 350000 units of fundamental charge. Cooling of the particles was done by introducing some gas into the chamber and collisionally

cooling the particles as described in Sec. 2.2.1. Calculating ε above shows it to easily be much larger than 168 for any reasonable temperatures. Repeated formation and *melting* of the crystal in [89] was observed by introducing and then evacuating the gas from the chamber. Striking photographs of the ordered structures of many particles and the trajectories of single aluminum particles can be found in this paper.

Crystallization of singly charged ions requires much lower temperatures, typically ≤ 1 K according to Eqn. 39, using an ion spacing of 20 μm. The first reports of ordered ion structure in traps were in Penning-style traps owing to their lack of rf heating. Soon thereafter ordered structures of Mg^+ ions in an rf trap were observed [90].

The laser cooling rate, excited state population and observed fluorescence all depend strongly on an ion's velocity. Because the ion's velocity drops when the ions cross over from cloud to crystal, a fluorescence increase is observed. We observed this effect and it can be seen in Fig. 24. The trapping and cooling parameters required for inducing a phase change from a cloud to an ordered crystal exhibits strong hysteresis. While a crystal may be maintained for certain laser cooling and trap voltage settings, the rate of cooling at those same settings may be insufficient to make the phase change from an ion cloud. The phase change hysteresis, as a function of trapping potential and laser cooling rate, was explored in depth in [91].

Though the equations of motion for a single ion are simply given by the Mathieu equations of motion shown in Sec. 2.1 the motion of two or more ions is substantially more complicated. In [92, 93, 94] the interaction of two trapped ions was investigated and the dynamics found to be making changes from ordered to chaotic motion. When ε is high enough that a crystal no longer forms, the occasional hard collisions between the ions drive the chaotic motion of the two ions.

2.4 Sources of Ion Loss

2.4.1 Ion Heating

Two classes of mechanisms cause the loss of ions confined in an rf trap. The first is the result of heating sufficient to cause the ion to escape the trap. As stated above, rf traps used in our experiment are very deep ($> 10^5$ K) when operated at values of the q parameter appropriate for mass selection, $q \approx 0.71$. But the stability diagram (Fig. 6) shows, so long as no background fields are present, and U_{dc} is near 0, the rf voltage applied can be lowered a great deal without loss of confinement. At lower trap depths rf heating arising from collisions can be enough to drive the ions from the trap.

Lasers may also be tuned to heat the ions out of the trap. This technique was used extensively in our work with barium photoionization, described in Sec. 3.2.3. Chosen isotopes of Ba^+ were forced to leave the trap by tuning the cooling lasers to a frequency greater than atomic transition for that particular isotope. When our trap was operated at low values of V_{rf}, a few seconds of laser heating was enough for the undesirable ions to be ejected from the trap, leaving behind the rest of the ions. This heating proceeds quickly enough that other ions do not have time to be sympathetically heated by the ions being driven from the trap.

2.4.2 Ion Reactions

Reactions between trapped ions and residual gases left in the chamber were also observed. In the case of *charge exchange*[95], a trapped positive ion will absorb an electron from a neutral background atom; and if the trapping parameters (V_{rf}, U_{dc}) are such that the new ion is stable, it will remain in the trap. Collisions of this type will be energetically favorable when the trapped ion's state with one less unit of charge has a higher ionization energy than the atom or molecule with which it has collided. The problem of charge exchange with trapped ions has been studied for

some time [96], as typically these reactions are an undesirable source of trap loss.

When working with multiply charged ions charge exchange is of particular concern. Charge exchange collisions were particularly problematic in our work with Th^{3+}. The ionization energy of $Th^{2+} \rightarrow Th^{3+}$ is 17 eV, making a charge exchanging collision with background molecules such as N_2 and CO_2 very favorable. If the neutral atom source remains in operation after creation of multiply charged ions, inevitably charge exchange collisions will occur with the neutral products, eventually converting all of the higher charge states to 1+ ions. In Sec. 4.6 we review our direct observation the loss of trapped Th^{3+} ions through this mechanism. In [97], this was discussed in the context of the limitation of isotope selective photoionization trap loading of calcium. If a rare isotope of calcium is desired, then the rate of creation must be much higher than the rate of charge exchange. This situation is analogous to the problem of the creation of higher charged states via impact electron ionization of a neutral vapor. The technique of laser ablation employed for creation of thorium ions, reviewed in Sec. 4.2, alleviates this problem by creating the ions all at once, leaving very little neutral material left in the chamber after the ions are loaded.

Chemical reactions may also occur between trapped ions and neutral atoms. Whether an individual reaction will proceed may depend on several factors such as ion-neutral energy, charge state or even the internal electronic state of either the ion or neutral atom. One particular reaction we observed in our work was that of barium ions with neutral carbon dioxide molecules,

$$Ba^+ + CO_2 \rightarrow BaO^+ + CO. \tag{40}$$

Details of this observation are included in Sec. 4.4.

Although in our experiment chemical reactions are undesirable, the potential of ions traps to advance the study of cold ion-molecule reactions is considerable. Ion traps may provide an ideal environment in which the energies the reactants can be

carefully controlled and so that the quantum mechanical properties of chemical reactions may be studied, as in [98], where reactions between cold Ca^+ ions and CH_3F was studied.

2.5 Optical Cavities

In this section, the properties of standard Fabry-Perot cavities will be reviewed. The classical symmetric optical cavity consists of two concave mirrors (radius of curvature R) facing each other, separated by a distance L. Such a resonator will confine a stable gaussian mode of light with a wavelength λ when the cavity satisfies two conditions, as given by Siegman[99]:

$$0 \leq (1 - L/R)^2 \leq 1 \tag{41}$$

and (for perfectly reflecting mirrors)

$$L = m\lambda/2 \tag{42}$$

where m is any whole number. The parameter g will be useful in this section, it is defined to be

$$g \equiv 1 - L/R. \tag{43}$$

The three parameters which characterize a stable cavity are the free-spectral range (FSR), the cavity finesse $\mathcal{F}$, and the cavity linewidth κ. The free-spectral range is the radiation frequency difference between stable cavity modes. It is given by

$$FSR = \frac{c}{2L}. \tag{44}$$

It is equivalent to Eqn. 42 above with the substitution $m = 1$, $\lambda = c/\nu$. The finesse is given by

$$\mathcal{F} = \frac{2\pi}{2\delta} \tag{45}$$

where δ is the fractional power lost per mirror reflection due to transmission, absorption or scatter. A cavity constructed with high reflectivity mirrors therefore will have a high finesse.

In this experiment our mirrors have losses of about 0.01%, yielding a cavity with $\mathcal{F} \approx 3 \cdot 10^4$. State-of-the-art cavities constructed of similar materials and designed for near-IR wavelengths can achieve finesses about twenty times higher [100]. More exotic optical resonators such whispering-mode cavities can achieve finesses several orders of magnitude higher [101], but these cavities must overcome other challenges in attempting to couple atoms to their light.

The cavity's linewidth, κ, is given by

$$2\kappa = \frac{FSR}{\mathcal{F}}. \tag{46}$$

κ describes the relaxation of the Eqn. 42 requirement when the cavity mirrors are not perfectly reflecting. κ also describes the rate of light decay out of the cavity.

Mirror radii and spacing impose another requirement on light circulating in a cavity. The radiation's wavefront curvature must be properly matched the the curvature of the resonator mirrors in a stable cavity and this curvature is characterized by a parameter called the *beam waist*. The waist of a beam with a gaussian intensity profile is the radius of an aperture which will transmit 86% of the beam's power. The waist of a stable mode at the center of a symmetric resonator is given by [99]

$$w_0^2 = \frac{L\lambda}{\pi}\sqrt{\frac{1+g}{4(1-g)}} \tag{47}$$

and the waist at the surface of the reflectors is given by

$$w_1^2 = \frac{L\lambda}{\pi}\sqrt{\frac{1}{1-g^2}}. \tag{48}$$

In order for the light to be coupled into the cavity, light impinging on the back surface of a mirror must have a waist of w_1, and the correct convergence to match w_0 at the cavities center. Act of matching the beam's waists to those of an optical cavity is called *mode matching*.

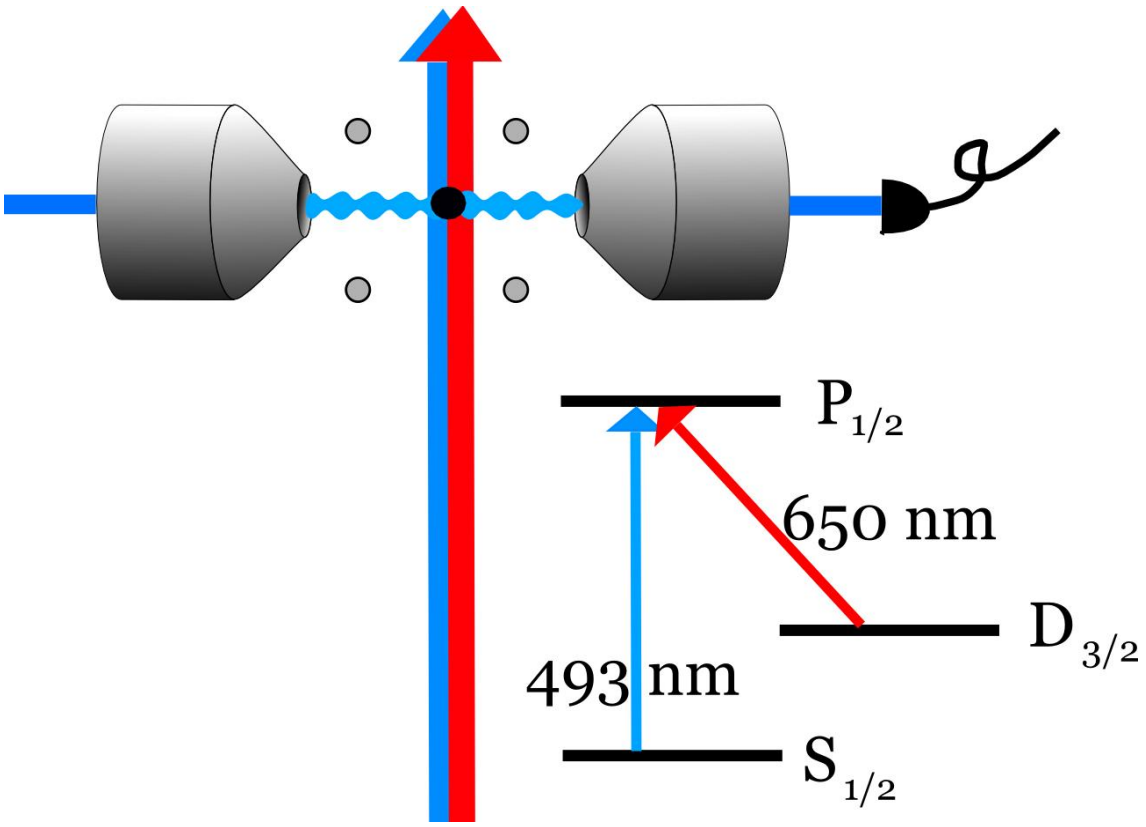

Figure 14: Ba^+ Cavity QED setup. A barium ion is confined to the region between four trap electrodes, inside of a high finesse optical cavity. The cavity is resonant with light near the 493 nm transition in Ba^+. The ion trap serves to position the ion at a maximum of the cavities standing wave. The precision of the placement will be in the Lamb-Dicke regime, where $\delta x \ll 493$ nm. The cavity's output is coupled to an optical fiber, allowing the light to be monitored or input to a copy of the system for remote entanglement.

2.6 Atom-Cavity Coupling

In this section the requirements for the generation of highly entangled states between single Ba^+ ion and a cavity photon will be reviewed. These requirements place a constraint on ratios between the strength of the atom-cavity coupling, the strength of the cavity's mode being coupled to the exterior environment (κ), and the strength of the atom's coupling to modes other than those of the cavity ($\sim$the atomic linewidth Γ for our cavities).

The strength of the coupling between the atom and the cavity is given by the

coherent coupling parameter g (not to be confused with the g in Sec. 2.5 above). It describes the coherent rate of oscillation between two states: one where the atom is excited and the cavity has no photon, and one where the atom is in its ground state and a single quanta of light at 493 nm is confined between the cavity mirrors.

Let $\psi(\vec{r})$ be the amplitude normalized cavity field amplitude at the ion's location $\vec{r}$. Then the cavity's mode volume V is given by:

$$V = \int |\psi(\vec{r})|^2 \, d\vec{r} \tag{49}$$

where the integration is over the region of space between the mirrors. Often this cavity field is a simple gaussian field mode, given by

$$\psi = cos(kz) \; exp\left(\frac{x^2 + y^2}{w_0^2}\right) \tag{50}$$

if z is along the cavity axis. In which case $V = \frac{\pi}{4} w_0^2 L$. With L the cavity length and w_0 the waist of it's mode as given by Eqn. 47.

With these definitions, the coherent coupling parameter g will be given by [102]:

$$g = g_0 \psi(\vec{r}) \tag{51}$$

$$g_0 = \mu \sqrt{\frac{ck}{2\epsilon_0 V \hbar}} \tag{52}$$

where $k = 2\pi/\lambda$ is the wavenumber of the atom/cavity light and μ is the electric dipole moment for the atomic transition resonant with the cavity. It is given by Metcalf [76]

$$\mu^2 = (3\pi\epsilon_0)\hbar\Gamma \, c^3 k^3 \tag{53}$$

and has a magnitude of $\sim e a_0$, with a_0 the bohr radius. These equations show that coupling is enhanced for a cavity with a small mode volume, and when the ion is located at a maximum of the cavity field.

As discussed in Sec. 1.1, the ability to control the trapped ion's position precisely (at a cavity field maximum) by applying voltages to the trap electrodes highlights

an advantage to working with ions as opposed to neutral atoms. In [22], an ion was used as a probe of a cavity field. A cavity was weakly excited with light resonant to the transition at 397 nm in Ca^+. By moving the ion through the cavity mode and monitoring the ion's fluorescence with a camera, both the transverse and longitudinal field amplitudes were measured to a precision of 40 nm, ten times smaller than the wavelength of the radiation.

The *strong coupling* regime is characterized by an atom-cavity coupling which is coherent for many atom-cavity flopping cycles before energy is lost through either spontaneous emission (at rate Γ) of the atom into non-cavity modes or loss through the cavity mirrors (at rate κ). This regime is characterized by two inequalities:

$$\frac{g^2}{\kappa\Gamma} \gg 1 \tag{54}$$

$$\frac{g}{\kappa} \gg 1 \tag{55}$$

The strong coupling regime is desired because it will allow an atomic superposition state to be mapped to a superposition of cavity photons with high fidelity.

The atomic state to be used in this mapping is the ground state hyperfine manifold of $^{137}Ba^+$, which possesses two states separated by 8 GHz. The spin up $|\uparrow\rangle$ and spin down $|\downarrow\rangle$ states will serve as a qubit.

This system will be able to execute a mapping of a coherent superposition of hyperfine ground states to a superposition of cavity photon states with 0 or 1 photon. This is performed as follows. Let a classical light field, at 493 nm, be incident on the atom from the side of the cavity as in Fig. 14. The tuning of this light will be such that it forms one leg of a Raman transition linking the $|\uparrow\rangle$ and the $P_{1/2}$ excited level in Ba^+. If the cavity is tuned to only link the excited $P_{1/2}$ state to the $|\downarrow\rangle$ then the initial hyperfine state superposition will be mapped to a superposition of $|0\rangle$ and $|1\rangle$

CHAPTER III

BARIUM ION CAVITY QED

This Chapter reviews the experimental apparatus of the Ba^+ ion trap cavity QED experiment. First, the chamber used to trap barium and test ionization schemes is described. This is followed by a description of the sources of neutral barium we employed and the ionization schemes utilized. These schemes include an ionization technique which used the photoelectric effect and a new method of isotope-selective photoionization we developed.

This Chapter also includes the methodology for the testing of high reflectivity mirrors will be covered and the construction high-finesse optical resonators. The Chapter concludes with a description of how the integration of a miniature ion trap and a small cavity will be accomplished in next stage of this experiment.

3.1 Barium Ion Trapping Vacuum Chamber

The first trap used in this experiment was a linear rf trap similar to one appearing in [103]. The trap, seen in Fig. 15, was made from four cylindrical rods cut from highly polished stainless steel wires(d= 0.84 mm). Two of the rods have a set of stainless steel tubes 8 mm long and separated by 8 mm slipped over them. The tubes are insulated from the rods with polyimide tubing and are held in place by friction. To avoid accumulation of charge on the polyimide insulator, care is taken to ensure none of the polymer is peaking out from under the tube. The rods are held in a square formation (side length 1.85 mm) by a larger alumina cylinder with four holes through it. The rods with the tubes slipped over them them are placed on diagonally opposite corners of the square. This rod arrangement defines a trap with $r_0 = 0.89$ mm and an axial length of $l = 8$ mm.

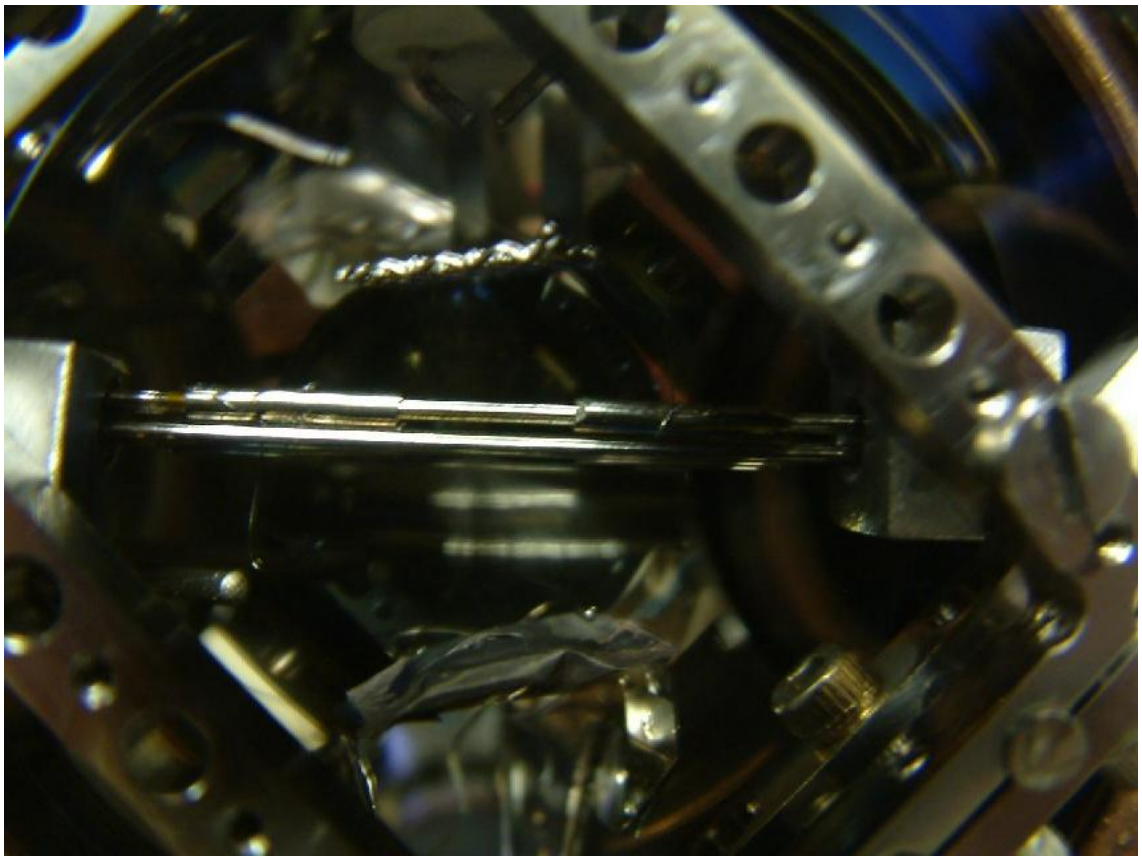

Figure 15: The first functional ion trap built for this experiment. It has a trap radius $r_0 = 0.89$ mm, length $l = 8$ mm and operates at a frequency $\Omega = 2\pi \cdot 6.6$ MHz. Above the trap is a tungsten filament used for electron-impact ionization. Below the trap is a small resistively heated barium oven. Cooling and photoionization light passes through the trap at 45° to its axis.

The alumina four-holed cylinder was purchased from Omega Engineering. Alumina is an ideal structural material for ion traps as it is non-porous and bakeable to very high temperatures, making its vacuum characteristics excellent. Additionally, it has a very low loss-tangent in the range of frequencies at which ion traps are typically operated (1-50 MHz), so it will not load the rf source driving the trap. It also has a high dielectric strength, which is important considering the high voltage difference (200 V_{rf} here) which may be applied to electrodes spaced <1 mm from each other.

The alumina cylinder is slipped into a hole cut in a stainless steel metal cube and held in place with a set screw. The face of the alumina is recessed far back into the metallic support structure to minimize charge collection on its face. The cubes which hold the alumina are supported by a rectangular bracket attached to the mounting grooves of the chamber. The barium oven source sits 1 cm below the trap and the electron gun sits 1 cm above. The connections for all of the rf rods and trap endcaps are spot welded to a high voltage feedthrough. Each of the rf carrying rods or endcaps may be biased individually to compensate for background electric fields.

The chamber used to house the first functional ion trap we constructed was a Magdeberg Hemisphere (Kimball Physics MCF450-MH10204/8-A). The chambers built by this company have grooves near each flange. They sell a series of clamps called 'groove grabbers' which made mounting and alignment of objects in the chamber much easier.

Cooling light passes through the trap at 45° to the trap axis. The cooling light beam was usually only focused along the shorter dimension of the trap so that we could illuminate as much of the trapping region as possible.

100 to 200 V_{rf} was applied to this trap for strong ion confinement. This voltage was applied to the two diagonally opposite pins without endcap electrodes on them. To generate this high voltage a rf signal at 6.6 MHz was generated (HP 8647 A signal generator) and amplified up to $\sim$5 W and then fed into a copper helical quarter-wave

Figure 16: Photograph of the quarter-wave coaxial resonator used to produce high voltage rf. It had a resonance quality factor Q$\approx$ 100 and was capable of outputting $>$200 V at 6.6 MHz. Rf was coupled into the low voltage end using a small loop antenna (pictured right) whose position was adjusted until coupling into the resonator was maximized. The weight of the helix is supported by three teflon 'combs.' Teflon is used for this purpose because of its low rf loss-tangent.

resonator (see Fig. 16). In [104], the design specifications for these resonators are given. The resonator is a copper tube with copper caps at both ends. It contains a helix of wire which is grounded to the tube at one end and at the other end passes through a hole cut into the cap. At the far end the helix is soldered to the ion trap electrode feedthrough. The resonator is fed by an antenna consisting of a few loops of wire at the grounded end. The resonator's length and the inductive coupling between the antenna and the helix are adjusted until the resonator and trap load are matched to the amplifier's source impedance (50 Ω). The coupling may be measured using a rf signal analyzer to send a frequency sweep into the resonator and monitor the back-reflected power as a function of frequency by using a directional coupler. The antenna is adjusted until the resonator is maximally coupled at some frequency. The rf source is then set to this frequency. This particular resonator has a 30 coil helix stretched over a tube of length 21 cm.

3.2 Barium Ion Generation

3.2.1 Atomic Barium Source

The source of neutral barium used in this experiment was a resistively-heated oven. A thin sheet (0.001" thick) of stainless steel or tantalum foil is first rolled into a tube. One end of the tube is folded over and sealed with a spot welder. Small chips of barium metal are inserted into the other end. The end is then spot welded shut and attached to a set of leads so that current may be run through the foil. A small hole or slit is cutin the side of the oven which will face the trap. Running 5 to 9 A of current through the oven will bring it to 300°C. This produced a sufficient flux of barium to obtain electron impact ionization rate of ∼0.05 ions/s for oven-trap separations of 25 mm.

The oven must be filled without exposing the barium air, as it will oxidize very quickly. A clean barium surface will turn white and be covered with barium oxide in

as little as a minute in atmosphere. We purchased a rod of barium from Alfa-Aesar. It comes with its surface completely oxidized, so it must be carefully scraped clean then carved under a atmosphere free of oxygen. Barium metal is quite soft, so this can be done with a razor blade. The cleaning and cutting was performed in a glove bag which was filled with nitrogen to prevent oxidation.

Even if the barium is cut and cleaned in a nearly oxygen-free environment it is very challenging to avoid leaving a layer of barium-oxide on the surface of any chips inserted into the oven. This oxide layer may be ruptured by heating up the oven to a temperature of $\sim$600°C. However, this must be done with great caution. As soon as the oxide layer is broken the flux of barium will be quite high and there is a risk of coating the trap or nearby vacuum windows with a layer of barium. In the chamber described above this occurred, and the front window was made completely opaque with barium. Fortunately, by heating the window face to $\gtrsim$ 300°C for several hours, the barium was driven off from the viewport and the chamber did not need to be disassembled.

3.2.2 Electron Impact Ionization

Electron impact ionization is the most easily implemented method of creating Ba^+. By resistively heating a thin wire of a material with a low thermionic work function, and placing a positively biased electrode nearby, electrons can be drawn off from the wire. We used either tungsten or thoriated tungsten for our filaments. Thoriated tungsten is a more expensive wire but it will emit electrons at lower temperature, extending the life of the filament. The electrode used to draw the electrons away from the filament is either made of a wire mesh, which some fraction of the electrons pass through, or is plate with a hole punched in it. The voltage difference between the filament and the electrode will set the potential energy of the electrons. This potential should be set to a value greater than the ionization energy of the atom to

be trapped. The ionization energy of barium is 5.2 eV, and typically the electron energy was set to ∼30 eV.

While electron-impact ionization is easily implemented, it suffers from several drawbacks. It is vital that no insulating materials are near the ion trap, or the electrons will build up on those surfaces. Depending on the electron current being generated, which is typically in the 50 μA to 1 mA range, this charge buildup may be rapid enough that it destabilizes the ions in the trap entirely after only a few second of running the beam. The charging effect may be directly observed by observing the position of a trapped ion immediately after loading. The apparent center of the trap, inferred by the ion's position, was observed to move up to 200 μm over a few seconds after the filament was switched off.

Surface charging makes it very easy to ruin an ion trap. If, after using the oven for any extended period of time under vacuum the chamber is opened to atmosphere, the barium layer deposited by the oven on to the trap electrodes will oxidize rapidly. If the trap is not subsequently cleaned, its surface will be coated thereafter in barium-oxide, which is an insulator. This makes the electron gun almost entirely unusable when the system is pumped back down, because charge will accumulate on every surface which has a coating of BaO.

Another impact ionization technique we employed takes advantage of the low 2.7 eV photoelectric work function of bulk barium. We observed that shining a halogen lamp (Thorlabs UV75) into the chamber, aimed at the trap electrodes with the barium oven in operation, would produce many more barium ions per unit time than the electron beam would. Since the vacuum chamber windows do not transmit light with a wavelength below 300 nm, and the lamp's spectrum spans the range of 200 nm to 540 nm, the radiation responsible must be in the range of 300 nm to 540 nm. The work function of stainless steel is too high (5 eV) to eject photoelectrons in this energy range, but barium's is not. Additionally, 300 nm is not a short enough

Table 1: Barium's naturally occurring isotopes

Isotope	Nuclear Spin	Abundance(%)
^{138}Ba	0	71
^{137}Ba	3/2	11
^{136}Ba	0	8
^{135}Ba	3/2	6
^{134}Ba	0	2

wavelength for the mechanism to be photoionization, as barium's ionization energy is 5.2 eV (237 nm).

The photoelectric effect was responsible for this ionization. Electrons are emitted from surfaces with deposited low work-function barium, accelerated by the high voltage rf and ionize barium atoms by electron impact. By biasing one of the trap's conductors with a positive voltage we where able to collect a current when the lamp was in operation. This current was comparable to the electron beam emission current. The loading rate observed using this technique was 2.4(3) ions/s, about a hundred times higher than the electron beam loading rate.

Because this technique also creates electrons, it will cause the same charging as the electron emission filament. However, since only those regions where barium has been deposited emit electrons, and because it is easier to control which parts of the chamber the lamp's light falls on, we observe far less charging using this technique than we observed using the filament. The technique's main drawback is the requirement that the trap be coated with a low work function metal, which is not feasible in many circumstances.

3.2.3 Barium Photoionization

Both of the electron-impact techniques discussed suffer from their inability to selectively load particular desired isotopes of barium. Barium comes naturally in any one of 5 isotopes with abundances greater than 2%(see Table 1). Since only those isotopes with nuclear spin can be used to map an atomic hyperfine ground state onto a cavity

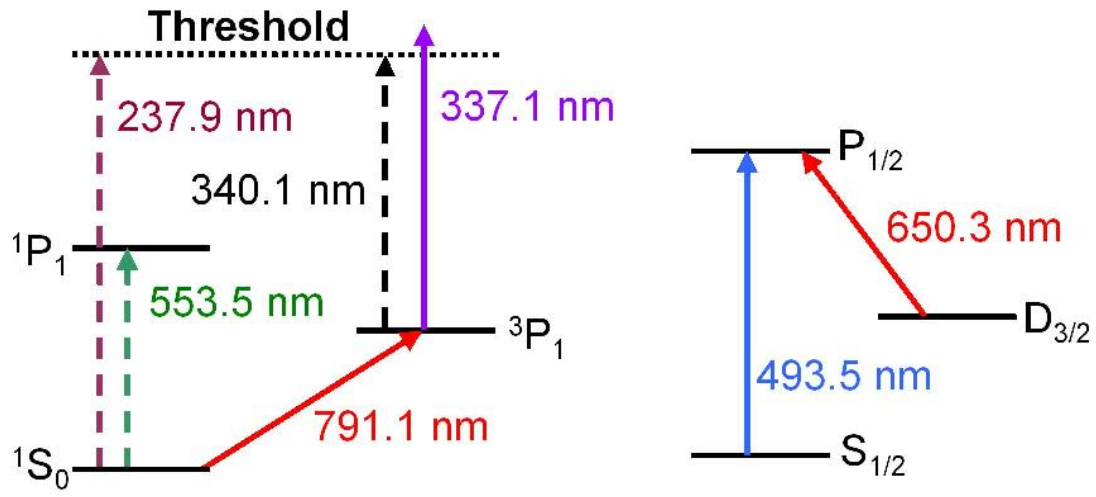

Figure 17: Relevant energy levels of neutral barium(left) and Ba^+(right). Solid lines indicate lasers used in this experiment. Photoionization proceeds by a transition at 791 nm followed by a nitrogen laser at 337 nm. Cooling of barium is done on a Λ-system, requiring lasers at 493 nm and 650 nm. The $D_{3/2}$ level in Ba^+ is metastable with a lifetime of $\tau = 89$ s [105]

photon state, the ability to load a particular desired isotope would be helpful.

More importantly, the influence of cavity mirrors on the trapped ions is of particular concern in this experiment, and electron impact based ionization techniques would greatly exacerbate mirror surface charging. This charge accumulation, in turn, would destabilize trapped ions and cause them to leave the trap. Also, for an equivalent flux of neutral atoms being emitted by the oven the photoionization technique also offers a much greater loading rate ($\sim$10 ions/s) than electron impact based ionization. Therefore, the barium oven can be run at lower temperatures during trap loading, extending the length of time before mirror performance is degraded due to accumulation of barium on its surface.

Energy level diagrams for Ba and Ba^+ are shown in Fig. 17. Previously implemented schemes for barium photoionization have utilized the strong dipole transition at 553 nm [106], but producing laser light at this wavelength is expensive, as the only option presently is a dye laser. Instead, we developed a new scheme which excites a narrow intercombination transition at 791 nm followed by an excitation above the

ionization threshold by a nitrogen pulse laser at 337 nm(Stanford Research Systems NL100). The use of this technique was first reported by us in [107]. The wavelength of the 791 nm transition and the isotope shifts were previously measured in [108] and the linewidth was found to be 50 kHz by [109].

We built a vapor cell for neutral barium to serve as an absolute frequency reference for the 791 nm laser. The construction of vapor cells for any alkaline-earth metals pose some challenges. First, creation of a vapor sufficiently dense for saturated absorption spectroscopy requires high temperatures. For barium >800°C is required. Any vacuum seals must be able to withstand these high temperatures or be isolated from the hot parts of the cell. Also, at high temperatures alkaline-earth vapors react corrosively with silicate based windows; but even if a non-reactive glass is used, the windows must be kept hot enough to prevent a metal film from forming on them (see [110]), or the viewports must be isolated from the vapor, as they are in a heat pipe [111].

The cell we constructed was substantially simpler these alternatives and can be seen in Fig. 18. The central region contains a rolled tube of stainless steel foil, 37 mm long, with the ends spot welded shut and a long slit cut in its top. The middle half of the cell is heated with a ceramic coaxial heater, causing barium to emitted from the crucible. Baffles are inserted to the left and right of the heated region, and the design and placement of the baffles is such that no line of sight exists from the hot central wall regions to the windows. The mean free path of a gas atom at the densities we produce is many times longer than the radial dimension of the heated region, making rare any atom-atom collisions which would lead to metal buildup outside of the baffled central region. Passive air cooling is sufficient to keep the conflat flanges to the left and right of the heated region below 550°C.

We obtain excellent saturated absorption signals from the cell when it is heated above 800°C. In Fig. 19 a saturated absorption scan over the 791 nm transition is

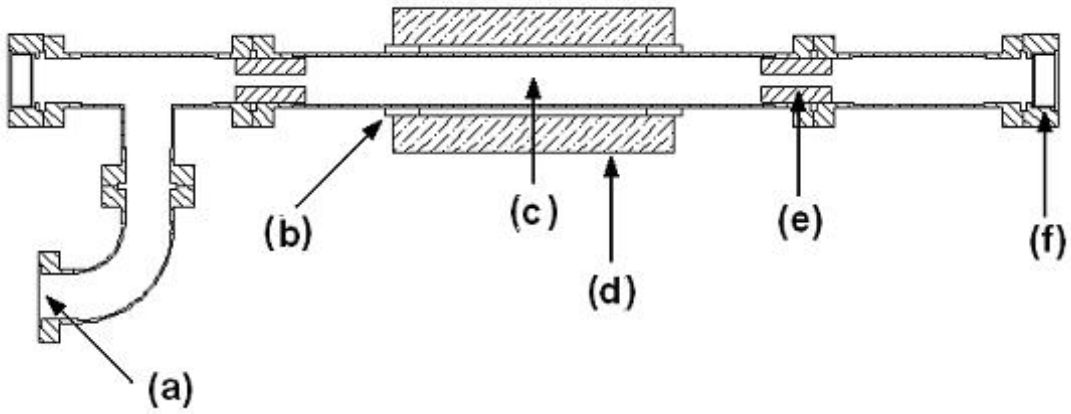

Figure 18: Diagram of the barium vapor cell used. This design would be in fact suitable for any alkali earth metal. The chamber was pumped out through a valve at (a). (b) is the set of resistive heating coils. (c) is the hot region of the chamber with the metal crucible. (d) is the ceramic shield surrounding the hot region. (e) is one of the two baffles which restricts metal vapor from having a line of sight from a hot region of the trap to one of the vacuum windows (f).

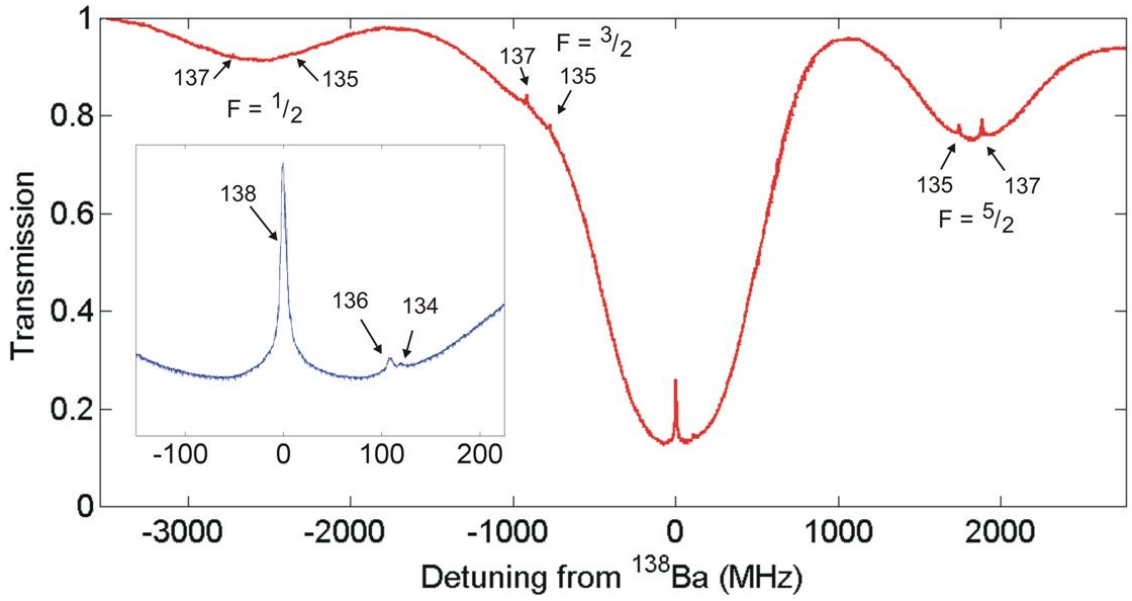

Figure 19: Scan over the barium 791 nm intercombination line. The line centers for each isotope with an abundance of >1% are visible, and the inset shows a zoomed in view of the scan near 0 detuning (relative to the ^{138}Ba line center).

shown from an earlier iteration of the vapor cell design. The only difference between Fig. 18 and the earlier iteration was that originally the vacuum flanges were closer to the heated region of the chamber, eventually causing the vacuum seal to fail.

Doppler free peaks from all isotopes with abundances grater than 1% are visible in Fig. 19. The peaks from the odd isotopes are spit in three positions because in those isotopes $I = 3/2$. So for the upper state, $^3P_1$, of this transition, $F = 1/2$, $3/2$ or $5/2$.

Photoionization was achieved by overlapping the 791 nm laser beam and the focused nitrogen pulse laser inside the ion trap. To load a desired isotope the vapor cell was used to tune the 791 nm laser to that isotope's saturated absorption peak. The isotope shifts for this transition, given by [108], are all separated by isotopte shifts >100 MHz. Given the natural linewidth of 50 kHz, the ultimate ability of this scheme to selectively ionize a particular isotope should be quite good. However, in our setup, transit broadening, power broadening and Doppler broadening all contribute to a reduction in the isotope selectivity of the photoionization.

Fig. 20 shows the loading efficiencies for each of ^{138}Ba, ^{136}Ba, ^{134}Ba as a function of 791 nm laser detuning. This data was taken with a laser power of 100 μW, which gives a focused peak intensity, I=325 mW/cm^2 and a power broadened linewidth of 7.6 MHz. The majority of the observed broadening is due to the divergence of the atoms emerging from the oven. Although the 791 nm laser beam was aligned orthogonally to the atomic beam, the divergence of the atomic beam ($\theta \sim 0.3$ rad) at the most probable velocity of 320 m/s for barium atoms at 300°C yields an expected Doppler FWHM of 102 MHz. This is in excellent agreement with the best fit to the data of 100 MHz FWHM. Additionally, the observed isotope shifts (relative to the ^{138}Ba$^+$ line center) were found to be 103(7), 95(5), and 4(5) MHz, not far from the shifts reported in [108] of 122, 109, and 0 MHz. The isotopic identification of a particular trapped ion was done by observation of the isotope shifts in the trapped ion's cooling light at 493 nm and 640 nm.

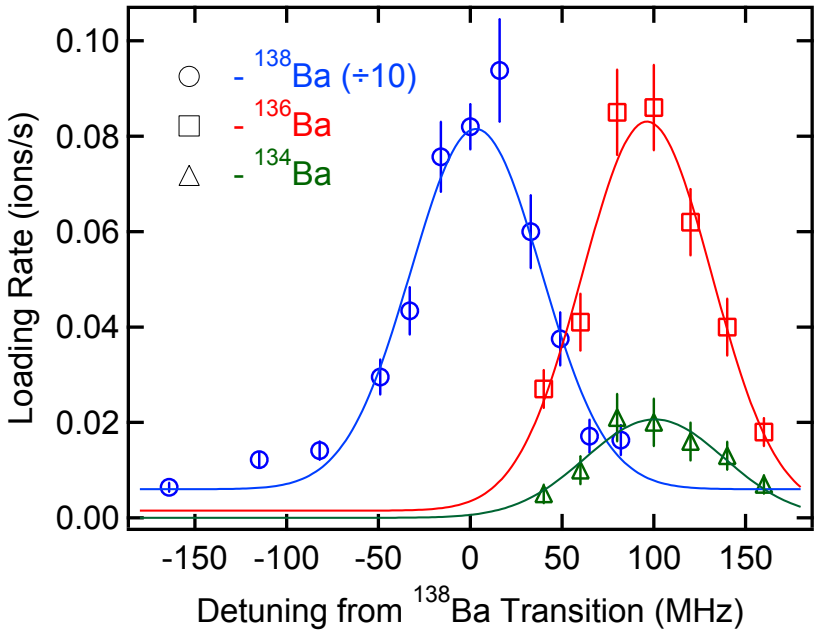

Figure 20: Photoionization spectrum for barium isotopes ^{138}Ba, ^{136}Ba and ^{134}Ba. The width of each peak is determined by the Doppler broadening of neutral atoms being emitted from the oven. Ions may be distinguished after loading by their isotope shifts on the cooling light transitions at 493 nm and 650 nm

Isotopes ^{135}Ba and ^{137}Ba were also loaded. Because of the hyperfine structure present in these isotopes, a more complex laser setup would be required for the observation of fluorescence. Instead of implementing this, the procedure was as follows: first, a number of $^{138}Ba^{+}$ ions were loaded and cooled into a crystal. Then photoionization was attempted in the vicinity of one of the these isotope's 791 nm lines. The odd isotopes where cooled sympathetically by the $^{138}Ba^{+}$ ions and were then counted by observing the number of dark spots in the ion crystal. The loading rates inferred from this technique can be seen in Fig. 21. This technique precludes the distinguishing of $^{135}Ba^{+}$ from $^{137}Ba^{+}$, but the two peaked feature of the data suggests selective loading of these isotopes as well.

This Doppler broadening due to the divergence of the beam could be eliminated with a straightforward collimation of the atomic source and does not represent any intrinsic limitation of the technique. But even with the limitation of the current setup

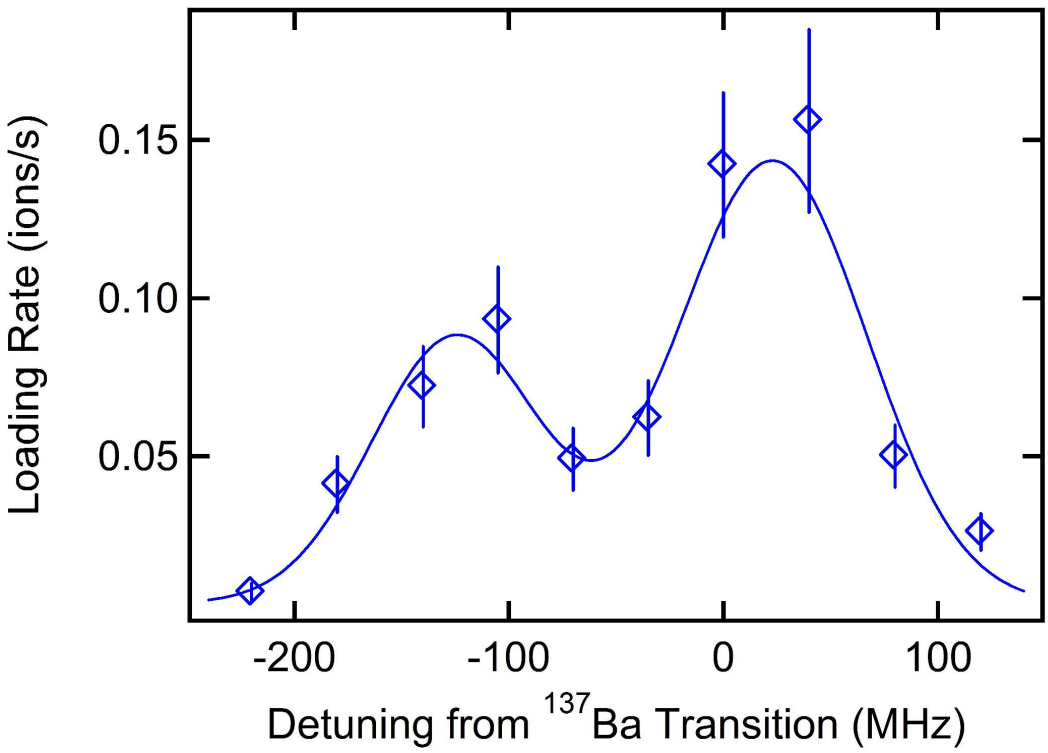

Figure 21: Photoionization efficiency of barium isotopes ^{137}Ba and ^{135}Ba. The ions are not distinguishable in our setup, but their detunings (given by the center of each peak here) are consistent with the values given in [108]

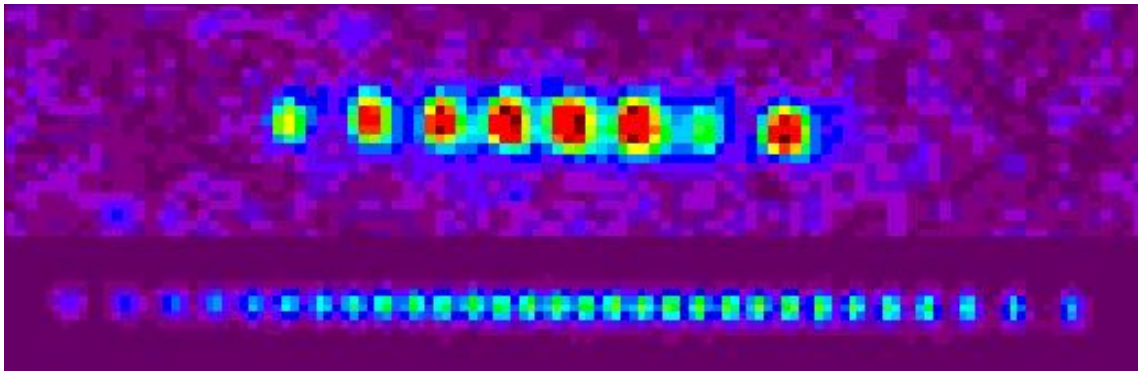

Figure 22: (Upper) Mixed crystal of ^{138}Ba and ^{136}Ba. (Lower) Pure crystal of 30 ^{138}Ba ions produced by photoionization.

a large degree of selection can be obtained. In Fig. 22 coulomb crystals of ions loaded using this technique can be seen. The creation of a 30 ion isotopically pure crystal as in Fig. 22(b) would have been highly improbable without the isotope selection offered by this technique.

3.3 Barium Laser Cooling and Detection

The simplest setup for cooling Ba^+ requires two lasers. The relevant energy levels can be seen in Fig. 17. A laser at 493 nm drives the $S_{1/2} \rightarrow P_{1/2}$ transition and one at 650 nm drives the $D_{3/2} \rightarrow P_{1/2}$ transition. The shared upper state has an 8 ns lifetime and a branching ratio of 3:1 favoring the 493 nm line. The 650 nm laser is a Toptica DL100 diode laser in the Littrow configuration. The laser is controlled with Toptica's grating piezo, temperature and current circuits. Second harmonic generation used to generate light at 493 nm was also purchased from Toptica. Light from a diode at 986 nm is coupled into a bow tie cavity which contains a potassium niobate ($KNbO_3$) crystal. With the crystal and cavity optimally tuned, $\sim$70 mW of 986 light is converted to $\sim$20 mW of 493 nm light. A PID feedback circuit issues control voltages to a piezo behind one of the cavity mirrors, locking the cavity to the 986 nm laser.

Finding the correct wavelengths near 493 nm and 650 nm for observation of fluorescence required a frequency reference. An optogalvanic cell is used as such a reference in many laboratories trapping barium ions. In this setup, the current in a barium gas discharge is monitored as a laser is passed through the vapor. The monitored current will be modulated if the laser light is at a wavelength of an atomic transition of a discharge product. This modulation signal may be used to lock the laser. The advantage of this technique is that the lock is direct to the atomic line. However, the broad width of the transitions, due to the high temperature in the gas discharge, can make acquisition of a narrow laser lock challenging. The optogalvanic technique was not used in this experiment.

A glass cell containing tellurium (purchased from Opthos Instruments) is another option. Molecular tellurium is rich in lines near 493 nm; the line nearest to the transition in Ba^+ is detuned by 300 MHz [85]. The cell must be heated to over 500°C to generate sufficient optical density for observation of saturated absorption. In the saturated absorption setup, one probe beam was deflected and modulated by an acousto-optic modulator (AOM) then set to overlap with the pump. A second beam was passed through the cell not overlapping with the pump. Both probe beams were input to an auto-balanced photoreceiver (New Focus Nirvana 2007). The photoreceiver's output was input to a lock-in amplifier (Stanford Research Systems SR830), which generated a dispersive signal to which the 493 nm laser was locked. To lock the 650 nm laser, an iodine cell may be used in the same way. However, iodine has sufficient vapor pressure at room temperature to obtain saturated signals.

On a day-to-day basis the vapor cells were not required. Using a wavemeter (High-Finesse WS7), which had an absolute accuracy of ∼200 MHz, the correct frequencies could be found most often by simply loading the ion trap with barium and searching around in frequency space for a minute or two until fluorescence was observed.

On the transition driven by the 650 nm laser there are more states in the lower

metastable $D_{3/2}$ level than there are in the upper $P_{1/2}$ level. This results in two dark states arising from optical pumping for any fixed 650 nm light polarization, as described in Sec. 2.2.5. In order to observe fluorescence continuously, either the polarization of the 650 nm laser must be modulated (using, for instance, an electro-optic modulator) or a magnetic field must be applied, making the dark states time dependent. In this experiment we used a magnetic field to destabilize the dark states. The applied field is a few gauss in magnitude and is applied perpendicular to the trap's axis by running $\sim$5 A through a few coils of copper wire wound around the chamber. The polarization of the 650 nm light must not be parallel to the applied field or the dark state will persist, so a half wave plate was inserted into its path and adjusted to maximize the observed fluorescence.

By tuning the 493 nm laser slightly below the atomic resonance, trapped barium ions were cooled as described in Sec. 2.2.2. A CCD camera (Andor iXon) used for observation of fluorescence. This camera possesses a quantum efficiency of 90% at both 493 and 650 nm, and its CCD chip may be cooled for low-noise operation. It has an electron-multiplying gain mode which can achieve a high sensitivity with a fast frame rate and a conventional gain mode with lower frame rates but less readout noise. In its high gain made, single ions were observed using exposure times of a few ms.

For observation of single ions and coulomb crystals, we used a Mitutoyo M Plan Apo SL objective. This is an infinite conjugate objective with a numerical aperture of 0.24, corresponding to a collection efficiency of $\sim$5.7%. It has a 30 mm working distance and effective focal length of 10 mm. We used it in all of the high magnification (5x or more) systems employed for observation of ion crystals, as it also offered a better ultimate resolution than the achromatic doublets used as objectives at other times.

The average excited state population we observed for ions in coulomb crystals was $\sim$15(3)%. This was measured by counting the number of ions observed in a

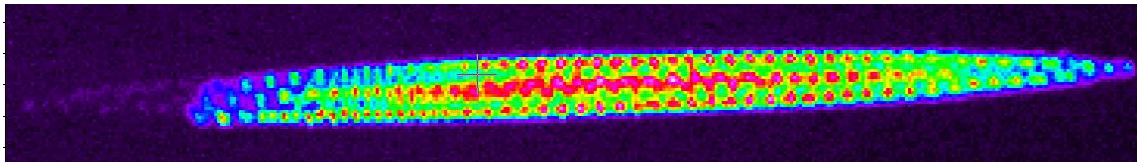

Figure 23: An ion crystal consisting mostly of $^{138}Ba^{+}$, with some other isotopes also dimly visible. Cooling light is incident from the left, and the force shifts the trap center for the $^{138}Ba^{+}$ ions with respect to the others. This results in a *sorting* of the crystal.

coulomb crystal and measuring the number of photons collected per unit time. Then, knowing the collection efficiency of our optical setup we may calculate the excited state population. It is likely that we are not achieving higher values due to coherent population trapping effects (see Sec. 2.2.4) and non-optimal selection of laser powers.

As described in Sec. 2.3, once the ions are in the crystal phase, they will stay in fixed positions with respect to each other. If non-fluorescing ions are present, then dark spots within the crystal will be observed. Even though in the crystal phase there is not enough energy in the system for ions to move past each other, in our system the ions were observed to shuffle their positions. For background pressure of 10^{-10} torr, the mean time for crystal re-organization was about a second. As described by [112], collisions with background atoms occasionally add some energy to the system, and this gives the crystal enough energy for the ions to shuffle around. The effect can be observed directly by turning on the barium oven while observing the crystal. As the flux of atoms being emitted from the over rises, the mean time for ion movement will decrease. A video of a coulomb crystal undergoing repeated reorganizations can be viewed at http://www.avsteele.com/thesis.

If multiple ion species are present within a coulomb crystal, the effects of radiation pressure may be observed (see Sec. 2.2.2 and [112]). In Fig. 23 a mixed coulomb crystal in one of our traps is shown. It consists largely of brightly fluorescing $^{138}Ba^{+}$, with some other ions being sympathetically cooled. Some of those other ions are barium isotopes 134 or 136 and they are fluorescing dimly. The cooling light is incident from

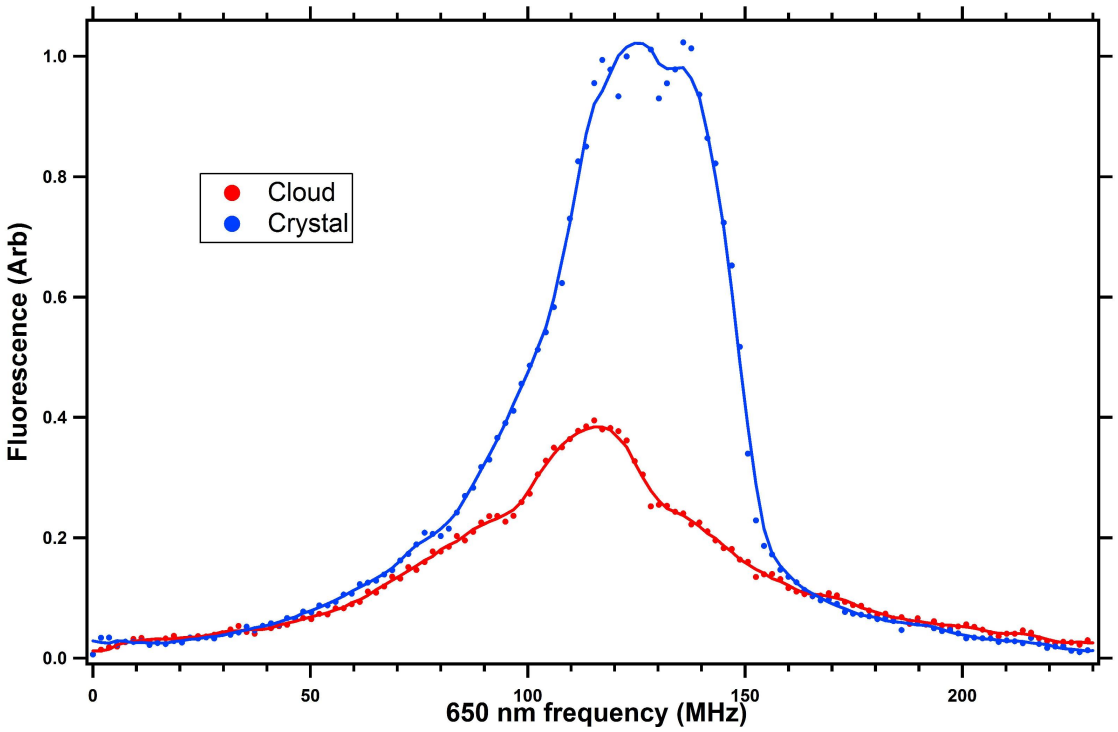

Figure 24: The brightness of a laser cooled cloud and a crystal with equal ion numbers are compared. On frequency sweeps of the 650 nm laser where a crystal forms a brightness increase of ∼2.5 times was observed. All laser and trap settings are equal for these two sweeps. Solid line is a 4 point moving average.

the left and it sorts the crystal, pushing all of the ions being strongly laser cooled to one end of the trap. If a second beam is added going the opposite direction, forces will again be balanced and the ions will be randomly distributed throughout the crystal. This sorting technique may be useful in the future when attempts to observe sympathetic cooling of Th^{3+} are made, since this method localizes all of the ions of a single type to a small volume of the trap.

Fig. 24 shows the difference in brightness for about 20 ions in a cold cloud versus a crystal. The figure shows the ion's fluorescence as the 650 nm laser frequency is swept over the atomic line. Even with identical trap voltage and laser powers, the same frequency sweep will usually result in the atoms remaining a cloud but occasionally the ions will make the phase change to a crystal. If during a given sweep a crystal forms, then the fluorescence increases by a factor of about 2.5 at the

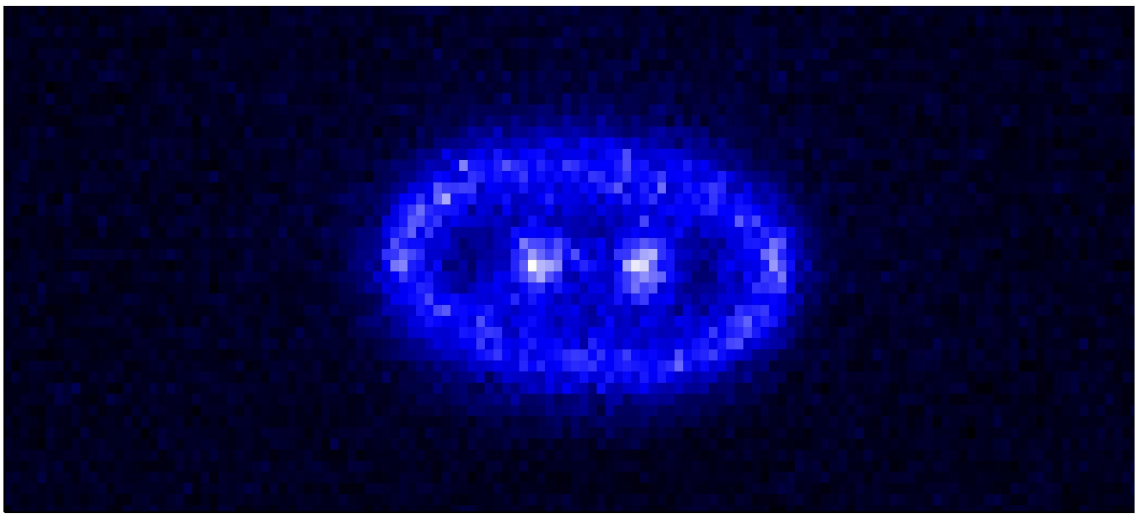

Figure 25: A strange formation of trapped ions which is part coulomb crystal and part cloud.

peak. The crystal forms once in about every twenty frequency sweeps. We believe the crystal formation is dependent on the number of heating collisions (with neutral background atoms) the trapped ions undergo during a given trial.

Typical ion spacing in the crystals shown in the figures above is $\sim$20 μm. In Sec. 2.3 the parameter ε relating the kinetic and coulomb energies was defined as

$$\varepsilon = \frac{E_C}{E_{kin}} = \frac{1}{4\pi\epsilon_0}\frac{e^2}{r k_B T}. \tag{56}$$

The Doppler limit (see Eqn. 30) for the 493 nm transition in Ba^+ is 380 μK. The threshold to cross over to a crystal given by $\varepsilon \geq 168$ implies a temperature of $\sim$5 mK. So crystallization should be readily achievable, as we have found it is. However, emphasizing the results in Sec. 2.2.1, which stated that the heating is driven by the rf drive voltage, ion crystals were only found to form for low values of $q < 0.2$. Crystallization puts a bound on the saturation parameter used. If the laser power is high enough, then the Doppler temperature will be too large for a crystal to form. Loss of crystallization due to high laser power was shown in [89].

Occasionally, very strange arrangements of ion crystals were observed. In Fig. 25 one peculiar arrangement is shown. Here two ions are fixed in lattice positions and

several other ions orbit around them in an oval pattern.

The balance of this Chapter will review some specifics of mirror cleaning and testing, followed by our method of constructing high finesse optical cavities. We will also give a description of the path we intend to take in the next stage of this experiment, which will require the assembly and testing of a miniaturized version of the ion trap described in Sec. 3.1.

3.4 Mirror Testing

As discussed in Sec. 2.6, a pair of high-reflectivity mirrors are critical to achieving strong coupling between the ion and the optical cavity. We purchased a number of high finesse mirrors from Research Electro-Optics. These mirrors had a diameter of 7 mm and radii of curvature of 2.5 cm or 10 cm. The fraction of light transmitted through these mirrors was specified by the manufacturer to be 100 ppm (parts-per-million) at 493 nm and normal incidence.

Each mirror required testing to see whether it met this specification. Several cavities were constructed perform these tests. First, a short (0.1 mm) cavity was made from one set of the mirrors. The mirrors where held by two aluminum mounts which registered to a cylindrical piezo controlling the mirror spacing. The voltage required to adjust the length of the cavity by $\lambda/2 \approx 246$ nm, one free spectral range, was found. We also measured was the voltage required to change the cavity's length by one linewidth. The cavity's linewidth can then be found by the equation

$$\frac{\kappa(Volts)}{FSR(Volts)} = \frac{\kappa(Hz)}{FSR(Hz)}. \tag{57}$$

The FSR of the cavity is given by Eqn. 44. From Eqn. 57 the linewidth of the cavity, κ, and therefore the mirror losses (see Eqn. 46) may be calculated. The limitation of this technique is that a cavity with a linewidth much larger than the laser must be used. If the cavity's width is not much larger than the laser's, then the measured cavity width will be convolved with the laser linewidth. For high finesse mirrors, this

requires a very short cavity whose length must be known precisely. It also requires confidence in the linearity of the piezo response when it is moved one FSR.

The cavity *ringdown* technique is another way of measuring mirror reflectivity. The linewidth of the cavity can be measured by quickly shuttering off the light on the input of a cavity on resonance, then monitoring the light intensity decay on the cavity's output with a fast photodiode. The cavity linewidth κ will be lifetime of the light decay from the cavity. This method requires a fast light shutter, such as an AOM. It also requires a photodiode with a bandwidth greater than κ to monitor the light decay. Fig. 26 shows data from a particular ringdown measurement on a cavity of length $\sim$19 mm. Longer cavities than those used in the direct κ measurement may be used with the ringdown method, making it less prone to errors arising from the cavity construction.

Employing these two linewidth measurements we found that all of the 10 cm mirrors tested had losses between 200 and 280 ppm, far more than the specification. The 2.5 cm mirrors tested yielded losses of 125-130 ppm. We selected a sample of the 2.5 cm mirrors for cavity construction.

3.5 Cavity Construction

Cavity construction was done in several stages. First, we must make a modification to the mirror's substrate in order to remove superfluous areas of the high reflectivity surface. We require a cavity with a length of 1 mm. The mirror's radius of curvature is 25 mm, and its diameter is 7 mm. The curvature and diameter imply that if we have a 1 mm mirror spacing then at the edges of the reflectors the mirrors will be separated by only $\sim$0.5 mm. By cutting away the excess reflector surface, the minimum distance between the mirror will be much closer to the 1 mm cavity length, giving us more room for the ion trap between the mirrors.

The cavity lengths and radius of curvature set the cavity waist to $w_0 = 23$ μm and

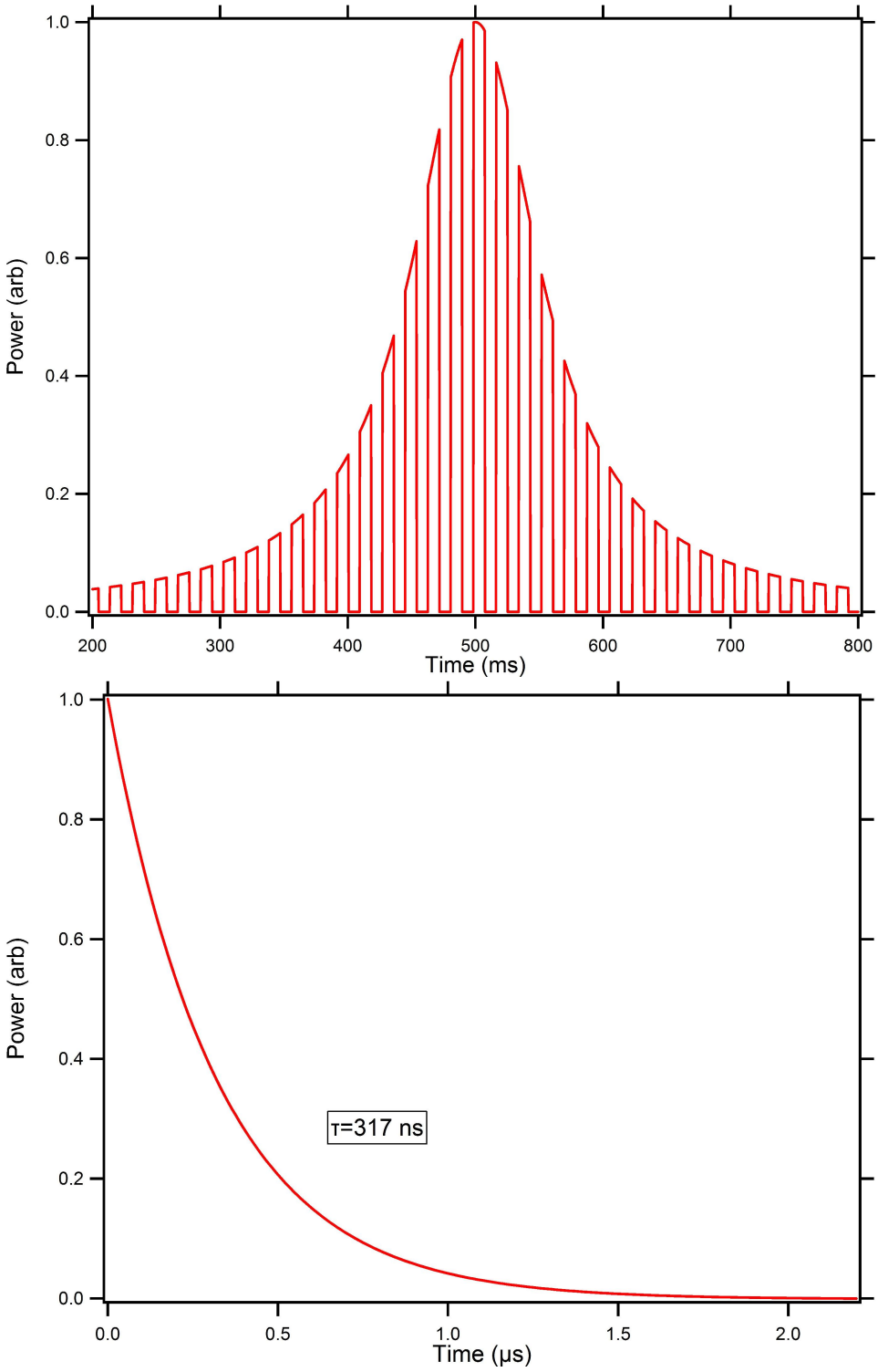

Figure 26: Ringdown performed on a pair of mirrors making a $L = 19$ mm cavity. (Upper) As the cavity's length is swept over a resonance, the lineshape is modulated by the rapid chopping of the cavity light by an AOM. (Lower) When the cavity input light is shuttered off, the light on the cavity's output decays exponentially with a measured lifetime $\tau = 317$ ns, yielding per-mirror losses (by Eqn. 46) of 200 ppm.

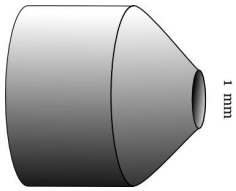

Figure 27: Drawing of a coned cavity Mirror.

the waist at the cavity mirrors to $w_1 = 24$ μm (see Eqns.47 and 48). The radius of the reflecting surface of the mirror only needs to be a few times larger than the waist w_1 for losses due to inadequate surface area to become negligible. For example, if the mirror's radius is $3w_1$ then losses will be $\sim$10 ppm. We left 1 mm of reflector on our mirrors ($\sim 40w_1$), so the losses should be negligible as long as the cavity mode is near the center of the mirror. We also reduced the back end diameter of the mirrors to 3 mm. A diagram of the mirror shape can be seen in Fig. 27. These reduced mirrors are very similar to ones described in the theses of Jacob Sauer [113] and Kevin Fortier [114].

Once the mirror substrate has been reduced, the high reflectivity surface must be cleaned. While every effort is made by the manufacturer to keep the mirror surfaces clean, small particles are inevitably on the mirror surface upon receipt. The typical size of these particles is $<$10 μm, they are easily visible using the dark-field mode of a high magnification microscope. In order to maximize the cavity finesse they must be removed.

This was done by hand, using lintless lens tissue, a pair of tweezers, and a small amount of methanol. The mirrors where repeatedly swiped from the center of the reflector outward to the edge. This was done with great care. If the tissue is brought down too close to the edge of the reflector, then glass particles from the rough cone shaped surface can be dragged across the mirror surface. At best, this will simply mean restarting the cleaning process At worst, the mirror can be ruined. Fortunately, surface damage is easily visible under the microscope.

Once a pair of mirrors were cleaned, the cavity was assembled. Each mirror is attached to a 3-axis micrometer stage. Under a microscope, the mirror spacing was set to 1 mm. One of the micrometer stages also has a two axis gimbal mount so that the faces of the mirrors can be made parallel. Once the mirror spacing and alignment is set, light is coupled into the cavity. By observing the small amount of light scatter from a mirror's reflective surface when the cavity was resonant with the laser we verified that the cavity's mode was near the center of both mirrors.

A small quantity of Torr-Seal adhesive was applied to the side of each mirror and a flat piezo crystal was brought down on top of the mirrors. Torr-seal limits the temperatures to which the chamber may be heated to $\lesssim 100°\mathrm{C}$, but it is otherwise an ideal adhesive for ultra-high vacuum applications. After the adhesive dries, the cavity's finesse was tested by the ring-down technique, yielding $\mathcal{F} = 1.9 \pm 0.2 \cdot 10^4$, implying a per-mirror loss of 167 ppm. The increased losses measured here when compared with the ringdown measurement discussed in Sec. 3.4 are most likely due to dust attaching to the mirror surface during construction. The finesse of this cavity is lower than we desired, so a new cavity may be constructed before it is integrated with the miniature ion trap. This cavity would presently operate between the strong and weak coupling regimes. From Eqns. 54 and 55 we have:

$$\frac{g^2}{\kappa\Gamma} = 0.8 \tag{58}$$

$$\frac{g}{\kappa} = 1.74 \tag{59}$$

The completed cavity in its counting black can be seen in Fig. 28

3.6 Cavity+Ion Trap Integration

In the next stage of this experiment a miniature ion trap (which remains to be built) and the 1 mm cavity described above will be integrated. The integrated design we will use consists of a vertically mounted cavity as shown in Fig. 28 and a miniature linear ion trap mounted on an arm which may be swung into, or out of, the cavity.

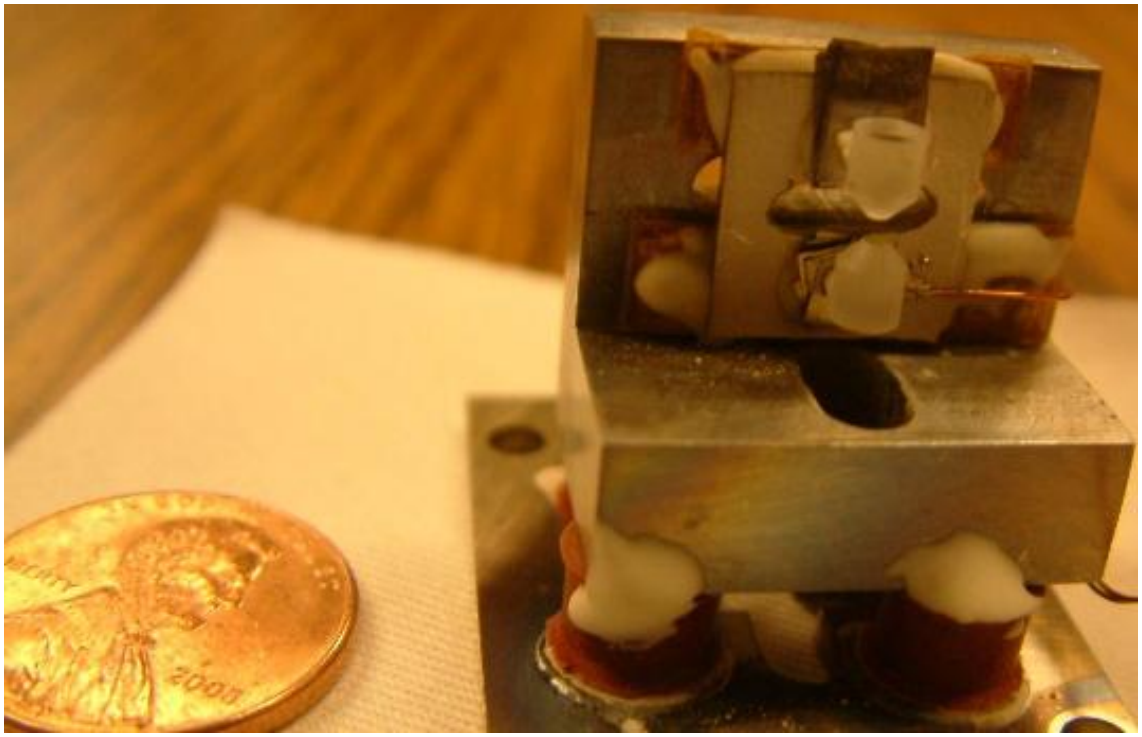

Figure 28: High-finesse cavity and mounting block.

The ability to move the trap is important for two reasons. First, it is possible that the presence of large dielectrics near the trap electrodes may have an impact on the trapping potential. By allowing the trap to remain mobile it may initially be tested away from the influence of the cavity. Mobility may also be important so we can be sure that the trap is in a position where its electrodes will not clip the cavity mode.

CHAPTER IV

THORIUM ION TRAPPING

This chapter reviews the results of our thorium ion trapping experiment. Th^{3+} ions were produced by laser ablation from a metal target and subsequently trapped. The ions were cooled and made to fluoresce by illuminating them with lasers at 984 nm, 690 nm and 1087 nm. The fluorescence was observed with a CCD camera. The trapping apparatus was housed in a vacuum chamber pumped down to a pressure below 10^{-9} torr of all gases except helium. Singly ionized barium ions were used as a spatial aid for the proper placement of the thorium fluorescence lasers and for tests of the camera's noise properties and collection efficiency. The details of each piece of the experimental apparatus will be reviewed followed by some notes on the experimental techniques we employed. This Chapter concludes with a presentation of the acquired Th^{3+} fluorescence data.

4.1 Chambers

Two different ion trap arrangements were used in this experiment. However, the components of each chamber were prepared in much the same way. Each element that went into the chamber was ultrasonically cleaned in either acetone or methanol. Each chamber had an ion pump and a titanium sublimation pump. After assembly the chambers were attached to a turbo pump and heated to $\geq 300°C$ for a period of a few days while the partial pressure of water vapor in the chamber was monitored by a residual gas analyzer. When the partial pressure of water had dropped below that of nitrogen the chamber was cooled and sealed off. Thereafter it was pumped continuously by an ion pump. The exception being the trap of Sec. 4.1.2 which was pumped continuously by a turbo pump because of the high pressures of helium (up

to 10^{-5} torr) which were often introduced into the chamber.

4.1.1 Large Linear Trap

A new chamber was constructed at the start of the thorium experiment. We desired a trap with a large trap volume, to make loading of Th^{3+} ions as favorable as possible. The design is similar to the trap in [115] dimensionally, and is made for observation of large ion crystals. The trap's configuration was similar to the trap of Sec. 3.1, with 4 polished stainless steel cylinders ($d = 4$ mm) forming the electrodes and stainless steel tubes slipped over them to make the endcaps. The distance between the endcaps was $\sim$20 mm. The electrodes were again held in an alumina mount, but due to the large size of the electrodes in this trap no prefabricated spacer was available, so we had to drill the alumina ourselves using a diamond coated drill bit. The trap radius was 2.0 ± 0.2 mm, the high uncertainty being mainly due to the imprecision of the alumina cutting, which was done by hand with a drill press. The overall trapping volume is about a factor of 10 larger than in the trap of Sec. 3.1. Additionally, this trap should follow the theory of the linear Paul-style trap more precisely than the Sec. 3.1 trap because the ratio of rod diameter to r_0 follows the shape of the ideal hyperbolic electrodes more closely; it is nearly the optimal ratio of 1.15 specified by [62].

The area between the trap electrodes was large enough that a 1 mm on-axis hole could be drilled in the alumina mount. This enabled us to add a cooling beam which propagated along the trap's axis. This beam allows radiation pressure sorting of the trap contents to be done (see Sec. 3.3). Additionally, the on-axis cooling beams scattered far less laser light from the trap electrodes when compared with beams passing perpendicular to the trap axis. Low levels of light scatter yielded a high signal to noise ratio (>200 for a single Ba^+ ion in a 0.1 s exposure) when observing fluorescence from trapped ions. Counter-propagating barium and thorium light along

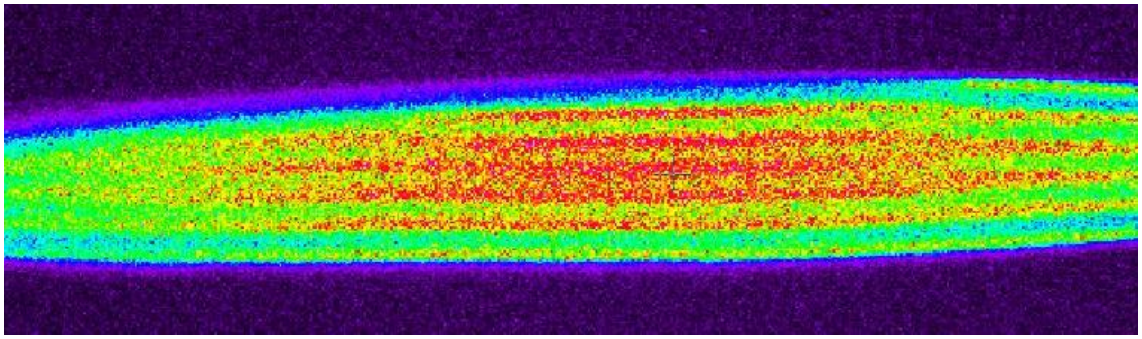

Figure 29: A huge ion crystal loaded into the large linear trap. The crystal structure is visible as alternating light and dark lines of ions.

the trap's axis could also be used to separate the barium and thorium ions in the trap using the radiation pressure force (see Sec. 2.2.3). This trap was placed in a 'spherical octagon' chamber purchased from Kimball physics (MCF450-SO20008C) which has a central 4.5" flange and eight 1.33" flanges around its outer edge. The chamber also affords a line of sight so that cooling beams could be added at 45° to the trap axis either along the horizontal or the vertical.

The barium oven in this chamber was placed ∼1 cm below the trap and an electron gun ∼1 cm above it. A tantalum metal crucible containing thorium nitrate was placed below the trap at an angle of 45° to the barium oven.

The trap is able to load and cool very large ion crystals. The crystals shown in Fig. 23 and Fig. 35 were created in this chamber. An even larger crystal where the individual sites are no longer resolvable, but the overall ordered structure remains visible can be seen in Fig. 29. Species identification of loaded ions in this chamber was difficult. Fluorescence was only observable from the barium ions; in order to identify other species, we had to observe a change in barium fluorescence after the ejection of the other ions. This process is described in greater detail in Sec. 4.7.1

4.1.2 Ion Filter and Trap

We built another ion trap for this experiment by performing a modification of a commercial residual gas analyzer(RGA), the Stanford Research Systems SRS100 (Fig. 30).

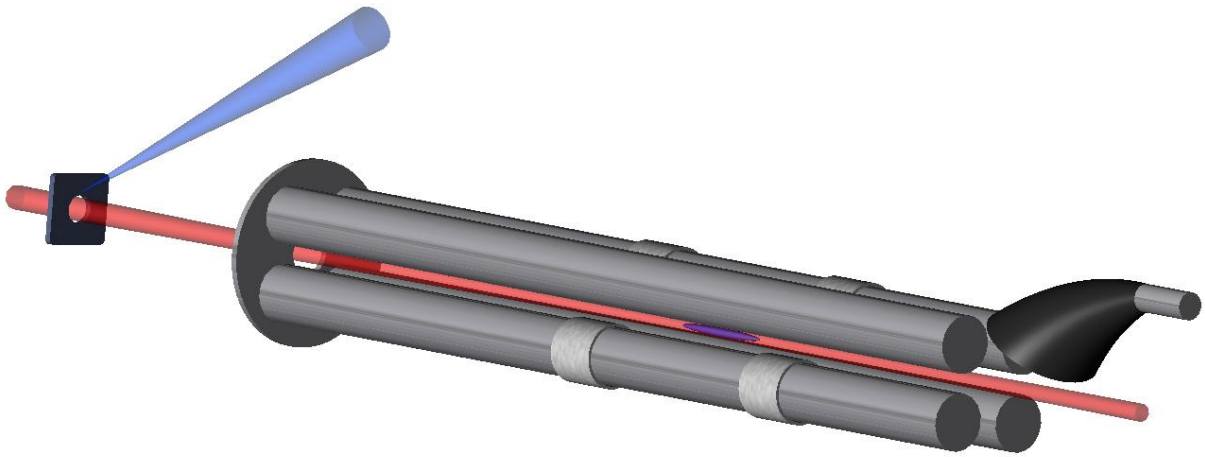

Figure 30: Diagram of modified RGA ion trap. The blue focused beam represents the third harmonic of a pulsed YAG laser, used for ablation. The red beam represents laser cooling light shined along the trap's axis. A diverging plume of ions pass from the ablation metal target, and are turned by the focus plate into the trapping region between the four rods. Two of the rods have stainless steel electrodes wrapped around them. By applying a positive voltage to these stainless steel sheathes a trapping region can be created. The potentials V_{rf} and U_{dc} are usually applied only to the two other rods without sheathes. At the far end of the trap is a CEM biased at -2800 V. The ions emerging from the quadruple rods are turned into the CEM by this high negative voltage.

This unit was originally used for detecting leaks in our vacuums systems and monitoring chamber bakeouts. The mass filter unit consists of four 6.3 mm diameter rods. At one end of the rods is a thoriated iridium filament ionizer which typically produces 1 mA of 70 eV electrons. Ions created by these electrons are focused into the region between the rods by a plate biased at -70 to -125 V. This plate serves to focus a divergent beam of ions into the region between the rods. At the other end of the rods is a faraday cup, for reading out ion currents between 1 mA and 0.1 nA, and channel electron multiplier (CEM), designed for reading an ion currents of between 1 μA and 10^{-17} A. The CEM is also capable of outputing current pulses generated by the arrival of single ions.

We placed several metal targets at the end of the RGA approximately 7.5 cm from the focus plate. The metal targets included thorium, barium, tantalum and stainless steel. By focusing the third harmonic of a pulsed YAG laser onto the surfaces of these metals, metal ions were created in a process called *ablation*. The ablation technique is described in greater detail in Sec. 4.2. A hole co-linear with the trap's axis is punched through the metal targets so that cooling laser beams may pass through into the trap.

The RGA has several features which make it attractive as an ion trap. First, the alignment and positioning of the rods is very precise. They are fixed in place by a precisely ground alumina spacer. Used as a mass filter, the RGA is able to achieve a precision of $<$1 amu, allowing the separation of different isotopes of a given atom. The circle inscribed by the rods has a radius of 2.77 mm with a tolerance of better than 300 μm. The high level of precision minimizes the possibility non-quadrupole potentials affecting the ions, as described in [63]. The rods are 115 mm long, giving enough room to make an ion trap consisting of multiple segmented trapping regions.

The control electronics and radio-frequency source that come packaged with the RGA will not function if the trap assembly is not housed in a 2.75" nipple, due to the difference in trap capacitance. To control the trap voltage ourselves we purchased a

high voltage rf source from Ardara Technology. It has two outputs 180° out of phase, each capable of producing a wave of 1200 V amplitude at 2.2 MHz, which is a high enough rf voltage to reach the highly mass selective regime ($q \approx 0.7$) for $^{232}Th^{+}$. To apply a large enough value of U_{dc} to reach the selective regime ($a \approx 0.21$) we used a high voltage piezo driver capable of swinging its full 150 V range in less than 1 ms. This speed is important as it allows us to quickly apply mass selection pulses after loading the trap.

In order to create a region where ions could be trapped, we added several new electrodes to the trap. Two pairs of thin rings of 0.001" thick stainless steel shim ∼10 mm wide were wrapped around the trap electrodes. The pairs of rings were placed on diagonally opposite rods and separated by ∼25 mm. The shim was insulated from the rods by polyimide tubing. By placing a positive voltage on these pieces of shim, we created an axial trapping potential for positive ions. Though only two endcap electrodes would have sufficed, having four allows any micromotion-inducing fields at the trap center to be zeroed (see Sec. [59]). Since this zeroing was not needed to accomplish our immediate goals, the endcaps at each end of the trap were welded to each other.

One of the features of this trap which motivated its construction was its ability to identify the number of ions in the trap electronically. By dropping the voltage on the set of endcaps closest to the CEM to 0, trapped ions may be ejected from the trapping region and into the CEM. Current pulses on the CEM's output arising from the arrival of each ion can then be counted with an amplifier/discriminator. By comparing the fluorescence measured from a cloud of barium ions to the number of pulses observed on the CEM after dumping those ions, we estimated the efficiency of the counting to be about 30% with a -2800 V bias on the CEM. However, we cannot state with confidence whether or not the temperature of the ions has an effect on the dumping efficiency.

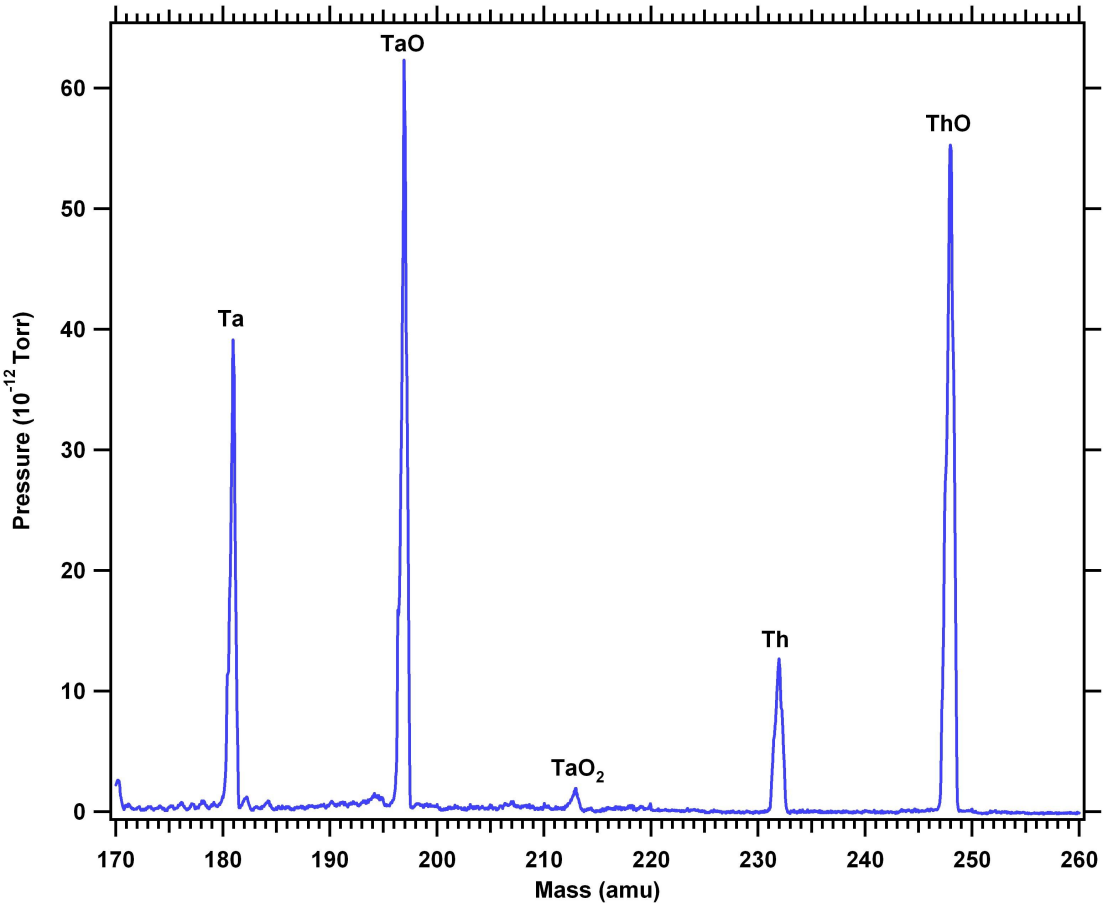

Figure 31: The products of electron impact ionization of Thorium Nitrate. A nitrate source was heated to high temperatures and aimed at the RGA's ionization region. The > 1 mA of 70 eV electrons produced the shown singly ionized products. The RGA's software converted an ion current measured at its faraday cup into an estimated pressure based on a calibration to nitrogen. No products at lower mass/charge ratios than $\sim$180 were detected.

4.2 Thorium Ion Generation & Laser Ablation

Thorium is not as readily available as barium. The source of thorium which may be acquired most easily is thorium nitrate, $(Th(NO_3)_4)$, is a white powder. By adding water to the nitrate we created a slurry which could be applied to a thin piece of tantalum foil to which it adhered. The foil was attached to leads so that the tantalum could be resistivity heated. We attempted to create Th^{3+} ions by heating this source near the RGA's ionizing electron beam.

Fig. 31 shows our observations. We saw clear evidence of singly ionized thorium

and thorium oxide, which must either have detached from the nitrate as it left the source or been fragmentation products of electron impact in the RGA's ionizer. Strong signals of tantalum, tantalum oxide and tantalum dioxide were also observed. The source had to be heated to very near the melting point of the tantalum foil (3000 K) to observe any thorium signal at all, so it is not surprising that tantalum was observed in such large quantities. No detectable levels of Th^{2+} or Th^{3+} were observed.

There are several reasons why this might be. The total energy needed to ionize Th→Th^{3+} is 37.7 eV and the electron energy of the RGA is ∼70 eV. But, as can be seen in [116], the electron impact cross sections for double and triple ionization, in that case of magnesium, are peaked at electron energy values much larger than the ionization energy of the atom. The energy required to ionize Mg → Mg^{2+} and Mg → Mg^{3+} are 22 eV and 103.2 eV, but the electron impact cross sections are peaked at energies of 200 eV and 400 eV respectively. If this were the only problem it might still be feasible to ionize thorium via electron impact by simply increasing the electron energy. However, as [116] also makes evident, the cross sections for electron impact drop by an order of magnitude with each successively higher charge state. The peak electron impact ionization cross-section of Mg^{+} is $6 \cdot 10^{-16}$ cm^2, Mg^{2+}'s peak is $2 \cdot 10^{-17}$ cm^2 and Mg^{3+}'s peak is 10^{-18} cm^2. This suggests it would be difficult to produce more than a small number of Th^{3+} by electron impact ionization.

The prospects for creation of a large number of Th3+ ions might be better for resistive heating of a pure thorium metal source since it could be brought to a higher temperature than a tantalum vessel, but this presents difficulties as well. Thorium metal is not easily acquired. We first procured a sample of thorium wire from the Goodfellow Wire Company. Upon receipt we found the wire to be completely oxidized, nearly to its core. This sample had reportedly been sitting in air for about 30 years. We tried to heat the residual thorium oxide as well. The melting point of thorium oxide is so high however (3651 K) [117], that no detectable levels of thorium coming

off the sample were detected before the destruction of the resistively heated container holding the ThO. Containers used in these attempts included both a resistively heated piece of tantalum foil and a ceramic crucible heated by tungsten wire.

Photoionization was a technique we employed with great success in the creation of Ba^+, but the large energy required to obtain Th^{3+} from neutral thorium would necessitate either a pulse laser with extremely high intensity or a potentially complex multi-step ionization process.

The ionization technique with which we had the greatest success was laser ablation. We were generously lent a sample of thorium metal by Dr. Heavens of Emory University and later purchased a second sample of thorium metal from Goodfellow Wire. We also borrowed a pulsed Nd:YAG laser (Thompson-CSF 5000 Series) from Dr. deHeer of Georgia Tech. By focusing a pulse from the third harmonic output of this laser at 355 nm on to a thorium metal or thorium nitrate target we produced a plasma plume consisting of $\lesssim 10^{15}$ particles of neutral thorium (see [118]), electrons and highly charged ions (ions are $\sim$50% of the total atoms [118]). Some fraction of the ions produced will be Th^{3+}. The mechanism by which ions are created in the ablation plume has never been definitively explained, so no predictions about what fraction of the particles would be Th^{3+} were available. The typical pulse energy used was a few mJ.

Ablated ions have a very high energy and velocity when compared with ions created via electron impact ionization in the RGA's ionizer. We measured the speed of the ions in the ablation pulse by measuring plume arrival times for electrodes at different distances from the ablation target. We obtained a result of 12 km/s for ions ablated from a piece of thorium metal. This agrees with the result in [118] of 10-30 km/s. For Th^+, this velocity is $\sim$4.5 times greater than that of ions created by the RGA's ionizer unit, which have an energy of 8 eV.

Our first target for the ablation laser was a sample of thorium nitrate. The nitrate

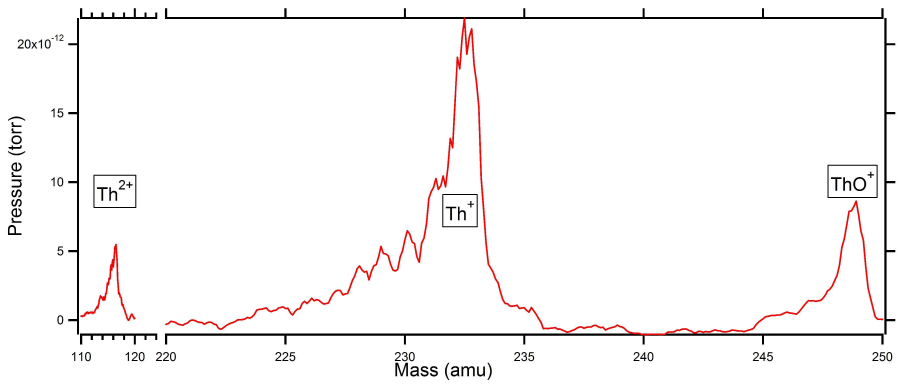

Figure 32: The products of thorium nitrate ablation. The ions produced here were created directly by the ablation process, RGA's ionization unit was switched off for these studies. Both Th^{+} and Th^{2+} were detected, but Th^{3+} was not. These peaks are substantially broader than those of Fig. 31. These peaks are an average of several sweeps over these mass/charge ratios as the ablation laser was fired continuously. On any given sweep these peaks may or may not appear. The peak widening observed is likely due to the diminished mass selectivity of the RGA for ablation due to their high velocity when compared with ions created by its ionizer.

was again mixed with water to make a slurry which was then applied to a piece of stainless steel. The sample was pointed towards the RGA axis and the ablation laser was fired at it. The ablation products observed can be seen in Fig. 32. We were able to create both Th^{+} and Th^{2+} ions. No Th^{3+} was observed from the nitrate, but it is possibly being created in smaller quantities than the RGA may detect in this mode of operation.

Ablation of pure thorium metal was investigated next. The metal target was placed ∼5 cm from the end of the RGA and the ablation laser was continuously fired at its surface. The ionizing filament was turned off for these tests. The mass/charge regions about 232 amu, 117 amu and 77 amu were examined for peaks corresponding to Th^{+}, Th^{2+} and Th^{3+} respectively. These mass scans can be seen in Fig. 33.

The relative numbers of each ionization state shown in Fig. 33 might not be accurate. This measurement (along with the nitrate ablation) is quite different from the type the RGA was designed to handle. When measuring residual gases using the RGA's ionizer filament, ion currents at the faraday cup were measured to be,

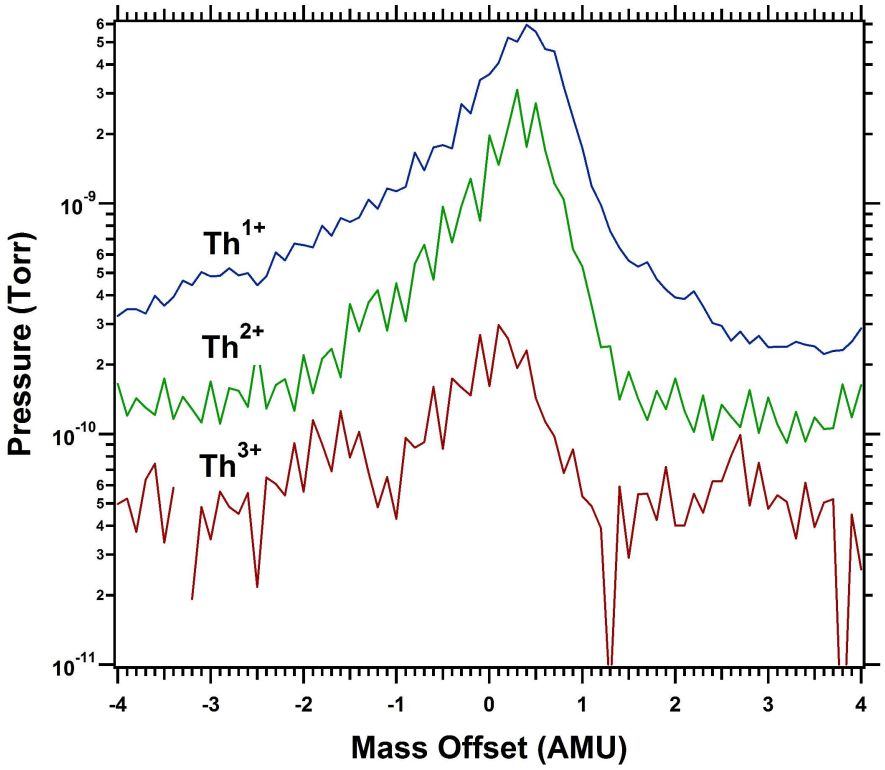

Figure 33: The products created from ablation of Thorium metal. Three peaks identified as Th^{+} Th^{2+} Th^{3+} were found and are plotted with respect to their expected mass/charge numbers. The relative heights are not likely to be representative of the true number of ions created by the ablation laser.

at most, ~ 10 μA. This would imply $\sim 10^{14}$ ions/s arriving with some Poissonian distribution. Conversely, an ablation plume contains $\lesssim 10^{15}$ ions [118]. By collecting the ablation products on a nearby electrode in a different chamber we observed that the overwhelming majority of charges are clustered within a 2 μs time span. This would imply a peak ion rate of 10^{20} ions/s. The laser fires at a rate of 10 Hz, so the duty cycle is $\sim 10^{-5}$. This means the only way the RGA's electronic readout would be correct is if the electrometer was properly averaging the huge peak current over several pulses. In order to collect the above data in Figs. 32 and 33 we had to average about 30 sweeps over the relevant mass region. On any given mass scan a peak may or may not appear.

Ablation yields more ions as the laser power is increased. However, if the power is sufficiently high, the ablation products will short out the rf electrodes providing the trapping voltage. In some cases this can be advantageous. If the rf and endcap voltages are fixed when the ablation laser is fired, then since the trapping field is a conservative, no ions will be loaded. When the trap is shorted out, the confining voltages drop to 0. When the voltage recovers, any ions still in the trapping region can be confined. We relied on this technique for some of the early attempts to load ions produced by ablation. In the trap of Sec. 4.1.1, the thorium metal target was placed in the chamber with its face perpendicular to the trap, at a distance of about 2 cm. In this configuration, the ablation plume shorts out the trap for $\sim$20 μs. After the voltage returns to its original value we would observe trapped ions. If the barium oven was on during the ablation, the collisions between ablation products and neutral barium would cause Ba^+ to load into the trap.

Loading efficiency can be increased dramatically by utilizing techniques which do not require shorting of the trap. These techniques will be discussed in Sec. 4.7.2.

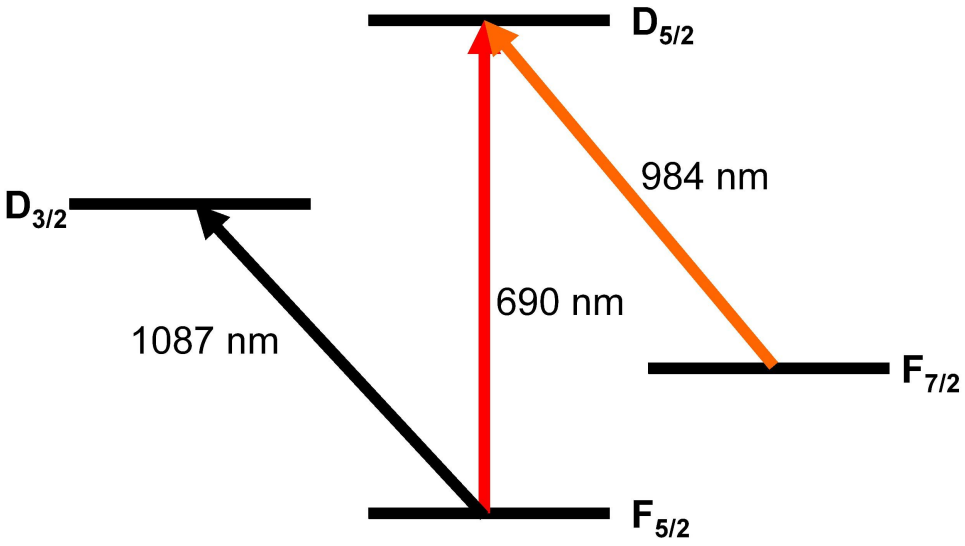

Figure 34: Thorium energy levels utilized in this experiment. A laser at 1087 nm drives a cycling transition, while lasers at 690 nm and 984 nm together drive a Λ-system. The calculated lifetime of the $D_{3/2}$ was calculated to be 1090 ns, while that of the $D_{5/2}$ state was calculated to be 676 ns [119].

4.3 Thorium Lasers

The four lowest energy levels of Th^{3+} can be seen in Fig. 34. Two laser schemes are available for observation of fluorescence. The simpler of the two is the cycling transition at 1087 nm which links the states $2^5F_{5/2} \rightarrow 6^2D_{3/2}$. The other scheme is the Λ-system consisting of the states $5^2F_{5/2}$, $6^2D_{5/2}$ and $5^2F_{5/2}$, which requires lasers at 984 nm and 690 nm. Lifetimes of the $6^2D_{3/2}$ and $6^2D_{5/2}$ states were theoretically calculated by [119] to be 1090 ns and 676 ns respectively, with the $6^2D_{5/2}$ state having a calculated $\sim 1 : 10.5$ branching ratio in favor of the transition at 984 nm; implying linewidths of 214 kHz for the 984 nm line, 23 kHz for the 690 nm line and 146 kHz for the 1087 nm line.

The most accurately measured wavelengths for these transitions are cataloged by [45]. The wavelengths listed there had a number of significant figures to imply a precision of order 3 MHz for the 984 nm and 1087 nm lines and 300 MHz for the 690 nm line. Unfortunately the uncertainties actually stated in the original papers

that [45] references were not available because they had been classified by Los Alamos. The narrow linewidths of these transitions and the line-center uncertainty implied that we may be required to search over a range of wavelengths before we found the correct ones for observation of fluorescence. However, given that we did not have the uncertainties, it would be difficult to confidently state that our attempt at observation did not fail simply because we had not searched enough laser frequencies.

Because the transition at 1087 nm only requires one laser, and its upper state lifetime is nearly as short as the upper level in the Λ-system, it seems the natural choice for observation. Unfortunately no low noise detectors could be found with a high quantum efficiency (QE) at that wavelength. The silicon based CCD's or APDs we use most frequently in the lab were measured to have a quantum efficiency of 0.12% at 1087 nm.

The Λ-system has drawbacks as well. First, we would be required to scan through two sets of laser frequencies to find the correct wavelengths near 984 nm and 690 nm. Given the unknown error bars on the measurements in [45] we were without a clear idea of how much frequency space we would be required to cover. In this scheme we would be observing light at 984 nm and 690 nm, with the 984 nm light being more than 90% of the total. The QE at 984 nm for our camera was only 18%. Additionally, as in barium, a magnetic field must be applied for continuous observation because the lower level in the 984 transition, $F_{7/2}$ has more states than the upper level $D_{5/2}$. Coherent population trapping could be a problem as well when working with the Λ-system.

Diodes at 984, 690 and 1087 nm were purchased from Power Technology and installed in Littrow style diode laser setups. A distributed feedback laser (DFB) was also purchased from Toptica at 1087 nm. The 984 and 690 nm lasers were coupled into the same fiber using a dichroic beamsplitter to ensure their overlap. We could achieve almost 1.5 mW of 984 nm power and 4 mW of 690 power through the fiber.

The 1087 nm laser originally put out 30 mW, but the diode's output power dropped before we were ready to use it in the experiment and thereafter only about 0.3 mW of light could be coupled into a fiber.

4.4 Buffer Gas cooling

Buffer gas cooling was used extensively in this experiment. The ions loaded by an ablation pulse may initially have a temperature which is a significant fraction of the trap depth ($\sim 10^5$ K). This temperature is high enough that only a very amount fluorescence will be emitted due to the ion's large Doppler width. The buffer gas is a simple way of cooling the ions to a temperature where they can be more efficiently laser cooled (as in barium) or observed via their fluorescence without further cooling (as with thorium).

The laser frequencies for optimal cooling near the coulomb crystallization phase change will be very different from those which may quickly cool hot laser-ablation loaded ions (see Sec. 2.2.2). With the 493 nm and 650 nm lasers fixed to frequencies optimal for ion crystal cooling we measured the length of time required for Ba^+ ions to come to their equilibrium temperature with and without a helium buffer gas pressure of 10^{-6} torr. Determination of ion cloud temperature equilibrium was determined by monitoring ion fluorescence on a CCD camera. If no buffer gas is used, it takes about 30 to 40 seconds for ablatively loaded ions to come to equilibrium. Only in the last 5-10 seconds is any fluorescence observed at all. This time can be reduced to a few seconds if a larger fraction of the trap is illuminated with cooling laser light than would be necessary for observation of the cloud at its (colder) equilibrium temperature. If the buffer gas is present, then the cloud will come to equilibrium within 12 ms (the lower frame rate limit of the camera we were using) of the laser light being turned on.

As discussed in Sec. 2.2.1, collisions with background atoms and a fluctuating

background electric field (due, in part, to the presence of other ions) are two mechanisms which will contribute to rf heating. The final temperature of an ion cloud will depend both on the rate of rf heating and the rate of buffer gas cooling.

The buffer gas was introduced to the chamber through a leak valve (Granville-Phillips Co. Series 203). This unit had a hand operated crank for opening and closing, and a dial to indicate the state of the value. It was bakeable to 450°C when the valve driver was removed. The ability to bake this valve was an important feature. When it was used initially, without baking, the gas flow at a given value of the dial was not consistent and a strong hysteresis effect was apparent. We found that this was the result of having a water seal form between the two components which make the valve's vacuum seal. After baking the unit, the water seal was broken and the unit admitted a continuous flow of vapor, allowing us to operate at pressures anywhere between 10^{-10} torr and 10^{-5} torr.

Fully purging the line behind the valve before introducing helium is critical as well. In the first installation of the valve this was not done. As a result, after opening the leak valve we observed a greatly reduced Ba^+ trap lifetime. Before opening the value a trap lifetime of >8 hours was observed, after opening the value this was reduced to a few seconds.

We set to investigating whether the loss of barium ions was due to charge-exchange collisions or a chemical reaction. By observing the fluorescence from a cold barium crystal we found Ba^+ ions were being replaced by another ion which remained in the trap. This work was done in the Sec. 4.1.1 chamber so electronic readout of the trap contents was not an option. By issuing short pulses of the a parameter and identifying the exodus of the unknown ion by observing the increase in barium crystal purity, we identified the interloper as BaO^+. This identification methodology is described in greater detail in Sec. 4.7.1. Fig. 35 shows the change in crystal purity following an a pulse which ejects BaO^+ from the trap.

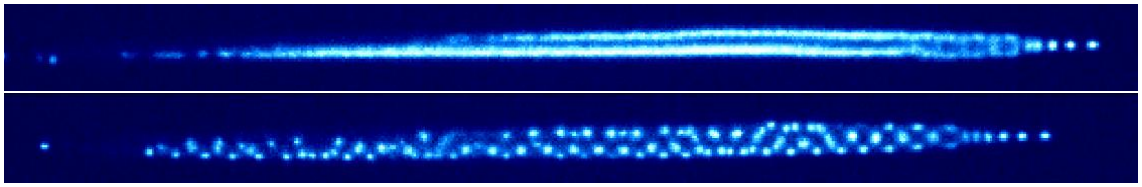

Figure 35: A mixed crystal of BaO^+ and Ba^+ ions (upper) from which the BaO^+ ions were ejected to create a purer Ba^+ crystal(lower). The remaining dark spots in the lower crystal are barium isotopes other than the brightly fluorescing $^{138}Ba^+$.

Given the strong reaction of barium metal in air with oxygen, the reaction

$$Ba^+ + O_2 \rightarrow BaO^+ + O \tag{60}$$

was suspected to be the mechanism responsible for the ion loss. However, in [120] a variety of molecular ion crystals were examined and sympathetically cooled with barium, and they note that the reaction

$$Ba^+ + CO_2 \rightarrow BaO^+ + CO \tag{61}$$

is exothermic by several eV, whereas the reaction of barium with oxygen is endothermic and will not occur even with the optically excited Ba^+. In order to avoid contamination of the leak valve helium line and vacuum chamber in the future, the helium line was pumped down to rough vacuum and then backfilled with >1 atmosphere of helium.

We made a measurement of barium cloud temperature as a function of partial pressure of helium introduced to the vacuum chamber. Fig. 36 shows the temperatures we observed. All of the measurements were made with the same cloud of barium ions, and in rapid succession. The powers on the 493 and 650 nm were turned down to 16 μW and 17 μW respectively, giving saturation parameters $s \leq 0.1$ for both the 493 nm and 650 nm transitions. This was done to ensure no laser cooling was being performed. The buffer gas was initially set to 10^{-8} torr, the 493 nm frequency was held fixed, and the 650 nm laser's frequency was swept over the fluorescence peak. This was repeated, increasing the buffer gas pressure by a factor of 10 each time up

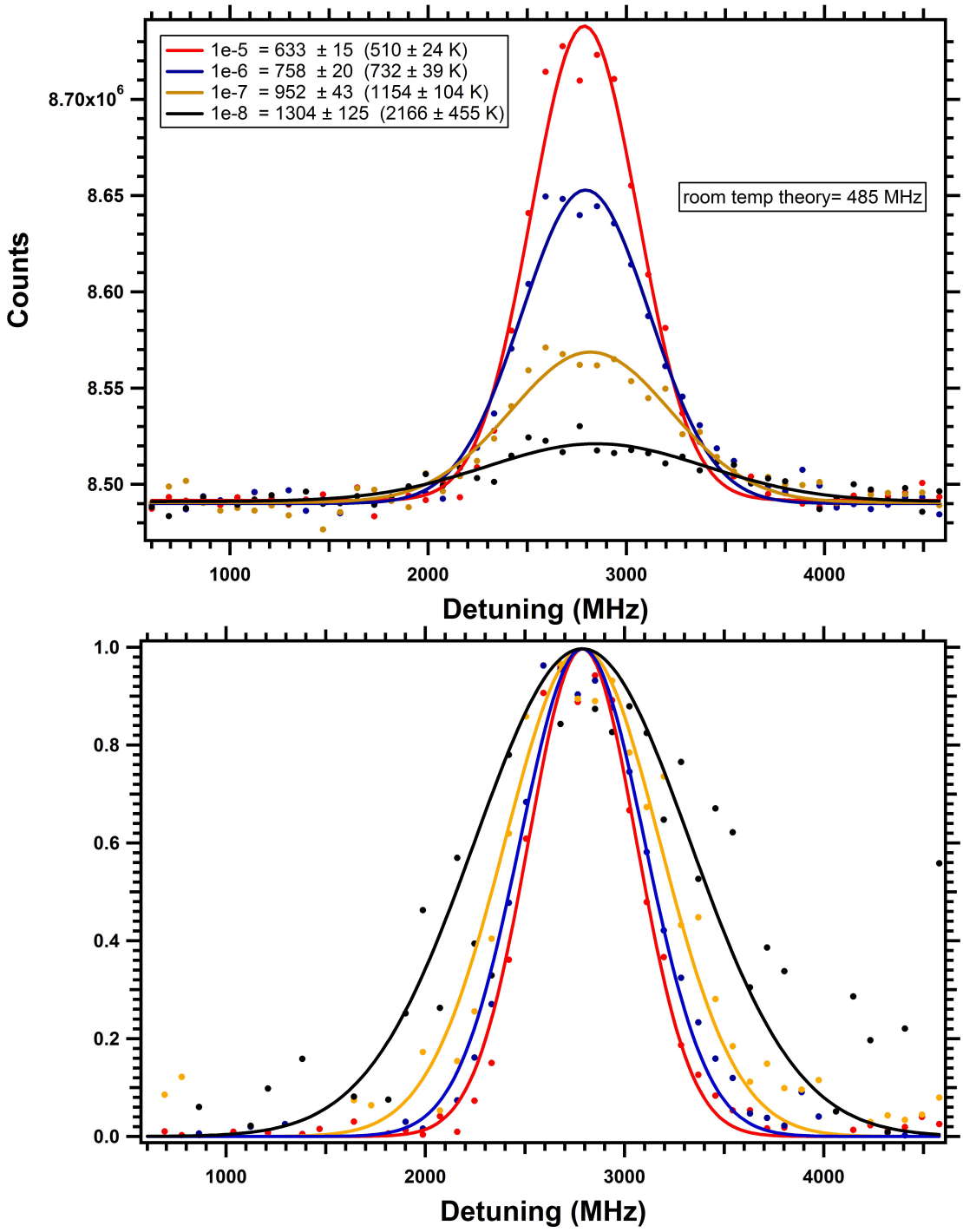

Figure 36: (Upper)Widths (and temperatures implied by Eqn. 22) of Ba^+ fluorescence response as a function of the 650 nm light frequency. (Lower)Height normalized plot of the above data.

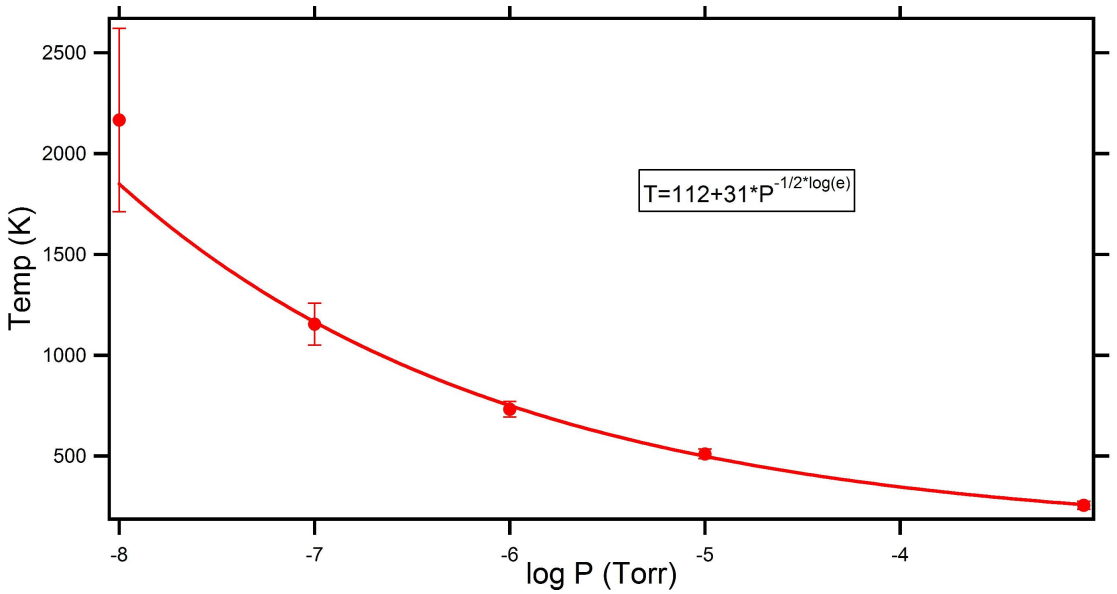

Figure 37: Temperature of the cloud given by figure 36 as a function of buffer gas pressure. An additional point at $4.8\,10^{-4}$ torr is added to the fit from [75].

to 10^{-5} torr. The temperature was calculated using the measured width and Eqn. 22. The peak height gets lower as the buffer gas pressure drops and the temperature rises due to the laser capturing a smaller fraction of velocity classes. If we were cooling on a two level transition, as the ions grew in temperature, the peaks would get broader as shown above, but the total area under the curve would remain constant. However, since here we are using a Λ-system here and the 493 nm laser frequency is fixed, the total fluorescence over a sweep drops as the temperature rises.

Fig. 37 shows the barium cloud temperature for the above data, plus an additional data point at a buffer gas pressure of $4.8 \cdot 10^{-4}$ torr from [75] (see Sec. 2.2.1). We do not suggest any quantitative model for the behavior. But the graph does show what temperature can be expected from Ba^+ in our particular ion trap as a function of buffer gas pressure.

The agreement between the fit to our data and the point given by [75] is noteworthy. In [75] only small numbers of ions were used, whereas we used a cloud of a few hundred ions. A sensible follow-up would be to see how, for a fixed buffer gas

pressure, the temperature of a cloud varies as a function of how many ions are loaded. In this way we could examine what the relative rates of ion-ion collisional heating vs ion-background collisional heating.

4.5 Detection

Several different cameras were investigated for observation of light at 984 nm or 1087 nm. The iXon camera used with barium was not suitable because an etaloning effect occurred when it was illuminated with wavelengths of light at these wavelengths. This was a result of long wavelength photons penetrating too deeply into the chip, which was designed to be used with visible wavelength photons. Any images taken at these IR wavelengths looked like the they were being multiplied by a fixed overlay pattern which would dramatically reduce the observed count rate for certain portions of the chip.

An Andor InGaAs iDus model was among the cameras considered for use with thorium. It has a much higher QE than a silicon based camera at 984 nm (81%) and 1087 nm (85%) and also has low noise. However, it's sensitivity reaches so far into the IR that the camera's target must also be chilled or the camera will read out a very large number of thermal photons. If an appropriate filter could be found and chilled this problem might be overcome. Additionally, it was designed for spectroscopic experiments, and so only had a single 1-D array of pixels, making imaging of trapped coulomb crystals impossible.

The most convenient option was found to be another iXon camera. This one was better designed to work at IR wavelengths, and was previously used in the lab's Rb experiments. It is nearly identical to the barium iXon, but we do not observe any etaloning at 984 or 1087 nm.

Two objectives were used for light collection. In the trap of Sec. 4.1.1 we used the Mitutoyo objective described in Sec. 3.3. In the Sec. 4.1.2 chamber the trap center

was much further away, so a 50 mm diameter achromatic lens with a focal length of 100 mm was used as the objective (NA$\approx$ 0.25).

In searching for Th^{3+} ion fluorescence, as described in Sec. 4.7.3, the barium was used as a camera alignment tool. Since the clouds of barium or thorium will both form in the same area of the ion trap, we loaded barium first and recorded which camera pixels the fluorescence fell on. By only integrating the counts over this region when running the search algorithm described in 4.7.3, we minimized our scatter and pixel readout noise.

Ba^{+} was also be use to align the 984 nm and 690 nm lasers. By overlapping these lasers with the barium light, we could be sure they were fixed on top of where the thorium cloud would form in the trap.

4.6 Th^{3+} Trap Lifetime

After successfully loading Th^{3+} into our ion trap by utilizing ablative loading described in Sec. 4.2, we found that with a chamber vacuum pressure of $\sim 2 \cdot 10^{-10}$ torr, the Th^{3+} ions did not remain in the trap much longer than a minute. Additionally, we observed a decreasing Th^{3+} trap lifetime with increasing buffer gas pressure. Fig. 38 shows the loss of ions as a function of time for a helium buffer gas pressure of 10^{-5} torr.

The most likely loss mechanism is charge exchange. The high ionization energy of Th^{2+} (20 eV) makes charge exchanging collisions (taking Th^{3+} to Th^{2+}) with background molecules more favorable. The ionization energy of helium is high enough (25 eV) that collisions of this type should be unlikely, but we cannot rule them out entirely. We do believe that the majority of loss is due to contaminants leaked in with the helium. The helium supply on the air side of the leak valve was pumped out to rough vacuum, about 10^{-3} torr, then filled with over one atmosphere (760 torr) of helium. The helium we purchased is supposed to have impurities on the order of

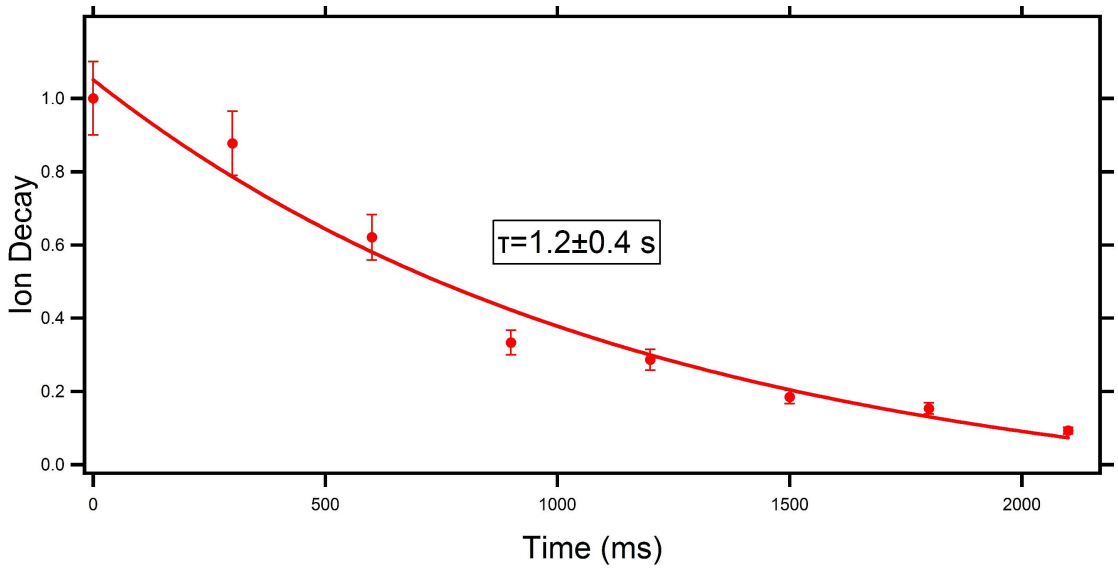

Figure 38: The lifetime of Th^{3+} ions in the trap, before they decay via charge exchange with vacuum or buffer gas contaminants. Ions are loaded via ablation, time elapses, then the ions are ejected from the trap into the CEM. This data was taken at 10^{-5} torr of helium and yielded a lifetime of 1.2 s.

10^{-6}. This implies that the impurities on the air side of the leak valve and those of the cylinder should be roughly equal. Therefore, with a buffer gas pressure of 10^{-5} torr introduced into the chamber, impurities should be of order 10^{-11} torr, still an order less than the baseline vacuum background. So either the impurities must be larger than the calculations would indicate, or line contamination is not the source of ion loss.

4.7 Techniques

4.7.1 Use of the Stability Diagram

Extensive use was made of the rf trap's stability characteristics throughout this experiment. By precisely controlling the values of V_{rf} and U_{dc} being applied to the trap, we can selectively eject unwanted ions. As described in Sec. 2.1, mass filters maintain a ratio of V_{rf} to U_{dc} such that only a vary small range of masses are stable at a given time. Ions formed at one end are filtered and only the stable ions are collected at the other end, generating spectra similar to the one shown in Fig. 31.

This mass filtering technique has some limitations however.

In our work with ablation, we found that the mass filter didn't have a high a level of mass selection for ablated ions as it did for the ions formed by electron impact. This is shown by the broad peak widths in the ablation spectra in Figs. 32 and 33 when compared with the electron impact created ion peaks in Fig. 31. The RGA's length was designed for good filtering of 8 eV ions, which for 232 amu would imply ∼2.5 km/s. This corresponds to the ion experiencing about 95 rf cycles as it traverses the trap. Given our measurement of 12 km/s for $^{232}Th^{+}$ in Sec. 4.2 this means the ion has an energy of 167 eV, or about 20 times higher than the filter is designed for, and a velocity of about 4.5 times higher. This higher velocity and ion energy may be the reason for the reduced mass selectivity.

For trapped ions, mass selection was done in a different manner. Ions are loaded into the trap while $U_{dc} = 0$, then a pulse of U_{dc} is applied for 2 ms or less. Longer pulses can cause loss of ions even if the values of V_{rf} and U_{dc} would be consistent with still being in the stable regime of Fig. 5. After the pulse is applied, the contents of the trap are examined. In the trap of Sec. 4.1.2 this is done by dumping the trapped ions into its CEM and counting the current pulses on its output. In the Sec. 4.1.1 chamber, no electronic readout could be done, so the successful ejection of ions was identified by a change in barium fluorescence. If barium is loaded in tandem with other ions, then after the selection pulse has been applied the barium cloud will take up less volume in the trap (see Fig. 35).

In order to have confidence in this method for identification of unknown ions, we had to first test that the addition of axial trapping electrodes (the trap endcaps) did not perturb the trapping field too much from its theoretical shape. In the chamber of Sec. 4.1.1 this was done by measuring the value of the a parameter at which barium left the trap for a variety of values of q, then comparing this data to the theoretical predictions. This data is shown in Fig. 39. The method used to generate

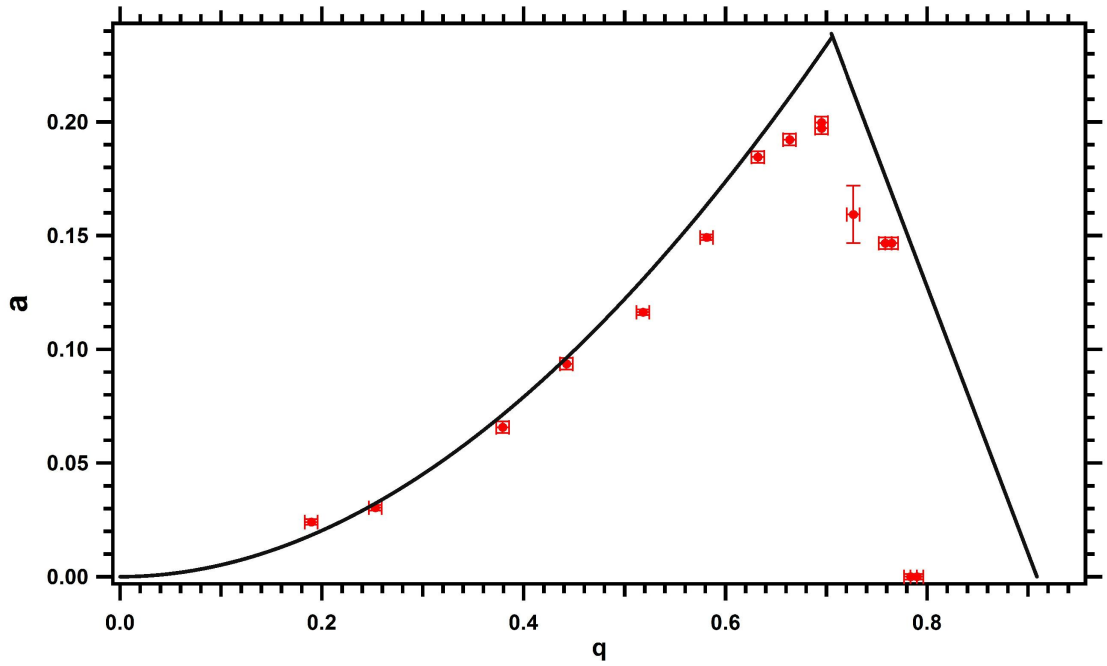

Figure 39: The edges of the stability regime where tested using Ba^+ in the trap of 4.1.1 and compared with theory. A plot is pointed where a pulse of length of a few ms will eject >90% of the loaded ions. Agreement with theory is very good for low 'q' values.

this data follows. First the trap is loaded with barium via either photoionization or the photoelectric effect. Then the trap voltage, V_{rf}, is set to some value; this determines the q stability parameter of the trap. Pulses of DC voltage, which set the value of the a stability parameter, are applied are applied to two of the diagonally opposite trap electrodes. The magnitude of these pulses are stepped incrementally up until we find value of U_{dc} where >90% of the ions (as measured by the observed drop in fluorescence) are ejected from the trap. The error bars represent uncertainty in the applied V_{rf} and U_{dc} voltages applied. As can be seen in the figure, the stability diagram was well approximated for values of q between 0.2 and 0.6.

Using this pulsing technique we identified other ions loaded into our trap by their effect on the barium fluorescence. This was already shown in Fig. 35. For a number of values of V_{rf}, the pulsed value of U_{dc} required for ejection was found, and then the V_{rf},U_{dc} curve was compared with the theoretical shape for a number of candidate

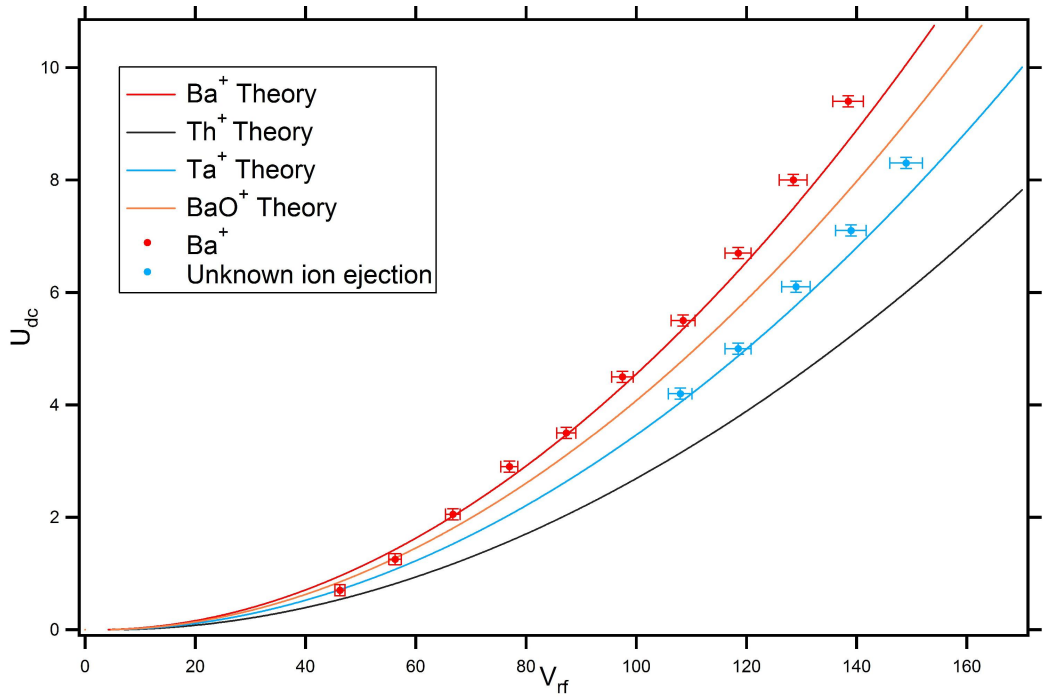

Figure 40: A particular ion species, in this case tantalum, was identified by comparing its measured stability boundary to the theoretical stability boundaries of candidate ions.

ions. Fig. 40 shows data from the identification of tantalum ions. This tantalum was loaded by ablation in the Sec. 4.1.1 chamber. Fig. 41 shows the identification of Th^+ ions loaded with the same setup.

In the chamber described in Sec. 4.1.2 we made more extensive use of the U_{dc} pulsing technique, though the methodology was different. Now, a value of m/e was selected and q was set to 0.705 for that value of m/e. Next the ablation laser was fired. After loading, a U_{dc} pulse consistent with an value of $a = 0.21$ was applied. Then the trap's contents were dumped into the CEM and the number of ions was recorded. This process is repeated for a range of m/e values, generating a spectrum of the ions loaded into the trap by the ablation laser. In Fig. 42 can be seen all the ions we loaded and identified with these techniques: Ba^+, Ba^{2+}, Th^+, Th^{2+}, Th^{3+} and Fe^+. This plot demonstrates the general usefulness of this setup, it should be capable of loading a very wide variety of ion species.

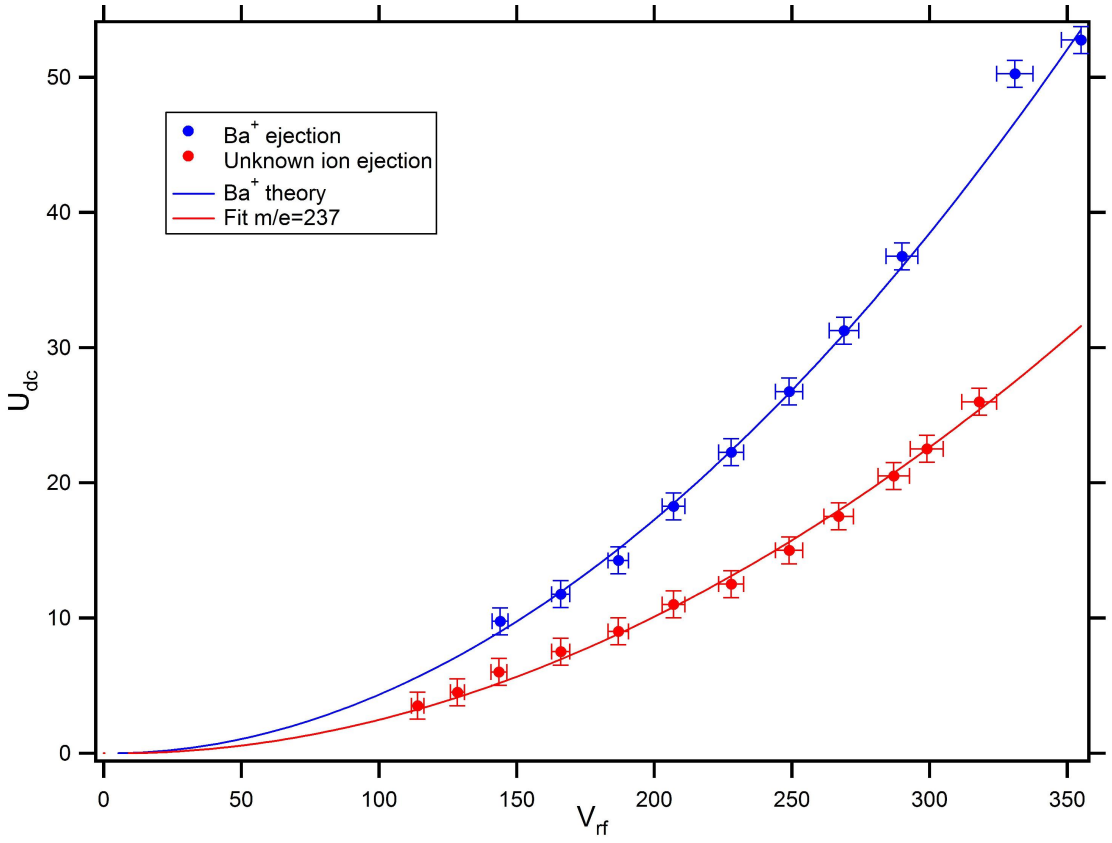

Figure 41: Identification of Th^+. Here the edges of the stability chart were plotted for an ion, and a best fit line was calculated, yielding a m/e of 237±5 amu/e, a good fit to the expected value for Th^+ of 232 amu/e.

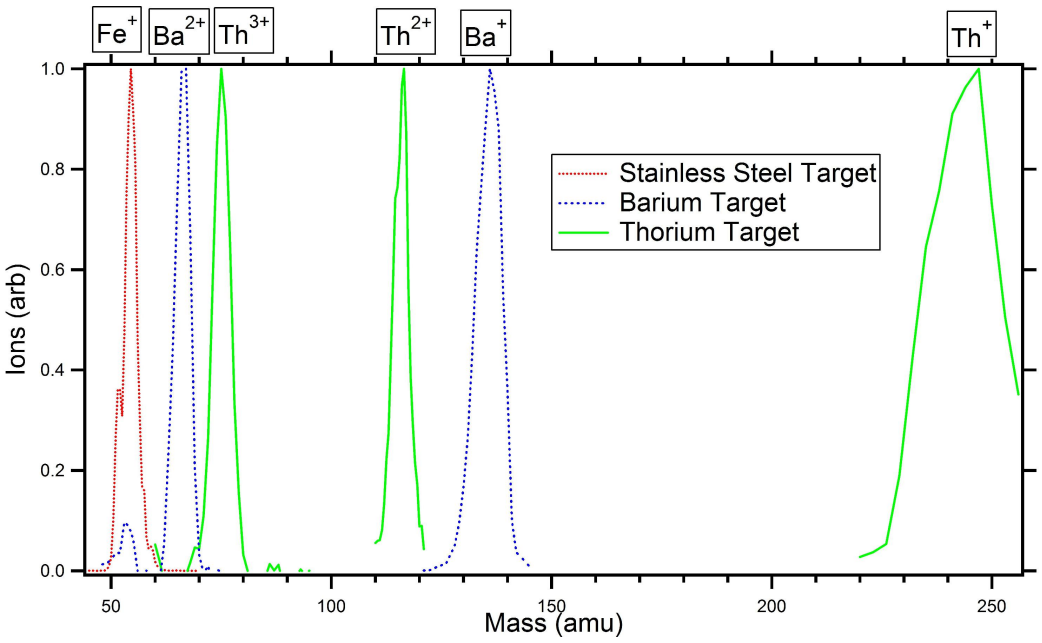

Figure 42: All of the ions loaded with the ablation technique. Their heights are normalized because of the large divergence of yield based on laser power and trap settings for each. High mass peaks are wider because in using a linear ramp of of U_{dc}/V_{rf}, the fractional width $\Delta m/m$ will be constant.

4.7.2 Dynamic and Successive Ablative Loading

Rf traps are conservative, which can make loading via ablation problematic. The ablation ions ions are created outside of the trapping region and so in theory any ions which enter the trap have enough energy to leave it. Some ways of circumventing this limitation are detailed in this section.

One method used was to allow the trap to short. If a high enough ablation pulse energy is used, then the large number of charged particles will pull the rf driving voltage to 0 volts for periods of 20 to 30 μs. When the rf voltage recovers, any ions in the trapping volume will be confined. This is sure to be only the very slowest moving ions from the plume, given the high average velocity of ablated ions, but there are enough of these slow ions to make the technique useful. All the ions in the chamber of Sec. 4.1.1 and in Figs. 40 and 41 where ablatively loaded by shorting out the trap voltage.

Another way of capturing ablated ions is given in [121]. In that work, two plumes of ablated ions moving at right angles to one another collided inside of the trap. In an elastic collision in the trapping region, one ion will be left at rest and the other will move off at an angle with a higher velocity. This technique was used to capture in excess of 10^5 ions. This method may be attempted in our chambers at some future date.

In the Sec. 4.1.2 trap, the ions are created at one end of the chamber, pass through an rf filtering region, then into a trapping region. If the endcaps are held at a fixed voltage, then only ions that are cooled in the time they pass through the space between the endcaps should be trapped. The trapping region is 25 mm long, and with an average plume speed of 12 km/s, the ions only spend 2 μs in the trap. Nevertheless, in this configuration we are still able to trap ions.

There are two mechanisms which may be responsible. Among the slowest ions in the plume, some small fraction will undergo a collision with a background gas molecule, which cools the ion as it traverses the trap. The base pressure in the chamber is $\sim 10^{-10}$ torr, if gas collisions were the mechanism responsible for loading we would expect that when we introduce a buffer gas pressure of 10^{-6} torr that the trapping efficiency would go up by 4 orders of magnitude. While we did observe greater numbers of ions loaded in the presence of buffer gas partial pressures of 10^{-6} or greater, the loading efficiency improvements were always limited to an order of magnitude or less.

Inter-ion forces may slow the ions as they traverse the trap. In our tests of the plume's velocity, we observed that the plume of charge spreads out as it propagates away from the metal target. If the ions near the tail end of the plume have enough energy to enter the trap, but are slowed by their repulsion from the ions in the head of the plume as they traverse the trap, then these slowed ions may be confined.

Loading efficiency can be dramatically improved by changing the voltage values

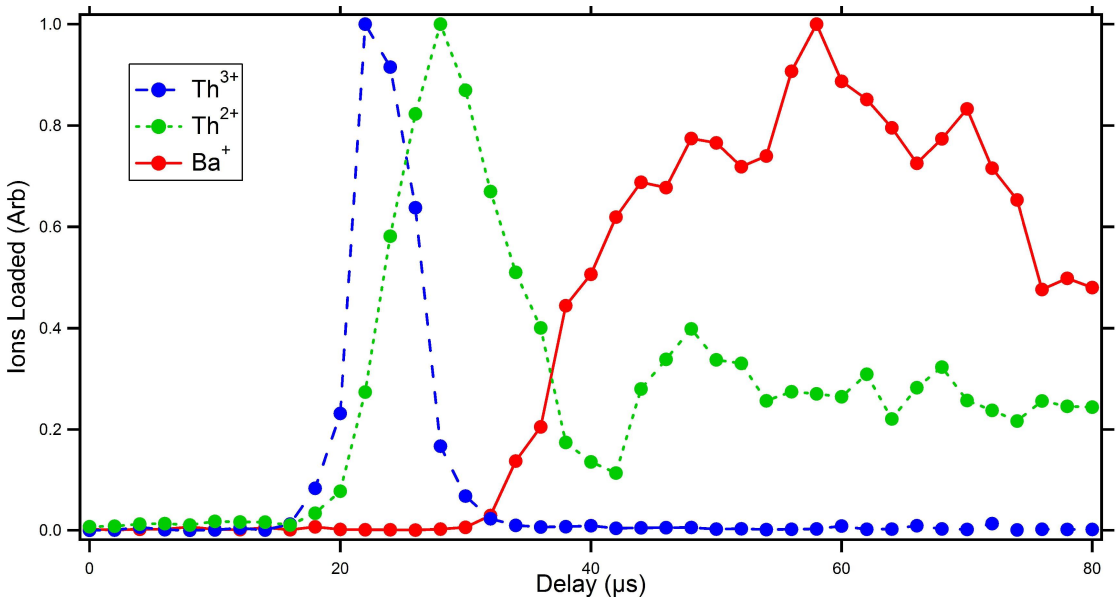

Figure 43: Different ions trapped as a function of the trap opening window. At t=0 the pulse laser fires. The Th^{3+} ions arrive at the trap first and can only be trapped for a narrow time window and Th^{2+} loading is is peaked at a slightly later time. Barium arrives later than either of the others ions and has a much broader peak.

on the endcaps after the ablation laser has fired. The endcap closest to the ablation source (the 'left' endcap) is set to zero volts as the ablation laser fires, then is turned back up to some high value a time later. The endcap further away from the target (the 'right' endcap) is held fixed at a high voltage (∼75 V). Ablated ions travel down through the mass filter, into the trapping region and are turned around by the right endcap. Between the time they enter the trap and the time they are turned around by the right endcap, the left endcap has its voltage turned up, leading to confinement. The appropriate time at which to turn up the left endcap voltage will depend on the velocity of the ions and the distance between the trap and the source.

Fig. 43 shows the window within which the left endcap should have its voltage increased for optimal loading of the ions. Two things are noteworthy about this data. First, the time to turn on the endcap is longer than expected. The ions travel a distance of about 120 mm from the target to the trap, and previous velocity measurements showed the ions moved with an average velocity of 12 km/s making

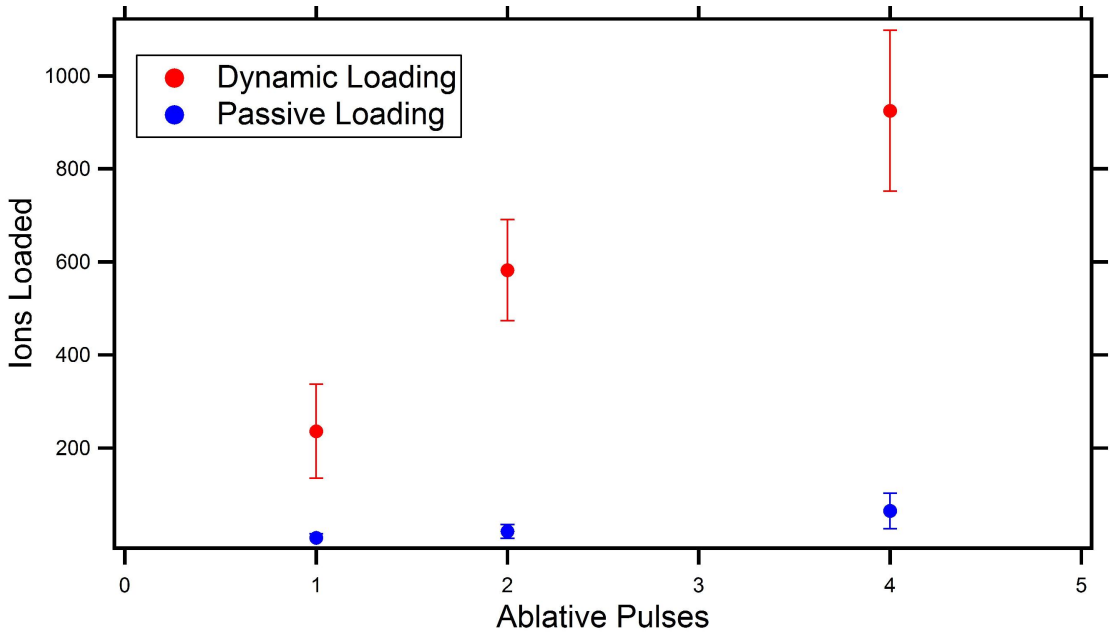

Figure 44: Passive and dynamic loading techniques are compared. In passive loading the endcaps remain fixed for each laser pulse. In the dynamic scheme the left endcap had its voltage lowered to 0 V for a window of 10 μs as the Th^{3+} arrives at the trap.

their expected arrival time at the trap about 10 μs, a much earlier time than any of the shown peaks. Additionally, the optimal turn-on time was observed to be different for each of Ba^{+}, Th^{3+} and Th^{2+} ions.

We also demonstrated that we could add ions from several different ablative pulses together in the trap. Axial secular frequencies for this trap are ~20 kHz or less; this frequency is low enough that we could lower the left endcap for a period long enough to allow additional ions from an ablation into the trap without losing a substantial fraction of the ions captured from previous pulses. We achieved the largest number of ions loaded per ablative pulse by dropping the left endcaps voltage to 0 for 10 μs. Shown in Fig. 44 is a comparison of the techniques for the loading of barium. The single pulse improvement obtained by turning on the left endcap after the ablation laser fires shown by the difference in average number of ions loaded in a single pulse. The additivity is demonstrated by the linear increase of ions with each ablative pulse.

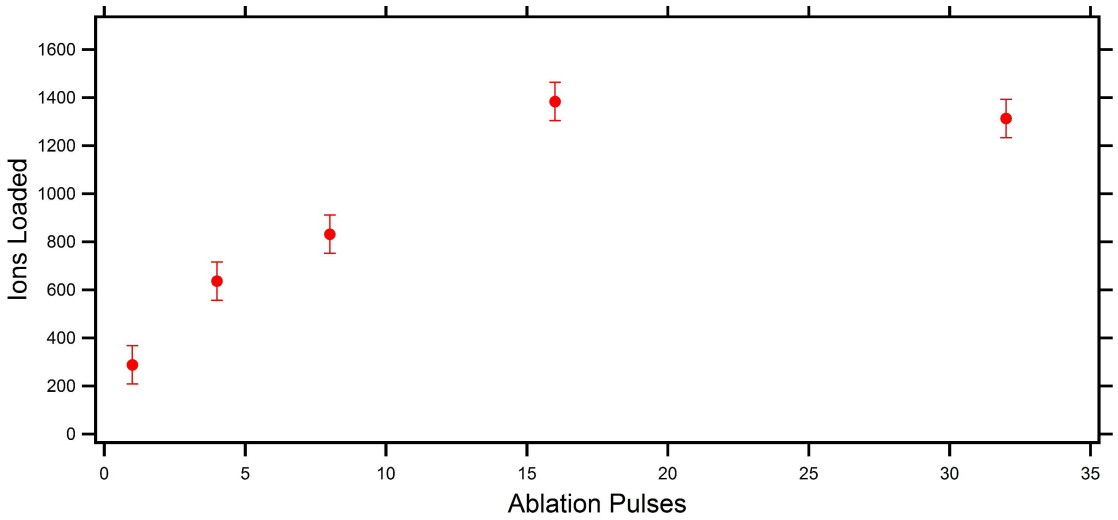

Figure 45: The ablation laser is fired repeatedly, and the trapped ion yield reaches an asymptote when the loading balances the loss due to charge exchange loss of Th^{3+}.

The maximum number of ions loaded is limited by space charging and trap lifetime. The ablation laser fires at a maximum rate of 10 Hz, so ion loading will asymptote when the number of ions loaded in a single shot is equal to the lifetime loss in 0.1 s. This asymptote can be seen in Fig. 45. We were able to load at least 3000 Th^{3+} ions with this technique when the loading was optimal. Given the efficiency of the counting by the channel-electron multiplier, which we have estimated to be 30% (see Sec. 4.1.2), the true maximum was $\sim 10^4$.

If during loading we set U_{dc} to a value close to the edge of the stability region for Th^{2+} and well outside of the region for Th^{+}, but still inside the diagram for Th^{3+}, we were able to trap more Th^{3+} ions. The optimal point of operation for loading Th^{3+} is shown in Fig. 46. The lower charge states of thorium are much more numerous in the plume than is triply ionized thorium. If $U_{dc} = 0$ when the ablation laser was fired, then Th^{+} and Th^{2+} will fill the trap up, nearly its space-charge limit. This limits the Th^{3+} loading to less than it might have been in the absence of Th^{+} ions. The value of U_{dc} selected prevents the unwanted ions from loading into the trap, leaving room for Th^{3+}.

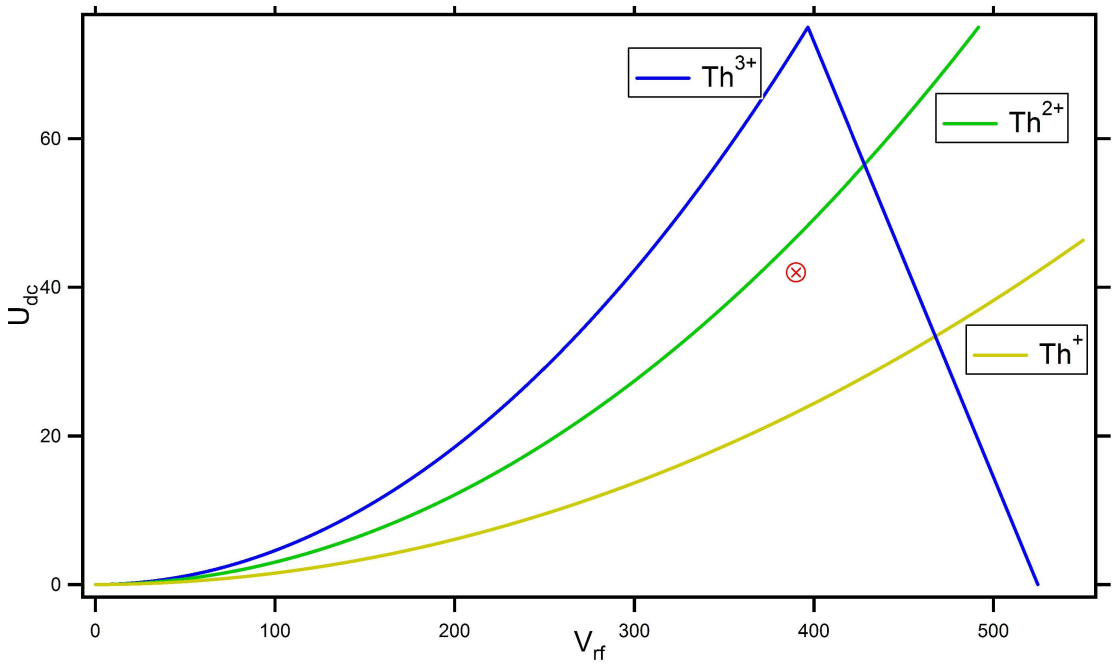

Figure 46: The trapping V$_r f$ and U$_d c$ during loading is indicated by the x'ed circle. The operating point lies above the stability border for Th^+ and near enough to the Th^{2+} border that no significant numbers of those ions are loaded.

4.7.3 Wavemeter Laser Feedback and Ion frequency Scanning

As discussed in Sec. 4.3, a laser frequency scan would be necessary to find the correct laser frequencies for observation of fluorescence, given the uncertainty of the previously reported measurements in [45]. We chose to use the Λ-system at 984 and 690 nm for fluorescence imaging due to the much higher quantum efficiency of our camera at 984 nm, relative to its QE at 1087 nm. A calculation of the time required to load ions into the trap and look for fluorescence at each possible laser frequency showed that a scan of the frequencies ±2.5 GHz on both lasers of the numbers given in [45] would take 8 to 12 hours. Therefore, we desired a frequency reference which was free from drift on the time scale of several hours.

The wavemeter discussed in 3.3 was selected to be our frequency reference. The stated absolute accuracy of the device is 60 MHz, but it was found that the frequency it reported for a locked laser could vary by 200 MHz or more over a few hour period.

The lines on which we would be observing fluorescence in Th^{3+} where 100 times more narrow than the corresponding lines in Ba^{+}. Given this, we could not count on laser cooling to be very efficient. Therefore, we decided to use a buffer gas to cool the ions during the frequency sweep, even though using a high pressure of helium buffer gas clearly shortened the trap lifetime of the Th^{3+} ions. The pressure used during the frequency search was selected to be $5 \cdot 10^{-6}$ torr. This pressure was selected because it allowed us to maintain an trap lifetime of $\sim$4 seconds, ensuring that our ion count asymptoted above 2400 ions, and also that the ion fluorescence would not drop much in the course of a 1 s camera exposure.

The temperature of the ions being buffer gas cooled was likely to be at least 295 K, giving Doppler widths of 248 MHz and 363 MHz for the 984 and 690 nm lines. If the uncertainties we inferred from the number of significant digits in [45] (3 MHz on the 984 nm light and 300 MHz on the 690 nm light) were accurate, then at room temperature almost no frequency scanning should be required. However, since we did not have complete confidence in the uncertainties we inferred from the numbers in [45], a more expansive frequency search than the above calculations would imply might need to be done. Since we desired to have as accurate a frequency reference as possible, we attempted to correct the wavemeter's systematic errors.

Two lasers at 780 nm and 795 nm were locked to the rubidium D1 and D2 lines using saturated absorption spectroscopy on a Rb vapor cell. The wavelengths of these locked lasers were measured as they drifted on the wavemeter. The data can be seen in Fig. 47. In Fig. 47(Upper) the absolute drift for both lasers relative to the known Rb frequency as a function of time is shown. A slow drift can be seen on both lasers with time, in addition to a few large 'hops.' These were also wavemeter errors, and on occasion they would result in frequency jumps of several hundred MHz. These hops were the result of software errors which have since been repaired with updated software provided by the manufacturer. However, they were a source of uncertainty

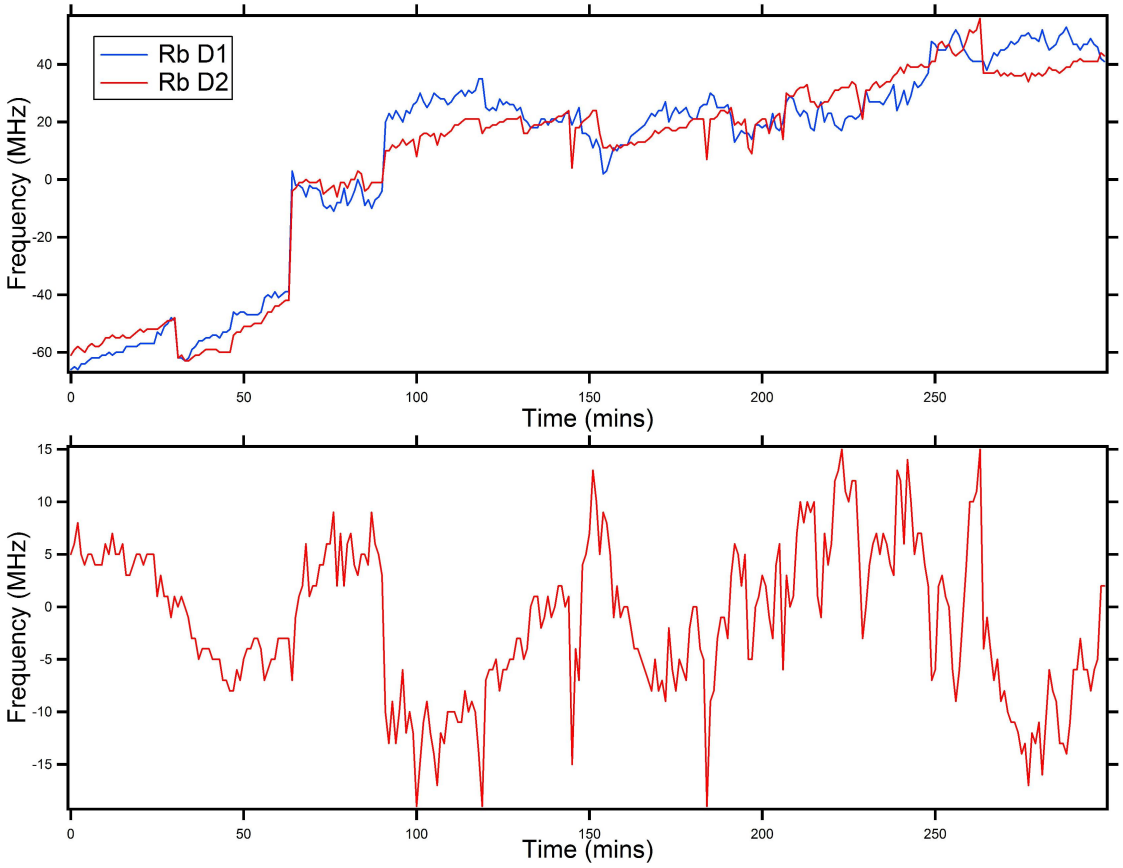

Figure 47: (Upper) Two lasers locked to the rubidium D1 and D2 lines tracked over 4 hours. Drift was over 100 MHz here, but it has been observed to be greater than this over similar periods of time. (Lower) Frequency difference between the two locked lasers was <15 MHz.

when these measurements were originally taken. Fig. 47(Lower) shows the subtracted error difference on both lasers. We observe that, while the absolute accuracy error varied by over 100 MHz, the relative error was less than 15 MHz. If the wavemeter's error was uniform over a wide range of wavelengths, then by performing a frequency measurement of a locked laser, a portion of wavemeter's systematic error could be compensated for.

When performing the Th^{3+} fluorescence frequency scan we would check the wavemeter's reading of a locked laser's wavelength, and use that measurement to properly tune the 984 nm and 690 nm lasers to an accuracy perhaps as small as 15 MHz. So that the comparison with a locked laser and the frequency tuning could be done rapidly, a locked Rb laser, and the 984 and 690 nm lasers were all coupled into a single multi-mode fiber. Three shutters controlled which of the light beams entered the wavemeter at a given time.

A sophisticated LabView program controlled the search process. At the start of operation a number of parameters were imputed: the frequency range and frequency step size for each of the 984 and 690 lasers, the correct timing parameters for optimal loading of Th^{3+}, and a 'threshold,' parameter which will be explained below.

The program would execute several operations in order. First it would take a reading of the Rb laser light and record the frequency error offset, then it would in turn look at each of the 984 nm and 690 nm lasers. For each laser, a feedback mechanism would tune the piezo so that the desired laser frequency was achieved. Then the YAG laser would ablate the target $\sim$12 times in an attempt to load Th^{3+}. Next the camera would be triggered to take a one second exposure. The number of camera counts was saved to be later correlated with the laser frequencies at which that particular camera shot was taken. After the exposure the right endcap of the trap was lowered to -1 V, dumping the trapped ions into the CEM If the number of ions counted was less than the threshold value, then the process would be repeated at

the same laser frequencies. If the number was above the threshold, then the program proceeded on to the next set of laser frequencies. Only one set of laser frequencies was checked for each trap load because of the limited lifetime of Th^{3+} in the trap. The threshold was selected to be a high but readily achievable number of ions, so that at each frequency step we could maximize our chances of observing fluorescence. It was necessary to set this minimum because the ablation technique's ion loading variance is so high.

The process was mostly automated. It only required that we turn up the ablation laser power every few minutes to keep the number of Th^{3+} counts high, and make sure none of the lasers mode hopped or the Rb laser lost its lock. This level of automation was vital so that we could cover a large range of frequencies in a reasonable period of time.

4.8 Results

Using the fluorescence search program described above we scanned a frequency range of ±2500 MHz in 50 MHz steps on both the 984 nm and 690 nm laser over the course of two days. Fig. 48 shows the result of this scan. For each frequency pair a number is plotted indicating the number of camera fluorescence counts observed in a one second exposure divided by the number of ions present in the trap for that measurement. Going back over the high count region in the vicinity of +100 MHz on the 984 nm and +1800 MHz on the 690 nm we found this high count region was due to thorium ion fluorescence. Fig. 49 shows a fluorescing cloud of $\gtrsim$ 2000 Th^{3+} ions. By measuring the wavelength of the line center over several days, we have determined the Λ-system wavelengths to be **984.15498(16) nm (304.619420(50) THz)** and **690.30844(17) nm (434.291350(100) THz)**.

Next we examined the width of the fluorescence peak. Fig. 50 shows a closer look at the thorium fluorescence peak. Fitting a 2-D Gaussian to this data we see a FWHM

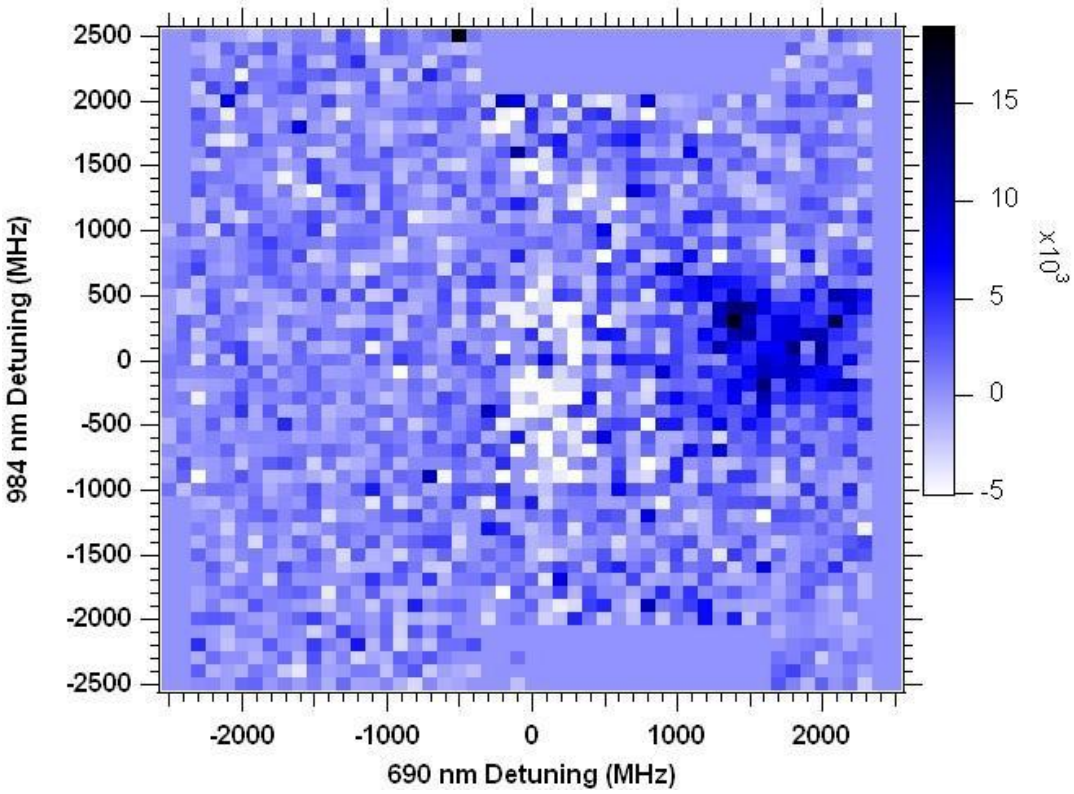

Figure 48: Frequency search grid for the 690 nm (x-axis) and 984 nm (y-axis) lasers. Both lasers were swept over ±2500 MHz relative to the published values in [45] (304.619290 THz and 434.289500 THz) in 50 MHz step increments. Frequencies where the number of observed fluorescence counts were high are indicated by dark blue/black pixels, low counts are light blue/white pixels.

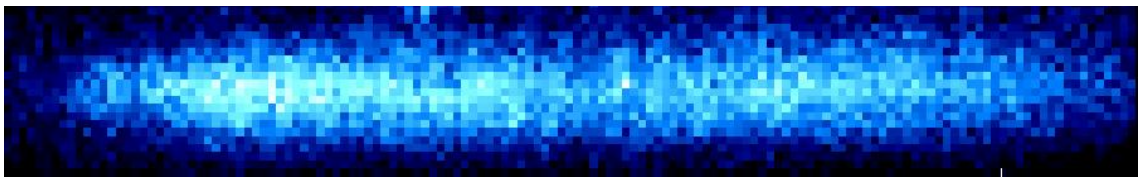

Figure 49: Picture of a fluorescing cloud of ∼3000 $^{232}Th^{3+}$ ions

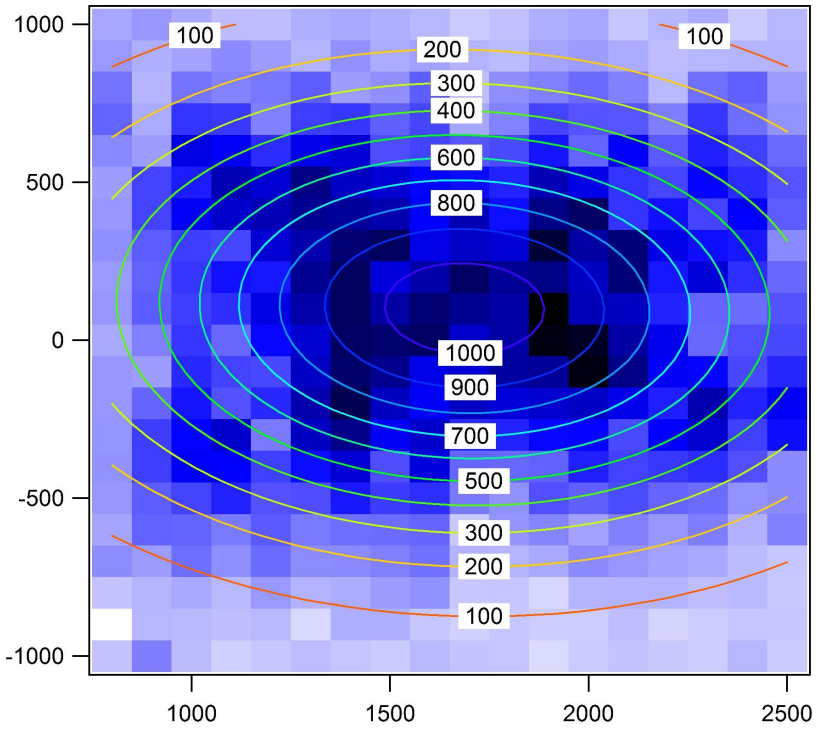

Figure 50: Thorium ions fluorescence spectrum with $4\,10^{-6}$ torr helium buffer gas. Axes are as in Fig. 48. The FWHM for each of the lasers are 745 ± 27 MHz for 690 nm light, 1045 ± 20 MHz for 984 nm light

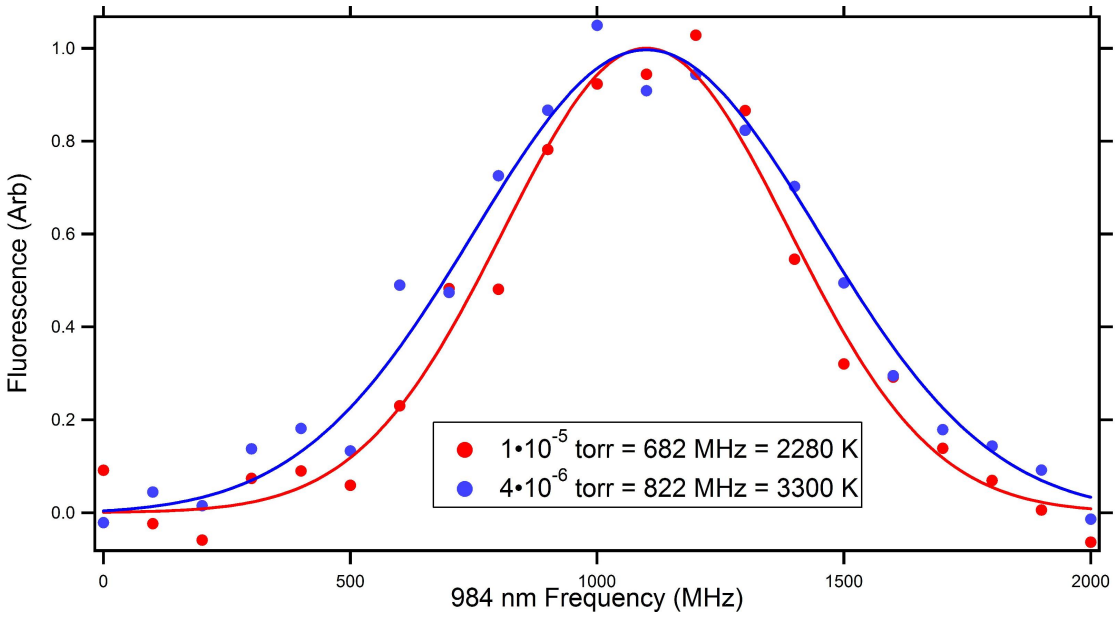

Figure 51: Height normalized fluorescence peaks for 984 nm transition for two buffer gas pressures. As with barium, the ions are hotter when less buffer gas is in the chamber

of 745 MHz for the 984 nm line and 1045 MHz for the 690 line. Some variation in width was observed day-to-day, but was consistent for scans taken in succession. The ratio between the two widths is equal to the ratio of the two laser frequencies, further suggesting these widths are determined by the cloud temperature. The temperature implied by the above widths is ∼2700 K. This is a much higher temperature than was measured for a barium cloud with an equivalent buffer gas pressure (see Fig. 36).

The width of the 984 nm fluorescence response was measured as a function of buffer gas pressure, the result is shown in Fig. 51. The 690 nm laser was held fixed as the 984 laser was scanned. While the higher buffer gas pressure of 10^{-5} torr yielded a more narrow peak, this measurement is more complicated than the similar measurement in barium. Each point in a thorium scan is obtained from a different set of ions, since the ions do not have a long enough trap lifetime for the frequency scan to be completed before a substantial number of Th^{3+} ions decay from the trap. Though each fluorescence measurement is normalized by the number of ions read out by the CEM, if the temperature depends on the number of ions and can vary significantly,

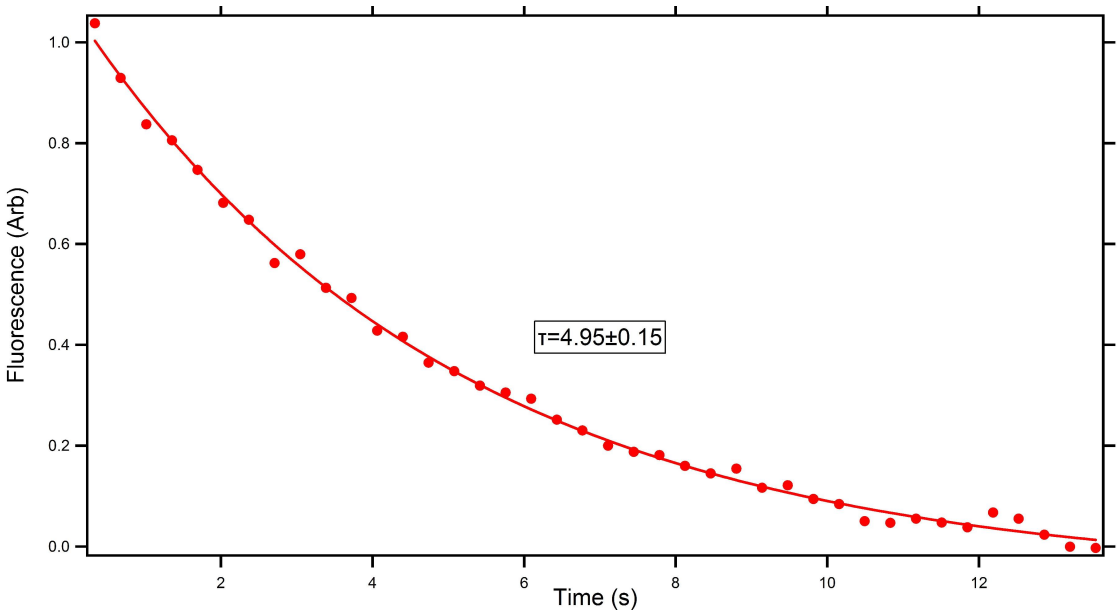

Figure 52: Trap lifetime of Th^{3+} with 3 10^{-6} torr of buffer gas. Similar measurement to Fig. 38, but now viewing the cloud fluorescence instead of doing an electronic readout of ions. The lifetime is longer here because of an improvement in the base vacuum and because a lower buffer gas pressure was used.

noise will be added to the data.

Loss of Th^{3+} ions from the trap was previously measured electronically by dumping trapped ions into the CEM after a delay, this was shown in Fig. 38. We can now measure the decay by directly observing a decrease in cloud fluorescence as function of time, this is shown in Fig. 52.

The branching ratio of the upper state in the Λ-system was also measured. We used two light filters so that we could separately measure a number of counts per ion in a one second exposure for both the 984 and 690 nm transitions. This data can been seen in Fig. 53. In both graphs, for high number of ions, the fluorescence as a function of ion number becomes nonlinear. This is due to the discriminator on the CEM's output not being able to count pulses properly for numbers of dumped ions much larger than 1700. Above ∼1700 trapped ions the CEM pulses begin to bleed together.

The 984 nm light filter used was a colored glass filter with a transmission (T) of

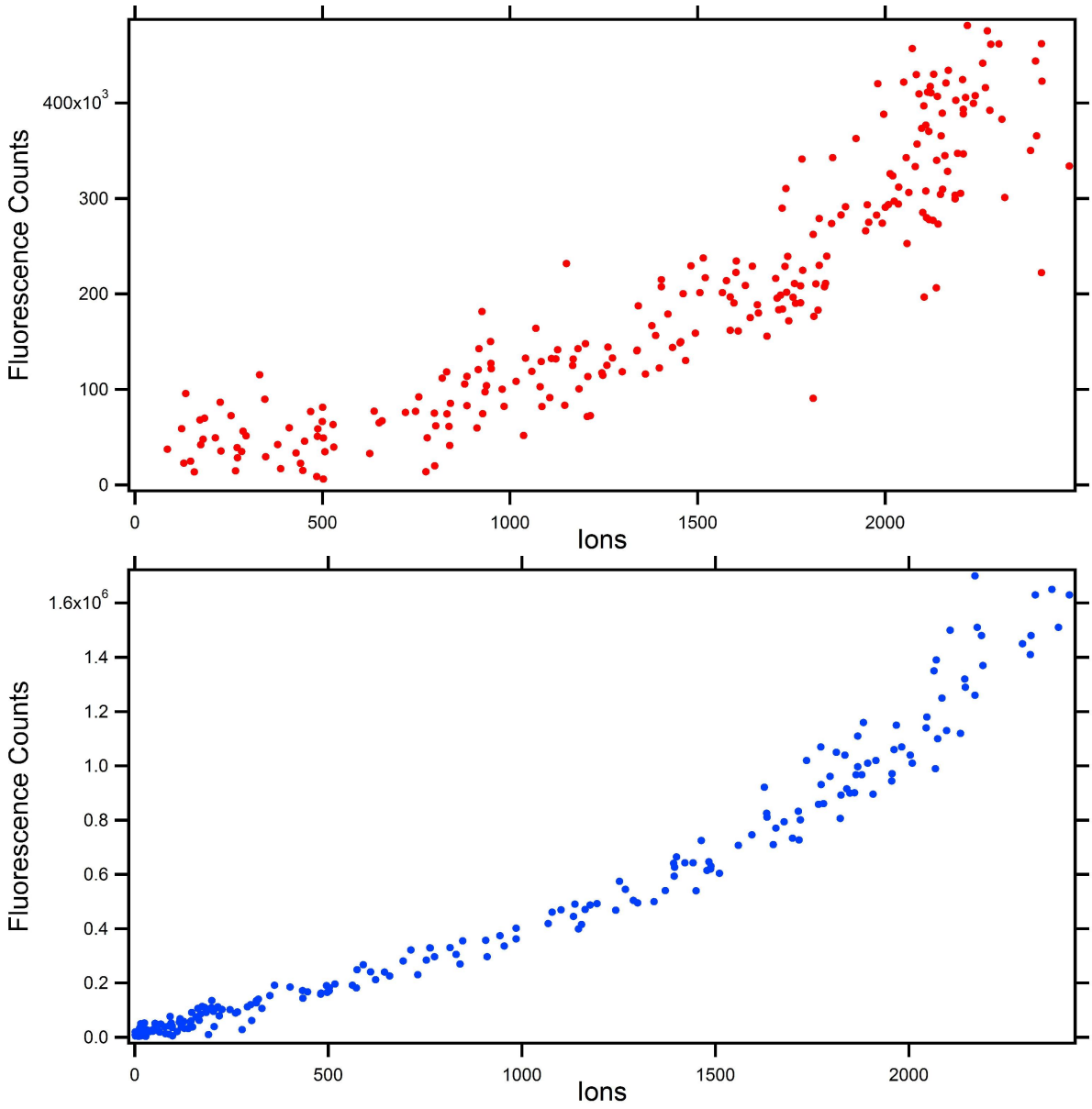

Figure 53: CCD camera counts in a 1 s exposure vs number of ions. (Upper) 690 nm fluorescence (Lower) 984 nm fluorescence.

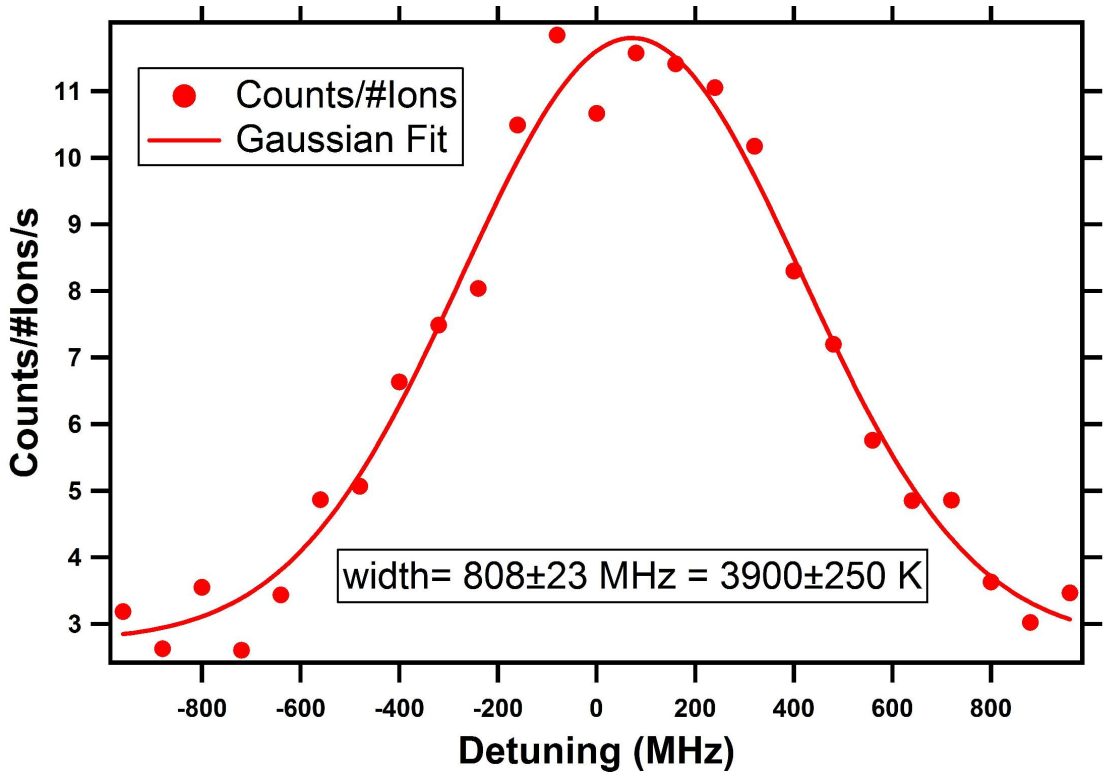

Figure 54: Fluorescence counts observed at 1087 nm vs laser detuning relative to wavelength given by [45] of 275.606560 THz.

0.95 ± 0.05 at 984 nm and T<0.01 at 690 nm. The filter used in the upper graph was an IR cutoff filter with a T≈ 0.06 at 984 nm and T= 0.60 ± 0.05 at 690 nm. Fitting a line to the linear portions of each graph, and using the fact that the QE of the camera at 984 is 18% at 984 nm and 85% at 690 nm, gives 1960 photons/ion/s collected at 984 nm and 189 photons/ion/s collected at 690 nm. This gives a branching ratio of **1:10(1)**, in good agreement with the 1 : 10.5 calculation by [119].

We also observed fluorescence from the 1087 nm transition. Despite the extremely low quantum efficiency of the camera, it was still possible to observe this fluorescence due to the large number of ions loaded. A scan over the transition can be seen in Fig. 54. This measurement was taken at $4 \cdot 10^{-6}$ torr buffer gas pressure. The line center was determined to be **1087.75538(20) nm (275.606600(50) THz)**. Its width would indicate a higher temperature than for the Λ-system shown above, but

the large uncertainty on the fit prevents a conclusion of inconsistency between these results.

The primary problem with comparing any of the Doppler widths measured to each other is that the data was taken over many different trap loadings due to the limited trap lifetimes of the Th^{3+} ions. The final Doppler temperature of the cloud will depend on both the rf heating rate and cooling rate. Potentially, the final temperatures observed will be dependent on the number of ions in the trap (see Sec. 2.2.1). For the most accurate temperature measurements the number of ions should be similar for each data point. In the 1087 nm Doppler scan, we have to use very high number of ions to see a significant amount of fluorescence, especially away from the line center. Generally this number high enough that we cannot accurately count them with the CEM. This may explain why the 1087 measurement temperature seems to be hotter than that of the 984 or 690 nm. It would also explain why the barium temperature is lower; since so few ions are needed to observe Ba^+ fluorescence, fewer ions are often loaded when working with Ba^+.

In the final Chapter of this thesis, the results of both experiments will be reviewed. This is followed by an enumeration of the next few steps required to advance these experiments, along with the hurdles which will have to be overcome to proceed.

CHAPTER V

DISCUSSION AND OUTLOOK

This thesis has presented our progress towards the goals of two ion trapping experiments. In the first experiment, we aim to achieve strong coupling between a single Ba^+ ion and a singe photon confined in a high-finesse optical cavity. Ba^+ ions where created through the use of electron impact, photoelectric and photoionization techniques and loaded into a linear ion trap. The photoionization technique was developed by us and has demonstrated its ability to load any isotope of barium with an abundance greater than 2%. Additionally, photoionization may ameliorate the difficulties associated with charge buildup on insulating surfaces near the trap. Photoionization will also reduce the rate of degradation of highly reflective cavity mirror surfaces since this technique requires lower flux of neutral vapor than electron impact ionization to achieve a high rate of ionization.

Next, a high finesse optical cavity was constructed. Mirrors where cleaned, where positioned precisely by a micrometer and were then glued to a piezo crystal to control their spacing. This cavity is 1 mm long; this length was selected since this will be a large enough spacing to fit a miniature ion trap between its mirrors in the next stage of this experiment. Its mode volume remains small enough that strong single atom-photon interactions should be observable.

The second half of this thesis has presented our progress towards a controlled excitation of the low energy isomer state of ^{229}Th. Our contribution was to create and trap $^{232}Th^{3+}$ ions, confine them for long periods under ultra-high vacuum ($<10^9$ torr) and discover the laser frequencies at which they would fluoresce. The more common 232 amu isotope was used both because of the high cost of ^{229}Th and because of the

greater simplicity in cooling $^{232}Th^{3+}$. Triply ionized thorium was used because of its simplified energy level structure when compared with Th^{+} or Th^{2+}. The use of an ion instead neutral thorium should greatly suppress the undesirable internal conversion isomeric decay channel of ^{229m}Th.

$^{232}Th^{3+}$ ions were created by focusing the third harmonic of a pulsed YAG laser onto a thorium metal plate. The created ions are ejected from the surface with high velocity. By modulating the confining potential of a linear rf ion trap, constructed from a modified commercial residual gas analyzer, we were able to trap large numbers of ions additively from several different ablative pulses. Up to 10^4 ions where loaded in the ion trap at once. We can ensure the loading only of Th^{3+} by using the charge-to-mass selectivity of the ion trap. Additionally, we can electronically count the number of loaded ions by ejecting them from the ion trap into a channel-electron multiplier.

Barium ions were used as a guide at several stages of this work. Traps were tested and their stability parameters compared with theory by loading and ejecting barium from them. Barium fluorescence served as a guide for alignment of laser light and CCD cameras.

Upon initial loading, or after long periods without cooling, trapped ions will assume a temperature which is a substantial fraction of the trap depth of 10^5 K. For initial cooling, a helium 'buffer gas' is introduced into the vacuum chamber. Collisions between the hot thorium and the room temperature helium cool the trapped ions. After ions were successfully loaded and cooled via the buffer gas, an extensive search of the two laser frequencies at 984 nm and 690 nm was undertaken. By referencing a precise wavemeter, lasers at frequencies of 984 nm and 690 nm were incrementally stepped in the region of the previously published transition frequencies. Fluorescence was found at wavelengths **984.15498(16) nm**, **690.30844(17) nm** and **1087.75538(20) nm**. The branching ratio of the $D_{5/2}$ state was determined to be **1:10(1)**.

5.1 Future Directions

5.1.1 Ba^+ Cavity QED

Several issues will need to be addressed in the short term to meet the immediate goal of strong coupling between an ion and a single photon confined in an optical cavity. A miniature ion trap will have to be built and tested. In order to minimize the possibility of the dielectric mirrors have a deleterious effect on the trapping potential, the ion trap will be designed so that its whole structure fits between the cavity mirrors. A trap small enough to fit between the mirrors may deviate substantially from the the theoretical model and its potential depth will be substantially lower ($\sim 10^3$ K) than the other traps used in this experiment. Additionally, despite efforts to shield the trapped ion, any charge accumulation on the mirror surfaces may contribute to trap instability.

The mirrors themselves could also be ruined quite easily. Barium has been observed to adhere quite readily to all of the traps with which it has been used. If the mirrors are not protected from the atomic vapor then is likely that the cavity performance will degrade over time. While the current design calls for a trap which can be moved out of the cavity, which would allow the atomic beam to be kept away from the mirrors, it may not be feasible to move the trap every time it needs to be re-loaded. Other similar experiments done with Ca^+ ions ([22]) have utilized a segmented trap, where ions could be loaded in one region and then shuttled into the cavity.

Small traps also suffer from *anomalous heating* [122], an additional source of heat which would drive the ions in addition to the rf heating described by this thesis. However, since we do not require cooling to the ground state of the trap to reach strong coupling and the Lamb-Dicke limit, and the rate of Doppler laser cooling is much greater than the anomalous heating rate, this may not be a concern.

5.1.2 ^{229}Th Isomer Excitation

Though this study was a step towards the controlled excitation of the ^{229m}Th state, several hurdles lie ahead before the experiment's goal may be accomplished. A sample of ^{229}Th must be obtained. While ^{232}Th is not inexpensive, a 25 mm x 25 mm x 1 mm sample costs ∼$1900, it is vastly easier to obtain than ^{229}Th. The 229-isotope is not found in any significant amounts naturally. Instead the majority of ^{229}Th used in experiments is obtained from the decay of ^{233}U, which is in turn created through neutron absorption by ^{232}Th. ^{229}Th's half-life is 7340 years, so a sample, once obtained, should last a long time.

Additionally, in this work we used a sample of ^{232}Th metal as our atomic source, since it provided unambiguous evidence of Th^{3+} ion production when it was ablated. However, ^{229}Th is usually only available as a nitrate ($Th(NO_3)_4$). Th^{3+} was never directly observed in our ablation tests of Th^{3+}, though Th^{2+} was.

The cost of the ^{229}Th will pose certain difficulties as well. The price of ^{229}Th is about $50000 per mg. Therefore, since each ablation yields about $\lesssim 10^{15}$ ions and neutral particles [118], we can expect to use $\lesssim$ 380 ng of material per ablation, implying a cost per ablation of $\lesssim$ $20. Given that we can see noticeable amounts of material missing from the metal target after a few days of loading, with some thousands of shots per day, the 10^{15} number may be an underestimate, or only be applicable when using much lower pulse energies than we presently do.

Presently, each ion loaded into the trap has a lifetime of only a few seconds when using a buffer gas pressure of $> 10^{-6}$ torr. However, with a background vacuum pressure of $2 \cdot 10^{-10}$ and no buffer gas we see lifetimes of a minute or more. Firing the ablation laser hundreds of times a day may be infeasible when working with a ^{229}Th sample from a cost standpoint. Therefore, we will need to improve the quality of the vacuum so that longer lifetimes may be achieved.

Assuming a long (several hour) vacuum lifetime could be achieved, a more specialized trap structure might be constructed to maximize the capture and usage of ablated ions. A very large ion trap near the target could be attached to a much smaller one farther away. The large trap would attempt to maximize the capture of Th^{3+} from the ablation plume and be loaded only rarely. The large trap could then serve as a source of ions shuttled into a more useful small ion trap in which the experiment would be conducted.

Once $^{229}Th^{3+}$ has been successfully loaded the next step will be to find its hyperfine structure. The ground state of Th^{3+} is $^2F_{5/2}$ ($J = 5/2$) and the nucleus has $I = 5/2$, giving 6 energy levels ($F = 0..5$) in the ground state manifold. Excitation of each of these states will likely be achieved by employing electro-optic modulation of the driving laser. Alternatively, given the possibility that the hyperfine splitting may be small, it is possible that we could simply saturate the whole manifold by power broadening the relevant transitions. However, this latter technique has the possibility of interfering with detection of successful isomer excitation via the shelving technique, depending on the size of the chemical shift of the line being driven.

Once the hyperfine structure has been mapped it will be possible to observe fluorescence from the Th^{3+} ions in their ground state. Some of the difficulties involved in the final step of this work, namely the excitation of the isomer state, were detailed in Sec. 1.2.3. Some further details on hurdles which will have to be overcome are elaborated on here.

The 163 nm (7.6 eV) isomer excitation light may have a deleterious effect on the trapped ions. Every metal which could be used to construct the trap will have a work function less than 7.6 eV. When the isomer light is shined on the ions, any light impinging onto the trap structure will eject electrons via the photoelectric effect. In this experiment, photoelectrons created might ionize trapped Th^{3+}, making identification of successful shelving more difficult. However, if the electron bridge were used

for excitation, then the highest energy photons needed would be 5.7 eV. In this case, the trap could be coated in a high work function material like platinum; this would prevent the creation of photoelectrons.

Initially, it is likely that the efficiency of the shelving process will be low. The wavelength of the isomer transition is only known approximately (7.6 ± 0.5 eV), and a powerful coherent light source may not be available to drive it even if an accurate measurement of that energy was made. If the excitation efficiency is low then a strategy would be to try to drive more ions. However, applying the light to more ions makes the shelving detection more difficult. If instead of a cloud of ions, the trapped $^{229}Th^{3+}$ were cooled into a coulomb crystal then the ions will remain in fixed positions. Therefore, the fluorescence of each ion can be independently monitored with a CCD camera. Then, even with a large number of ions, a single excitation could be detected by observing the darkening of a single lattice site.

It may also be possible to observe fluorescence from an ion in the ^{229m}Th state. Since the hyperfine states of ^{229g}Th will be known at that point in the experiment, those of ^{229m}Th might be calculated. If this were done, it would be possible to directly observe fluorescence from the $^{229m}Th^{3+}$ ion.

REFERENCES

[1] D. J. Wineland, R. E. Drullinger, and F. L. Walls. Radiation-pressure cooling of bound resonant absorbers. *Physical Review Letters*, 40(25):1639–1642, (1978).

[2] W. D. Phillips and H. Metcalf. Laser deceleration of an atomic-beam. *Physical Review Letters*, 48(9):596–599, (1982).

[3] J. E. Bjorkholm, R. R. Freeman, A. Ashkin, and D. B. Pearson. Observation of focusing of neutral atoms by dipole forces of resonance-radiation pressure. *Physical Review Letters*, 41(20):1361–1364, (1978).

[4] W. H. Oskay, S. A. Diddams, E. A. Donley, T. M. Fortier, T. P. Heavner, L. Hollberg, W. M. Itano, S. R. Jefferts, M. J. Delaney, K. Kim, F. Levi, T. E. Parker, and J. C. Bergquist. Single-atom optical clock with high accuracy. *Physical Review Letters*, 97(2):–, (2006).

[5] M. H. Anderson, J. R. Ensher, M. R. Matthews, C. E. Wieman, and E. A. Cornell. Observation of bose-einstein condensation in a dilute atomic vapor. *Science*, 269(5221):198–201, (1995).

[6] A. Steane. Quantum computing. *Reports on Progress in Physics*, 61(2):117–173, (1998).

[7] T. Chaneliere, D. N. Matsukevich, S. D. Jenkins, S. Y. Lan, T. A. B. Kennedy, and A. Kuzmich. Storage and retrieval of single photons transmitted between remote quantum memories. *Nature*, 438(7069):833–836, (2005).

[8] O. A. Collins, S. D. Jenkins, A. Kuzmich, and T. A. B. Kennedy. Multiplexed memory-insensitive quantum repeaters. *Physical Review Letters*, 98(6):–, (2007).

[9] S. Chu, J. E. Bjorkholm, A. Ashkin, and A. Cable. Experimental-observation of optically trapped atoms. *Physical Review Letters*, 57(3):314–317, (1986).

[10] T. M. Fortier, N. Ashby, J. C. Bergquist, M. J. Delaney, S. A. Diddams, T. P. Heavner, L. Hollberg, W. M. Itano, S. R. Jefferts, K. Kim, F. Levi, L. Lorini, W. H. Oskay, T. E. Parker, and J. E. Stalnaker. Precision atomic spectroscopy for improved limits on variation of the fine structure constant and local position invariance. *Physical Review Letters*, 98(7):–, (2007).

[11] L. Essen and J. V. L. Parry. Caesium resonator. *Nature*, 176(4476):281–282, (1955).

[12] R. Wynands and S. Weyers. Atomic fountain clocks. *Metrologia*, 42(3):S64–S79, (2005).

[13] H. G. Dehmelt. Mono-ion oscillator as potential ultimate laser frequency standard. *Ieee Transactions on Instrumentation and Measurement*, 31(2):83–87, (1982).

[14] H. J. Briegel, W. Dur, J. I. Cirac, and P. Zoller. Quantum repeaters: The role of imperfect local operations in quantum communication. *Physical Review Letters*, 81(26):5932–5935, (1998).

[15] J. I. Cirac, P. Zoller, H. J. Kimble, and H. Mabuchi. Quantum state transfer and entanglement distribution among distant nodes in a quantum network. *Physical Review Letters*, 78(16):3221–3224, (1997).

[16] R. Blatt and D. Wineland. Entangled states of trapped atomic ions. *Nature*, 453(7198):1008–1015, (2008).

[17] A. M. Steane and D. M. Lucas. Quantum computing with trapped ions, atoms and light. *Fortschritte Der Physik-Progress of Physics*, 48(9-11):839–858, (2000).

[18] I. Stewart. Quantum cryptography - schrodinger catflap. *Nature*, 353(6343):384–385, (1991).

[19] E. Knill, R. Laflamme, and G. J. Milburn. A scheme for efficient quantum computation with linear optics. *Nature*, 409(6816):46–52, (2001).

[20] M. Keller, B. Lange, K. Hayasaka, W. Lange, and H. Walther. Continuous generation of single photons with controlled waveform in an ion-trap cavity system. *Nature*, 431(7012):1075–1078, (2004).

[21] M. Hijlkema, B. Weber, H. P. Specht, S. C. Webster, A. Kuhn, and G. Rempe. A single-photon server with just one atom. *Nature Physics*, 3(4):253–255, (2007).

[22] M. Keller, B. Lange, K. Hayasaka, W. Lange, and H. Walther. Deterministic coupling of single ions to an optical cavity. *Applied Physics B-Lasers and Optics*, 76(2):125–128, (2003).

[23] M. J. Gibbons, S.Y. Kim, K. M. Fortier, P. Ahmadi, and M. S. Chapman. Achieving very long lifetims in optical lattices with pulsed cooling. *Physical Review A*, 78, (2008).

[24] E. Peik and C. Tamm. Nuclear laser spectroscopy of the 3.5ev transition in th-229. *Europhysics Letters*, 61(2):181–186, (2003).

[25] G. Werth, T. Beier, S. Djekic, H. J. Kluge, W. Quint, T. Valenzuela, J. Verdu, and M. Vogel. Precision studies in traps: Measurement of fundamental constants and tests of fundamental theories. *Nuclear Instruments & Methods*

in Physics Research Section B-Beam Interactions with Materials and Atoms, 205:1–8, (2003).

[26] V. V. Flambaum. Enhanced effect of temporal variation of the fine structure constant and the strong interaction in th-229. *Physical Review Letters*, 97(9):–, (2006).

[27] X. T. He and Z. Z. Ren. Temporal variation of the fine structure constant and the strong interaction parameter in the th-229 transition. *Nuclear Physics A*, 806:117–123, (2008).

[28] A. C. Hayes and J. L. Friar. Sensitivity of nuclear transition frequencies to temporal variation of the fine structure constant or the strong interaction. *Physics Letters B*, 650(4):229–232, (2007).

[29] X. T. He and Z. Z. Ren. Enhanced sensitivity to variation of fundamental constants in the transitions of th-229 and bk-249. *Journal of Physics G-Nuclear and Particle Physics*, 34(7):1611–1619, (2007).

[30] X. T. He and Z. Z. Ren. Enhanced sensitivity to variation of fundamental constants in the narrow nuclear transitions (ii). *Journal of Physics G-Nuclear and Particle Physics*, 35(3):–, (2008).

[31] B. R. Beck, J. A. Becker, P. Beiersdorfer, G. V. Brown, K. J. Moody, J. B. Wilhelmy, F. S. Porter, C. A. Kilbourne, and R. L. Kelley. Energy splitting of the ground-state doublet in the nucleus th-229. *Physical Review Letters*, 98(14):–, (2007).

[32] L. A. Kroger and C. W. Reich. Features of low-energy level scheme of th-229 as observed in alpha-decay of u-233. *Nuclear Physics A*, 259(1):29–60, (1976).

[33] C. W. Reich and R. G. Helmer. Energy separation of the doublet of intrinsic states at the ground-state of th-229. *Physical Review Letters*, 64(3):271–273, (1990).

[34] R. G. Helmer and C. W. Reich. An excited-state of th-229 at 3.5 ev. *Physical Review C*, 49(4):1845–1858, (1994).

[35] G. M. Irwin and K. H. Kim. Observation of electromagnetic radiation from de-excitation of the th-229 isomer. *Physical Review Letters*, 79(6):990–993, (1997).

[36] D. S. Richardson, D. M. Benton, D. E. Evans, J. A. R. Griffith, and G. Tungate. Ultraviolet photon emission observed in the search for the decay of the th-229 isomer. *Physical Review Letters*, 80(15):3206–3208, (1998).

[37] R. W. Shaw, J. P. Young, S. P. Cooper, and O. F. Webb. Spontaneous ultraviolet emission from (233)uranium/(229)thorium samples. *Physical Review Letters*, 82(6):1109–1111, (1999).

[38] S. B. Utter, P. Beiersdorfer, A. Barnes, R. W. Lougheed, J. R. C. Lopez-Urrutia, J. A. Becker, and M. S. Weiss. Reexamination of the optical gamma ray decay in th-229. *Physical Review Letters*, 82(3):505–508, (1999).

[39] Y. Kasamatsu, H. Kikunaga, K. Takamiya, T. Mitsugashira, T. Nakanishi, Y. Ohkubo, T. Ohtsuki, W. Sato, and A. Shinohara. Search for the decay of th-229m by photon detection. *Radiochimica Acta*, 93(9-10):511–514, (2005).

[40] I.D. Moore. Search for a low-lying 3.5 ev isomeric state in 229-th. *Argonne National Lab Physics Division Report*, (2004).

[41] P. Kalman and T. Bukki. Deexcitation of th-229(m): Direct gamma decay and electronic-bridge process. *Physical Review C*, 6302(2):–, (2001).

[42] E. V. Tkalya. Properties of the optical transition in the th-229 nucleus. *Physics-Uspekhi*, 46(3):315–320, (2003).

[43] F. F. Karpeshin and M. B. Trzhaskovskaya. Impact of the electron environment on the lifetime of the th-229(m) low-lying isomer. *Physical Review C*, 76(5):–, (2007).

[44] W. Kalber, G. Meisel, J. Rink, and R.C. Thompson. Two-step optical excitation for doppler linewidth reduction and motion study of ions stored in a paul trap. *Journal of Modern Optics*, 39(2):335–347, (1992).

[45] P. F. A. Klinkenberg. Spectral structure of trebly ionized thorium, th-iv. *Physica B and C*, 151(3):552–567, (1988).

[46] W. Kalber, J. Rink, K. Bekk, W. Faubel, S. Goring, G. Meisel, H. Rebel, and R. C. Thompson. Nuclear radii of thorium isotopes from laser spectroscopy of stored ions. *Zeitschrift Fur Physik a-Hadrons and Nuclei*, 334(1):103–108, (1989).

[47] N. Kurz, M. R. Dietrich, G. Shu, R. Bowler, J. Salacka, V. Mirgon, and B. B. Blinov. Measurement of the branching ratio in the 6p(3/2) decay of baii with a single trapped ion. *Physical Review A*, 77(6):–, (2008).

[48] F. F. Karpeshin, I. M. Band, M. B. Trzhaskowskaya, and B. A. Zon. Study of th-229 through laser-induced resonance internal-conversion. *Physics Letters B*, 282(3-4):267–270, (1992).

[49] F. F. Karpeshin and M. B. Trzhaskovskaya. Resonance conversion as a dominant decay mode for the 3.5-ev isomer in th-229m. *Physics of Atomic Nuclei*, 69(4):571–580, (2006).

[50] P. Kalman and T. Bukki. Deexcitation of th-229(m): Direct gamma decay and electronic-bridge process. *Physical Review C*, 6302(2):–, (2001).

[51] B. H. Bransden and C. J. Joachain. *Physics of atoms and molecules*. Prentice Hall, Harlow, England ; New York, 2nd edition, (2003).

[52] E. Browne, E. B. Norman, R. D. Canaan, D. C. Glasgow, J. M. Keller, and J. P. Young. Search for decay of the 3.5-ev level in th-229. *Physical Review C*, 6401(1):–, (2001).

[53] T. Mitsugashira, M. Hara, T. Ohtsuki, H. Yuki, K. Takamiya, Y. Kasamatsu, A. Shinohara, H. Kikunaga, and T. Nakanishi. Alpha-decay from the 3.5 ev isomer of th-229. *Journal of Radioanalytical and Nuclear Chemistry*, 255(1):63–66, (2003).

[54] R. J. Jones, K. D. Moll, M. J. Thorpe, and J. Ye. Phase-coherent frequency combs in the vacuum ultraviolet via high-harmonic generation inside a femtosecond enhancement cavity. *Physical Review Letters*, 94(19):–, (2005).

[55] C. E. M. Strauss and D. J. Funk. Broadly tunable difference-frequency-generation of vuv using 2-photon resonances in h2 and kr. *Optics Letters*, 16(15):1192–1194, (1991).

[56] David J. Griffiths. *Introduction to electrodynamics*. Prentice Hall, Upper Saddle River, N.J., 3rd edition, (1999).

[57] W. Paul. Electromagnetic traps for charged and neutral particles. *Reviews of Modern Physics*, 62(3):531–540, (1990).

[58] J. D. Prestage, G. J. Dick, and L. Maleki. New ion trap for frequency standard applications. *Journal of Applied Physics*, 66(3):1013–1017, (1989).

[59] D. J. Berkeland, J. D. Miller, J. C. Bergquist, W. M. Itano, and D. J. Wineland. Minimization of ion micromotion in a paul trap. *Journal of Applied Physics*, 83(10):5025–5033, (1998).

[60] J. M. Campbell, B. A. Collings, and D. J. Douglas. A new linear ion trap time-of-flight system with tandem mass spectrometry capabilities. *Rapid Communications in Mass Spectrometry*, 12(20):1463–1474, (1998).

[61] B. Landais, C. Beaugrand, L. Capron-Dukan, M. Sablier, G. Simonneau, and C. Rolando. Varying the radio frequency: a new scanning mode for quadrupole analyzers. *Rapid Communications in Mass Spectrometry*, 12(6):302–306, (1998).

[62] D. R. Denison. Operating parameters of a quadrupole in a grounded cylindrical housing. *Journal of Vacuum Science & Technology*, 8(1):266, (1971).

[63] N. Konenkov, F. Londry, C. F. Ding, and D. J. Douglas. Linear quadrupoles with added hexapole fields. *Journal of the American Society for Mass Spectrometry*, 17(8):1063–1073, (2006).

[64] M. Sudakov and D. J. Douglas. Linear quadrupoles with added octopole fields. *Rapid Communications in Mass Spectrometry*, 17(20):2290–2294, (2003).

[65] Y. Wang and J. Franzen. The nonlinear ion-trap .3. multipole components in 3 types of practical ion-trap. *International Journal of Mass Spectrometry and Ion Processes*, 132(3):155–172, (1994).

[66] J. E. Fulford, D. N. Hoa, R. J. Hughes, R. E. March, R. F. Bonner, and G. J. Wong. Radio-frequency mass selective excitation and resonant ejection of ions in a 3-dimensional quadrupole ion trap. *Journal of Vacuum Science & Technology*, 17(4):829–835, (1980).

[67] Pradip K. Ghosh. *Ion traps*. The International series of monographs on physics. Clarendon Press ; Oxford University Press, Oxford New York, (1995).

[68] N. Madsen, P. Bowe, M. Drewsen, L. H. Hornekaer, N. Kjaergaard, A. Labrador, J. S. Nielsen, J. P. Schiffer, P. Shi, and J. S. Hangst. Density limitations in a stored laser-cooled ion beam. *Physical Review Letters*, 83(21):4301–4304, (1999).

[69] Rodney Loudon. *The quantum theory of light*. Oxford science publications. Oxford University Press, Oxford ; New York, 3rd edition, (2000).

[70] F. G. Major and H. G. Dehmelt. Exchange-collision technique for rf spectroscopy of stored ions. *Physical Review*, 170(1):91, (1968).

[71] R. Blatt, P. Zoller, G. Holzmuller, and I. Siemers. Brownian-motion of a parametric oscillator - a model for ion confinement in radiofrequency traps. *Zeitschrift Fur Physik D-Atoms Molecules and Clusters*, 4(2):121–126, (1986).

[72] H. Schaaf, U. Schmeling, and G. Werth. Trapped ion density distribution in the presence of he-buffer gas. *Applied Physics*, 25(3):249–251, (1981).

[73] Y. Moriwaki and T. Shimizu. Effect of a heavy collision partner on ion loss from a radio frequency trap. *Japanese Journal of Applied Physics Part 1-Regular Papers Short Notes & Review Papers*, 37(1):344–348, (1998).

[74] Y. Moriwaki, M. Tachikawa, Y. Maeno, and T. Shimizu. Collision cooling of ions stored in quadrupole radiofrequency trap. *Japanese Journal of Applied Physics Part 2-Letters*, 31(11B):L1640–L1643, (1992).

[75] M. Green, J. Wodin, R. Devoe, P. Fierlinger, B. Flatt, G. Gratta, F. LePort, M. M. Diez, R. Neilson, K. O'Sullivan, A. Pocar, S. Waldman, D. S. Leonard, A. Piepke, C. Hargrove, D. Sinclair, V. Strickland, W. Fairbank, K. Hall, B. Mong, M. Moe, J. Farine, D. Hallman, C. Virtue, E. Baussan, Y. Martin, D. Schenker, J. L. Vuilleumier, J. M. Vuilleumier, P. Weber, M. Breidenbach, R. Conley, C. Hall, J. Hodgson, D. Mackay, A. Odian, C. Y. Prescott, P. C. Rowson, K. Skarpaas, and K. Wamba. Observation of single collisionally cooled trapped ions in a buffer gas. *Physical Review A*, 76(2):–, (2007).

[76] Harold J. Metcalf and Peter Van der Straten. *Laser cooling and trapping*. Graduate texts in contemporary physics. Springer, New York, (1999).

[77] D. Wineland and H. Dehmelt. Proposed 1014 delta upsilon less than upsilon laser fluorescence spectroscopy on t1+ mono-ion oscillator iii. *Bulletin of the American Physical Society*, 20(4):637–637, (1975).

[78] T. W. Hansch and A. L. Schawlow. Cooling of gases by laser radiation. *Optics Communications*, 13(1):68–69, (1975).

[79] D. J. Wineland and W. M. Itano. Laser cooling of atoms. *Physical Review A*, 20(4):1521–1540, (1979).

[80] R. Blatt, G. Lafyatis, W. D. Phillips, S. Stenholm, and D. J. Wineland. Cooling in traps. *Physica Scripta*, T22:216–223, (1988).

[81] S. Stenholm. The semiclassical theory of laser cooling. *Reviews of Modern Physics*, 58(3):699–739, (1986).

[82] R. E. Drullinger, D. J. Wineland, and J. C. Bergquist. High-resolution optical-spectra of laser cooled ions. *Applied Physics*, 22(4):365–368, (1980).

[83] T. Rosenband, D. B. Hume, P. O. Schmidt, C. W. Chou, A. Brusch, L. Lorini, W. H. Oskay, R. E. Drullinger, T. M. Fortier, J. E. Stalnaker, S. A. Diddams, W. C. Swann, N. R. Newbury, W. M. Itano, D. J. Wineland, and J. C. Bergquist. Frequency ratio of al+ and hg+ single-ion optical clocks; metrology at the 17th decimal place. *Science*, 319(5871):1808–1812, (2008).

[84] H. R. Gray, R. M. Whitley, and C. R. Stroud. Coherent trapping of atomic populations. *Optics Letters*, 3(6):218–220, (1978).

[85] C. Raab, J. Bolle, H. Oberst, J. Eschner, F. Schmidt-Kaler, and R. Blatt. Diode laser spectrometer at 493 nm for single trapped ba+ ions. *Applied Physics B-Lasers and Optics*, 67(6):683–688, (1998).

[86] D. J. Berkeland and M. G. Boshier. Destabilization of dark states and optical spectroscopy in zeeman-degenerate atomic systems. *Physical Review A*, 65(3):–, (2002).

[87] E. Wigner. Effects of the electron interaction on the energy levels of electrons in metals. *Transactions of the Faraday Society*, 34(1):0678–0685, (1938).

[88] W. L. Slattery, G. D. Doolen, and H. E. Dewitt. Improved equation of state for the classical one-component plasma. *Physical Review A*, 21(6):2087–2095, (1980).

[89] R. F. Wuerker, H. Shelton, and R. V. Langmuir. Electrodynamic containment of charged particles. *Journal of Applied Physics*, 30(3):342–349, (1959).

[90] F. Diedrich, E. Peik, J. M. Chen, W. Quint, and H. Walther. Observation of a phase-transition of stored laser-cooled ions. *Physical Review Letters*, 59(26):2931–2934, (1987).

[91] R. Blumel, J. M. Chen, E. Peik, W. Quint, W. Schleich, Y. R. Shen, and H. Walther. Phase-transitions of stored laser-cooled ions. *Nature*, 334(6180):309–313, (1988).

[92] J. Hoffnagle, R. G. Devoe, L. Reyna, and R. G. Brewer. Order-chaos transition of 2 trapped ions. *Physical Review Letters*, 61(3):255–258, (1988).

[93] R. G. Brewer, J. Hoffnagle, R. G. Devoe, L. Reyna, and W. Henshaw. Collision-induced 2-ion chaos. *Nature*, 344(6264):305–309, (1990).

[94] R. Blumel, C. Kappler, W. Quint, and H. Walther. Chaos and order of laser-cooled ions in a paul trap. *Physical Review A*, 40(2):808–823, (1989).

[95] P. M. Stier and C. F. Barnett. Charge exchange cross sections of hydrogen ions in gases. *Physical Review*, 103(4):896–907, (1956).

[96] D. A. Church. Charge-changing collisions of stored, multiply-charged ions. *Journal of Modern Optics*, 39(2):423–429, (1992).

[97] D. M. Lucas, A. Ramos, J. P. Home, M. J. McDonnell, S. Nakayama, J. P. Stacey, S. C. Webster, D. N. Stacey, and A. M. Steane. Isotope-selective photoionization for calcium ion trapping. *Physical Review A*, 69(1):–, (2004).

[98] S. Willitsch, M. T. Bell, A. D. Gingell, S. R. Procter, and T. P. Softley. Cold reactive collisions between laser-cooled ions and velocity-selected neutral molecules. *Physical Review Letters*, 1(4):–, (2008).

[99] A. E. Siegman. *Lasers*. University Science Books, Mill Valley, Calif., (1986).

[100] J. McKeever, J. R. Buck, A. D. Boozer, A. Kuzmich, H. C. Nagerl, D. M. Stamper-Kurn, and H. J. Kimble. State-insensitive cooling and trapping of single atoms in an optical cavity. *Physical Review Letters*, 90(13):–, (2003).

[101] W. von Klitzing, R. Long, V. S. Ilchenko, J. Hare, and V. Lefevre-Seguin. Tunable whispering gallery modes for spectroscopy and cqed experiments. *New Journal of Physics*, 3:141–1414, (2001).

[102] Paul R. Berman. *Cavity quantum electrodynamics*. Academic Press, Boston, (1994).

[103] D. J. Berkeland. Linear paul trap for strontium ions. *Review of Scientific Instruments*, 73(8):2856–2860, (2002).

[104] W. W. Macalpine and R. O. Schildknecht. Coaxial resonators with helical inner conductor. *Proceedings of the Institute of Radio Engineers*, 47(12):2099–2105, (1959).

[105] J. Gurell, E. Biemont, K. Blagoev, V. Fivet, P. Lundin, S. Mannervik, L. O. Norlin, P. Quinet, D. Rostohar, P. Royen, and P. Schef. Laser-probing measurements and calculations of lifetimes of the 5d d-2(3/2) and 5d d-2(5/2) metastable levels in baii. *Physical Review A*, 75(5):–, (2007).

[106] D. J. Armstrong and J. Cooper. Isotope-selective photoionization spectroscopy of barium. *Physical Review A*, 47(4):R2446–R2449, (1993).

[107] A. V. Steele, L. R. Churchill, P. F. Griffin, and M. S. Chapman. Photoionization and photoelectric loading of barium ion traps. *Physical Review A*, 75(5):–, (2007).

[108] P. Grundevik, M. Gustavsson, G. Olsson, and T. Olsson. Hyperfine-structure and isotope-shift measurements in the 6s5d[- -]6p5d transitions of ba-i in the far-red spectral region. *Zeitschrift Fur Physik a-Hadrons and Nuclei*, 312(1-2):1–9, (1983).

[109] N. D. Scielzo, J. R. Guest, E. C. Schulte, I. Ahmad, K. Bailey, D. L. Bowers, R. J. Holt, Z. T. Lu, T. P. O'Connor, and D. H. Potterveld. Measurement of the lifetimes of the lowest p-3(1) state of neutral ba and ra. *Physical Review A*, 73(1):–, (2006).

[110] C. J. Erickson, B. Neyenhuis, and D. S. Durfee. High-temperature calcium vapor cell for spectroscopy on the 4s(2) s-1(0)-4s4p p-3(1) intercombination line. *Review of Scientific Instruments*, 76(12):–, (2005).

[111] C. R. Vidal and J. Cooper. Heat-pipe oven - a new, well-defined metal vapor device for spectroscopic measurements. *Journal of Applied Physics*, 40(8):3370–3374, (1969).

[112] P. Bowe, L. Hornekaer, C. Brodersen, M. Drewsen, J. S. Hangst, and J. P. Schiffer. Sympathetic crystallization of trapped ions. *Physical Review Letters*, 82(10):2071–2074, (1999).

[113] Jacob Sauer. *Cold Atom Manipulation for Quantum Computing and Control*. PhD thesis, —2004—.

[114] Kevin Fortier. *Individual Trapped Atoms For Cavity QED Quantum Information Applications*. PhD thesis, —2007—.

[115] M. Drewsen, C. Brodersen, L. Hornekaer, J. S. Hangst, and J. P. Schiffer. Large ion crystals in a linear paul trap. *Physical Review Letters*, 81(14):2878–2881, (1998).

[116] R. F. Boivin and S. K. Srivastava. Electron-impact ionization of mg. *Journal of Physics B-Atomic Molecular and Optical Physics*, 31(10):2381–2394, (1998).

[117] C. Ronchi and J. P. Hiernaut. Experimental measurement of pre-melting and melting of thorium dioxide. *Journal of Alloys and Compounds*, 240(1-2):179–185, (1996).

[118] B. Thestrup, B. Toftmann, J. Schou, B. Doggett, and J. G. Lunney. Ion dynamics in laser ablation plumes from selected metals at 355 nm. *Applied Surface Science*, 197:175–180, (2002).

[119] U. I. Safronova, W. R. Johnson, and M. S. Safronova. Excitation energies, polarizabilities, multipole transition rates, and lifetimes in thiv. *Physical Review A*, 74(4):–, (2006).

[120] B. Roth, A. Ostendorf, H. Wenz, and S. Schiller. Production of large molecular ion crystals via sympathetic cooling by laser-cooled ba+. *Journal of Physics B-Atomic Molecular and Optical Physics*, 38(20):3673–3685, (2005).

[121] V. H. S. Kwong. Production and storage of low-energy highly charged ions by laser ablation and an ion trap. *Physical Review A*, 39(9):4451–4454, (1989).

[122] L. Deslauriers, S. Olmschenk, D. Stick, W. K. Hensinger, J. Sterk, and C. Monroe. Scaling and suppression of anomalous heating in ion traps. *Physical Review Letters*, 97(10):–, (2006).

[123] P. Bowe, L. Hornekaer, C. Brodersen, M. Drewsen, J. S. Hangst, and J. P. Schiffer. Sympathetic crystallization of trapped ions. *Physical Review Letters*, 82(10):2071–2074, (1999).

[124] K. M. Fortier, Y. Kim, M. J. Gibbons, P. Ahmadi, and M. S. Chapman. Deterministic loading of individual atoms to a high-finesse optical cavity. *Physical Review Letters*, 98(23):–, (2007).

[125] R Frisch. *Z. Phys*, 86(42), (1933).

[126] D. N. Matsukevich, P. Maunz, D. L. Moehring, S. Olmschenk, and C. Monroe. Bell inequality violation with two remote atomic qubits. *Physical Review Letters*, 100(15):–, (2008).

[127] J. McKeever, A. Boca, A. D. Boozer, J. R. Buck, and H. J. Kimble. Experimental realization of a one-atom laser in the regime of strong coupling. *Nature*, 425(6955):268–271, (2003).

[128] A. H. Myerson, D. J. Szwer, S. C. Webster, D. T. C. Allcock, M. J. Curtis, G. Imreh, J. A. Sherman, D. N. Stacey, A. M. Steane, and D. M. Lucas. High-fidelity readout of trapped-ion qubits. *Physical Review Letters*, 100(20):–, (2008).

[129] M. G. Raizen, J. M. Gilligan, J. C. Bergquist, W. M. Itano, and D. J. Wineland. Ionic-crystals in a linear paul trap. *Physical Review A*, 45(9):6493–6501, (1992).

[130] J. P. Reithmaier, G. Sek, A. Loffler, C. Hofmann, S. Kuhn, S. Reitzenstein, L. V. Keldysh, V. D. Kulakovskii, T. L. Reinecke, and A. Forchel. Strong coupling in a single quantum dot-semiconductor microcavity system. *Nature*, 432(7014):197–200, (2004).

[131] A. Wallraff, D. I. Schuster, A. Blais, L. Frunzio, R. S. Huang, J. Majer, S. Kumar, S. M. Girvin, and R. J. Schoelkopf. Strong coupling of a single photon to a superconducting qubit using circuit quantum electrodynamics. *Nature*, 431(7005):162–167, (2004).

INDEX

VITA

Adam V. Steele was born in Livingston New Jersey.